1 KOPIO - a search for $K^0 \to \pi^0 \nu \bar{\nu}$

I-H. Chiang, J.W. Glenn, V. Jain, D. Lazarus, K. Li,
L. Littenberg[1], G. Redlinger, R. Strand
Brookhaven National Laboratory

K. Kinoshita
University of Cinncinnati

G. Atoyan, M. Grigoriev, V. Issakov, A. Ivashkin, M. Khabibullin,
A. Khotjanzev, Y. Kudenko, O. Mineev, A. Poblaguev
INR, Moscow

T. Nomura, N. Sasao
Kyoto University

M. Blecher, M. Pitt, B. Vogelaar
Virginia Polytechnic Institute & State University

B. Bassalleck, N. Bruner, D.E. Fields, J. Lowe, T.L. Thomas
University of New Mexico

M. Ito
Thomas Jefferson National Accelerator Facility

E. Blackmore, D. Bryman[1], P. Gumplinger, M. Hasinoff, A. Konaka,
J. Macdonald, T. Numao, R. Poutissou, G. Smith
TRIUMF/UBC

S.K. Dhawan, H. Kaspar, S. Pislak, M.E. Zeller[1]
Yale University

P. Truöl
University of Zurich

[1]co-spokesperson

Contents

1.1 Introduction

At the present time CP violation is recognized to be one of the most important outstanding issues in the study of elementary particle physics. It is being vigorously attacked in the B sector by existing experiments such as CDF at the Fermilab Tevatron Collider and new ones constructed specifically for this purpose, including BaBar at SLAC's PEP-II, BELLE at KEKB, and HERA-B at DESY. The KOPIO component of the RSVP project proposes to add a new dimension to this world wide effort: a measurement of direct CP violation in the K sector via the decay $K_L^0 \to \pi^0 \nu\bar{\nu}$.

The single most incisive measurement in the study of CP violation is that of the branching ratio for $K_L^0 \to \pi^0 \nu\bar{\nu}$ ($\mathrm{B}(K_L^0 \to \pi\nu\bar{\nu})$). Using current estimates for Standard Model (SM) parameters, it is expected to lie in the range $(3.1 \pm 1.3) \times 10^{-11}$ [1]. In the SM this branching ratio is unique in that it directly measures the area of the CKM unitarity triangle, i.e. the physical parameter that characterizes CP violation.

The $\pi^0\nu\bar{\nu}$ decay mode is also unique in that it is completely dominated by direct CP violation [2] and is entirely governed by short-distance physics involving the top quark. Theoretical uncertainties are extremely small because hadronic effects can be extracted from the well measured decay $K^+ \to \pi^0 e^+ \nu$. Thus its measurement will provide the standard against which all other measurements of CP violation will be compared, and even small deviations from the expectation derived from other SM measurements will unambiguously signal the presence of new physics.

The experimental aspects of measuring $\mathrm{B}(K_L^0 \to \pi^0 \nu\bar{\nu})$ are quite challenging. The mode is a three body decay where only a π^0 is observed. There are competing decay modes which also yield π^0s, but whose branching ratios are millions of times larger. And observing a decay mode with a branching ratio on the order of 3×10^{-11} requires a prodigious number of kaons in order to achieve the desired sensitivity. Because the measurement is so challenging a detection technique must be developed that provides maximum possible redundancy for this kinematically unconstrained decay, that has an optimum system for insuring that the observed π^0 is the only observable particle emanating from the K_L^0 decay, and that has multiple handles for identifying possible small backgrounds that might simulate the desired decay mode. It is with these issues in mind that the KOPIO experiment has been designed.

The KOPIO technique employs a low energy, time structured K_L^0 beam to allow determination of the incident kaon momentum. This intense beam, with its special characteristics, can be provided by the BNL AGS. Utilizing low momentum also permits a detection system for the π^0 decay photons that yields a fully constrained reconstruction of the π^0's mass, energy, and, momentum. As is shown in this proposal, these features provide the necessary redundancy and checks mentioned above. The system for vetoing extra particles is also well understood since it is based on experience with a previous experiment, BNL E787, which successfully contended with particles in the same energy domain.

The goal of KOPIO is to obtain about 60 events with a signal to background ratio of 2:1. This will yield a statistical uncertainty in the measurement of the area of the CKM unitarity triangle of less than 10%.

In what follows, the theoretical motivation (Section 1.2), experimental overview (Section 1.3), accelerator and beam (Sections 1.4 and 1.5), detector (Sections 1.6 to 1.11), and background and sensitivity (Sections 1.12 to 1.14) are presented.

1.2 $K_L^0 \to \pi^0 \nu\bar{\nu}$ – Theoretical Motivation

1.2.1 Standard Model

Understanding the phenomenology of quark mixing and CP violation is currently one of the central goals of particle physics. Examining the CKM ansatz of the Standard Model (SM) through precise determination of its basic parameters, several of which are poorly known at present, is crucial. To assure a clear interpretation of experimental results, the ideal observable must not only be sensitive to fundamental parameters, but must also be calculable with little theoretical ambiguity.

The rare decay $K_L^0 \to \pi^0 \nu\bar{\nu}$ is unique among potential SM observables; it is dominated by direct CP violation [2] and is entirely governed by short-distance physics involving the top quark (for general reviews see [3, 4]). Long distance effects have been shown to be negligible [5]. Theoretical uncertainties are extremely small because the hadronic matrix element can be extracted from the well measured decay $K^+ \to \pi^0 e^+ \nu$, where small isospin breaking effects have been calculated. Since the dominant uncertainty due to renormalization scale dependence has been practically eliminated by including next-to-leading QCD corrections, the remaining theoretical uncertainty for $B(K_L^0 \to \pi^0 \nu\bar{\nu})$ is reduced to O(1%).

$K_L^0 \to \pi^0 \nu\bar{\nu}$ is a flavor-changing neutral current (FCNC) process that is induced through loop effects in the Standard Model. The leading electroweak diagrams are shown in fig. 1. The expression for the $K_L^0 \to \pi^0 \nu\bar{\nu}$ branching ratio can be written as

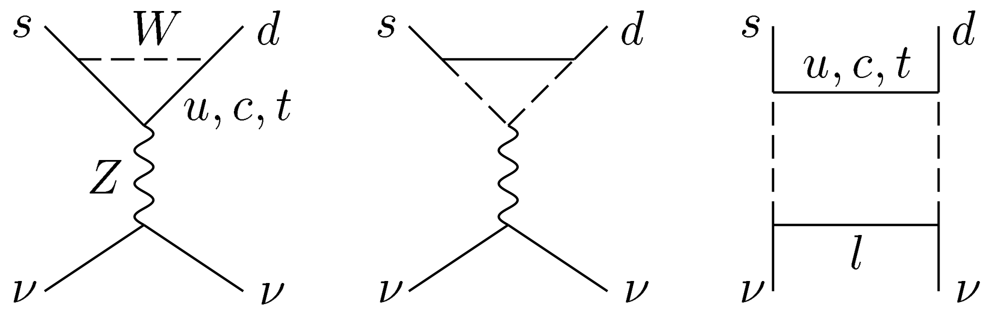

Figure 1: The leading electroweak diagrams inducing $K_L^0 \to \pi^0 \nu\bar{\nu}$.

$$B(K_L^0 \to \pi^0 \nu\bar{\nu}) = r_{IB} \frac{B(K^+ \to \pi^0 e^+ \nu)}{|V_{us}|^2} \frac{\tau(K_L^0)}{\tau(K^+)} \frac{3\alpha^2}{2\pi^2 \sin^4 \Theta_W} [Im(V_{ts}^* V_{td}) X(x_t)]^2 \tag{1}$$

where

$$X(x) \equiv \eta_X \cdot \frac{x}{8} \left[\frac{x+2}{x-1} + \frac{3x-6}{(x-1)^2} \ln x \right] \qquad \eta_X = 0.985 \tag{2}$$

and $x_t = m_t^2/M_W^2$. Here the appropriate top quark mass to be used is the running $\overline{MS}$ mass, $m_t \equiv \bar{m}_t(m_t)$, which is related by $\bar{m}_t(m_t) = m_t^*(1 - 4/3 \cdot \alpha_s(m_t)/\pi)$ to the pole mass m_t^* measured in collider experiments. With this choice of mass definition the QCD correction factor is given by $\eta_X = 0.985$ and is essentially independent of m_t [6]. The coefficient

$r_{IB} = 0.944$ summarizes the leading isospin breaking corrections in relating $K_L^0 \to \pi^0\nu\bar{\nu}$ to $K^+ \to \pi^0 e^+\nu$ [7].

$K_L^0 \to \pi^0\nu\bar{\nu}$ is driven by direct CP violation due to the CP properties of K_L, π^0 and the relevant short-distance hadronic transition current. Since K_L^0 is predominantly a coherent, CP odd superposition of K^0 and $\bar{K}^0$, only the imaginary part of $V_{ts}^* V_{td}$ survives in the amplitude. Since the value of the sine of the Cabibbo angle is well known ($|V_{us}| = \lambda = 0.2205$), this quantity is equivalent to the Jarlskog invariant, $\mathcal{J} \equiv -Im(V_{ts}^* V_{td} V_{us}^* V_{ud}) = -\lambda(1 - \frac{\lambda^2}{2}) Im(V_{ts}^* V_{td})$. $\mathcal{J}$, in turn, is equal to twice the area of any of the six possible unitarity triangles[8]. A comparison of the area of any unitarity triangle obtained indirectly through studies of the B system or otherwise with the same quantity obtained directly from $K_L^0 \to \pi^0\nu\bar{\nu}$ is then a critical test of the SM explanation of CP violation.

To facilitate the SM prediction of $B(K_L^0 \to \pi^0\nu\bar{\nu})$ and exhibit its relation to other measurements, we employ the Wolfenstein parametrization (λ, A, ϱ, η) of the CKM matrix, which allows a display of unitarity in a transparent way. In this representation, Eqn. 1 can be recast as

$$B(K_L^0 \to \pi^0\nu\bar{\nu}) = 1.8 \cdot 10^{-10} \eta^2 A^4 X^2(x_t) \tag{3}$$

Inserting the current estimates for SM parameters into Eqn. 3, the branching ratio for $K_L^0 \to \pi^0\nu\bar{\nu}$ is expected to lie in the range $(3.1 \pm 1.3) \cdot 10^{-11}$[1]. The unitarity relation

$$1 + \frac{V_{td} V_{tb}^*}{V_{cd} V_{cb}^*} = -\frac{V_{ud} V_{ub}^*}{V_{cd} V_{cb}^*} \equiv \bar{\varrho} + i\bar{\eta} \tag{4}$$

determines the most commonly discussed triangle in the $(\bar{\varrho}, \bar{\eta})$ plane. Here $\bar{\varrho} = \varrho(1 - \lambda^2/2)$ and $\bar{\eta} = \eta(1 - \lambda^2/2)$. This unitarity triangle is illustrated in fig. 2. A clean measure of its height is provided by the $K_L^0 \to \pi^0\nu\bar{\nu}$ branching ratio. We note that, all other parameters being known, Eqn. 3 implies that the relative error on η is half that on $B(K_L^0 \to \pi^0\nu\bar{\nu})$. Thus, for example, a 15% measurement of $B(K_L^0 \to \pi^0\nu\bar{\nu})$ can in principle determine η to 7.5%.

To construct the complete unitarity triangle in the K system, the charged mode $K^+ \to \pi^+\nu\bar{\nu}$ which is closely related to $K_L^0 \to \pi^0\nu\bar{\nu}$ is also needed. However, $K^+ \to \pi^+\nu\bar{\nu}$ is not CP violating and receives a non-negligible charm contribution leading to a slightly higher theoretical uncertainty (about 5%) [9]. Measurement of $B(K^+ \to \pi^+\nu\bar{\nu})$ allows the extraction of $|V_{td}|$ with the least theoretical uncertainty. The first evidence for $K^+ \to \pi^+\nu\bar{\nu}$ was recently reported by E787 [10], at a branching ratio, B($K^+ \to \pi^+\nu\bar{\nu}$)= $4.2^{+9.7}_{-3.5} \times 10^{-10}$, that is several times higher than the central SM prediction (although statistically consistent with it). Analysis of substantial additional data is ongoing [11] and will indicate whether there is consistency with the SM prediction. Together with $B(K_L^0 \to \pi^0\nu\bar{\nu})$ the unitarity triangle is completely determined as shown in fig. 2. Only a few other possible SM observables (*e.g.* x_s/x_d, $B \to l^+l^-$ or certain CP asymmetries in B decays) provide similar opportunities for unambiguously revealing SM effects.

The pure B-system alternative to obtaining $\bar{\varrho}$ and $\bar{\eta}$ from $K \to \pi\nu\bar{\nu}$ discussed most frequently requires measuring B^0 or $\bar{B}^0 \to \pi\pi$ and B^0 or $\bar{B}^0 \to J/\psi K_S^0$. At B factories or hadronic colliders, the time-dependent asymmetry in the rate between B^0 and $\bar{B}^0$ must be measured in both cases. These CP violating asymmetries measure $\sin 2\alpha$ and $\sin 2\beta$, respectively, and could in principle be used to infer $\bar{\varrho}$ and $\bar{\eta}$ (fig. 2), completing the CKM

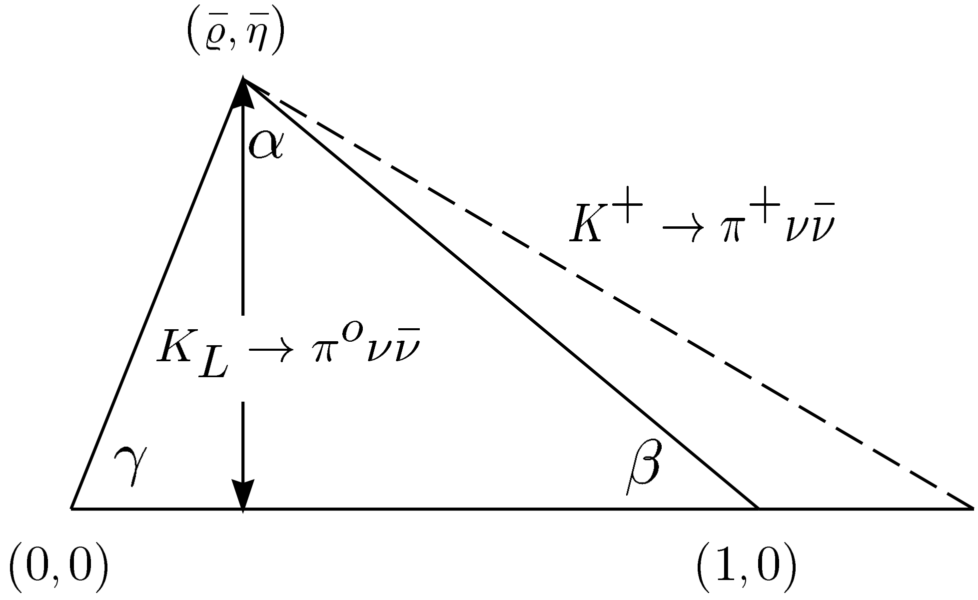

Figure 2: The unitarity triangle.

determination. However, the extraction of $\sin 2\alpha$ from $B \to \pi\pi$ is complicated by the presence of penguin contributions. If only the channel $B_d \to \pi^+\pi^-$ is used, these contributions introduce potentially sizable theoretical uncertainties [12]. On the other hand, avoiding penguin effects requires a careful isospin analysis and a combination of several modes, including the challenging decay $B_d \to \pi^0\pi^0$. Also, inferring $\bar{\varrho}$ and $\bar{\eta}$ from $\sin 2\alpha$ and $\sin 2\beta$ involves discrete ambiguities, so that some additional information (*e.g.* on the size of V_{ub}) is necessary to single out a unique solution. The CKM analysis for $K \to \pi\nu\bar{\nu}$ is less complicated, which could turn out to be of advantage in the unitarity triangle determination.

Alternatively, results from the CP violation experiments in B physics and a $K_L^0 \to \pi^0\nu\bar{\nu}$ measurement could also be combined for high precision determinations of the CKM matrix. One could complete a CKM matrix determination that is essentially free of hadronic uncertainties[13]. The method could become particularly interesting when CP asymmetries in B decays are measured with improved precision at the LHC. Such a precise determination of the independent CKM parameters, in which $K_L^0 \to \pi^0\nu\bar{\nu}$ plays a crucial role, would provide an ideal basis for comparison with other observables sensitive to mixing angles, like $K^+ \to \pi^+\nu\bar{\nu}$, $B \to \pi l\nu$, x_s/x_d or V_{cb} from $b \to c$ transitions. Any additional, independent determination of CKM parameters would then constitute a test of the Standard Model. Any significant deviation would point to new physics.

Additional strategies for combining and comparing information from the rare K and the B sector are described in Ref. [4]. Finally, it should be emphasized that it is very desirable that such fundamental quantities as ϱ and η be measured redundantly via methods that do not share the same systematic errors.

1.2.2 Non-standard Models

Extensions of the Standard Model can in principle modify the physics discussed above in many ways. Usually extended models introduce a variety of new degrees of freedom and *a priori* unknown parameters, and it is therefore difficult to obtain definite predictions. However one can make a few general remarks relevant for $K_L^0 \to \pi^0 \nu\bar{\nu}$ and the comparison with information from the B system. For a review of CP violation in B physics beyond the SM see [14, 15].

A clean SM test is provided by comparing η from $K_L^0 \to \pi^0 \nu\bar{\nu}$ with that triangulated from measurements of $|V_{ub}/V_{cb}|$ and x_d/x_s. Similarly, if B$(K^+ \to \pi^+\nu\bar{\nu})$ is measured, a very clean test is to compare the value of $\sin 2\beta$ obtained from the two kaon decays with that determined from the CP-asymmetry in $B \to J/\psi K_S^0$. Other incisive tests involve comparisons of the of the Jarlskog invariant obtained from $B(K_L^0 \to \pi^0\nu\bar{\nu})$ with indirect determinations of the same quantity from the B system. Any discrepancy would clearly indicate new physics. The more theoretically precise the observables under discussion, the smaller the deviation that could be detected.

In some new physics scenarios, such as multi-Higgs doublet models[16, 17] or minimal SUSY in which the CKM matrix remains the sole source of CP violation, the extraction of $\sin 2\alpha$ and $\sin 2\beta$ from CP asymmetries in B decays would be unaffected. Such effects might then show up in a comparison with $K_L^0 \to \pi^0\nu\bar{\nu}$, where e.g. charged Higgs contributions modify the top quark dependent function $X(x_t)$ in (1).

In other new physics scenarios, such as supersymmetric flavor models[18], the effects in $K \to \pi\nu\bar{\nu}$ tend to be small, while there can be large effects in the B (and also the D) system. In these models the rare K decays are the only clean way to measure the true CKM parameters.

Examples for new physics scenarios that show drastic deviations from the Standard Model are provided by some of the extended Higgs models discussed in [17], in topcolor-assisted technicolor models [19], in left-right symmetric models [20], in models with extra quarks in vector-like representations[21], lepto-quark exchange [21], and in 4-generation models [22].

In the past year, attention has been focussed on the contributions of flavor-changing Z-penguin diagrams in generic low-energy supersymmetric extensions of the Standard Model [18, 23, 24, 25, 26]. Such diagrams can interfere with the weak penguins of the Standard Model, and either raise or reduce the predicted $B(K_L^0 \to \pi^0\nu\bar{\nu})$ by considerable factors. Although there is still some controversy about this mechanism, it appears that very large effects are possible, possibly even more than an order of magnitude.

The E787 result on $K^+ \to \pi^+\nu\bar{\nu}$ and recent confirmation of a large value for ϵ'/ϵ[27, 28] have focussed much attention on rare K decays. Many of the BSM effects mentioned above could lead to a considerable enhancement of $B(K^+ \to \pi^+\nu\bar{\nu})$ over the SM prediction. The same type of flavor-changing Z-penguin diagrams that can contribute to rare K decays can affect ϵ'/ϵ [25]. If ϵ'/ϵ is dominated by such new physics, $B(K_L^0 \to \pi^0\nu\bar{\nu})$ can be more than 20 times higher than the central Standard Model prediction[25, 29]. It is also possible for such effects to suppress $B(K_L^0 \to \pi^0\nu\bar{\nu})$significantly. We stress, however, that as opposed to the case of ϵ'/ϵ, deviations from the predicted value of $B(K_L^0 \to \pi^0\nu\bar{\nu})$ unambiguously indicate the presence of new physics.

1.2.3 Theoretical summary

As a consequence of unprecedented theoretical precision and anticipated experimental accessibility, a measurement of $K_L^0 \to \pi^0 \nu\bar{\nu}$ can unambiguously test the SM origin of CP violation, directly measure the area of the unitarity triangle, and ultimately yield the most accurate determination of the CKM CP violating phase η. This rare decay mode therefore provides a unique opportunity for making significant progress in our understanding of flavor-dynamics and CP violation. It is competitive with and complementary to future measurements in the B meson system. If new physics is manifesting itself in $K^+ \to \pi^+ \nu\bar{\nu}$ and ϵ'/ϵ, it is virtually certain to show up in an unambiguous way in a measurement of $K_L^0 \to \pi^0 \nu\bar{\nu}$ at the SM-predicted level. Absence of $K_L^0 \to \pi^0 \nu\bar{\nu}$ within the range of about $(3 \pm 2) \times 10^{-11}$ or a conflict with other CKM determinations would certainly indicate new physics.

1.3 Overview of the $K_L^0 \to \pi^0 \nu\bar{\nu}$ measurement technique

Along with the challenge of obtaining sufficient detection sensitivity, one of the main issues in measuring an ultra-rare process is the control of systematic uncertainties in estimating tiny levels of backgrounds. In general Monte Carlo calculations are of limited value in assessing minute problems or low level physics processes which can simulate the signal. The only reliable recourse is to use data to systematically study the backgrounds. This is feasible when there is enough experimental information for each event so that the signal can be securely grasped, the backgrounds confidently rejected, and the background levels independently measured in spite of limited statistics. Only with reliable background determinations at a level well below the experiment's sensitivity can observation of an extremely small signal be firmly established. The KOPIO experiment has been designed with this approach in mind.

The complete experimental signature for the $K_L^0 \to \pi^0 \nu\bar{\nu}$ decay mode consists of exactly two photons with the invariant mass of a π^0, and nothing else. The experimental challenge arises from the 34% probability that a K_L^0 will emit at least one π^0 in comparison with the expected decay probability for $K_L^0 \to \pi^0 \nu\bar{\nu}$ which is ten orders of magnitude smaller. Compounding the difficulty, interactions between neutrons and kaons in the neutral beam with residual gas in the decay volume can also result in emission of single π^0s, as can the decays of hyperons which might occur in the decay region, *e.g.* $\Lambda \to \pi^0 n$. The current experimental limit $B(K_L^0 \to \pi^0 \nu\bar{\nu}) < 5.9 \times 10^{-7}$[30] comes from an auxiliary Fermilab experiment which employed the Dalitz decay $\pi^0 \to \gamma e^+ e^-$. Further improvement in sensitivity by perhaps an order of magnitude may be expected during the next few years. Thus, an experimental improvement in sensitivity of more than four orders of magnitude is required to obtain the signal for $K_L^0 \to \pi^0 \nu\bar{\nu}$ at the SM level of $B(K_L^0 \to \pi^0 \nu\bar{\nu}) = 3 \times 10^{-11}$.

For any experiment seeking to measure $K_L^0 \to \pi^0 \nu\bar{\nu}$ the most important means of eliminating unwanted events is to determine that nothing other than one π^0 was emitted in the decay, *i.e.* to veto any extra particles. The most difficult mode to suppress in this manner is $K_L^0 \to \pi^0 \pi^0$ ($K_{\pi 2}^0$). If this were the only defense against unwanted events, however, an extremely high (perhaps unachievable) photon veto detection efficiency would be required. Thus, to increase the probability that the source of an observed signal is truly $K_L^0 \to \pi^0 \nu\bar{\nu}$, another handle is needed.

That handle is provided by measurement of the K_L^0 momentum via time-of-flight (TOF). Copious low energy kaons can be produced at the AGS in an appropriately time structured beam. From knowledge of the decaying K_L^0 momentum the π^0 can be transformed to the K_L^0 center-of-mass frame and kinematic constraints can be imposed on an event-by-event basis. This technique facilitates rejection of bogus kaon decays and suppression of all other potential backgrounds, including otherwise extremely problematic ones such as hyperon decays and beam neutron and photon interactions.

The background suppression is achieved using a combination of hermetic high sensitivity photon vetoing and full reconstruction of each observed photon through measurements of position, angle and energy. Events originating in the two-body decay $K_L^0 \to \pi^0 \pi^0$ identify themselves when reconstructed in the K_L^0 center-of-mass system. Furthermore, those events with missing low energy photons, the most difficult to detect, can be identified and eliminated. With the two independent criteria based on precise kinematic measurements and demonstrated photon veto levels, not only is there enough experimental information so that

$K_L^0 \rightarrow \pi^0\pi^0$ can be suppressed to the level of an order of magnitude below the expected signal, but the background level can also be measured directly from data.

The beam and detectors for KOPIO employ well known technologies. Important aspects of the system are based on previously established measurement techniques and new aspects have been studied in beam measurements and with prototypes and simulations. Figure 3 shows a simplified representation of the beam and detector concept and fig. 4 gives a schematic layout of the entire apparatus. The 24 GeV primary proton beam is presented to the kaon production target in 200 ps wide pulses at a rate of 25 MHz giving a microbunch separation of 40 ns. A 500 μsr solid angle neutral beam is extracted at $\sim 40^o$ to produce a "soft" K_L spectrum peaked at 0.65 GeV/c; kaons in the range from about 0.4 GeV/c to 1.3 GeV/c are used. The vertical acceptance of the beam (0.005 r) is kept much smaller than the horizontal acceptance (0.1 r) so that effective collimation can be obtained to severely limit beam halos and to obtain another constraint on the decay vertex position. Downstream of the final beam collimator is a 4 m long decay region which is surrounded by the main detector. Approximately 16% of the kaons decay yielding a decay rate of about 14 MHz. The beam region is evacuated to a level of 10^{-7} Torr to suppress neutron-induced π^0 production. The decay region is surrounded by an efficient Pb/scintillator photon veto detector ("barrel veto"). In order to simplify triggering and offline analysis, only events with the signature of a single kaon decay producing two photons occurring within the period between microbunches are accepted.

Photons from $K_L^0 \rightarrow \pi^0\nu\bar{\nu}$ decay are observed in a two-stage endcap detector comprised of a fine-grained preradiator followed by an 18 radiation length (X_0) electromagnetic calorimeter. The preradiator obtains the times, positions and angles of the interacting photons from π^0 decay by determining the initial trajectories of the first e^+e^- pairs. The preradiator consists of 60 0.034 X_0-thick layers, each with plastic scintillator, converter and dual coordinate drift chamber. The preradiator has a total effective thickness of 2 X_0 and functions to measure the photon positions and directions accurately in order to allow reconstruction of the K_L decay vertex while also contributing to the achievement of sufficient energy resolution.

The calorimeter located behind the preradiator consists of "Shashlyk" tower modules, roughly 10 cm by 10 cm in cross section and 18 X_0 in depth. A Shashlyk calorimeter module consists of a stack of square tiles with alternating layers of Pb and plastic scintillator read out by penetrating WLS fibers. The preradiator-calorimeter combination is expected to have an energy resolution of $\sigma_\mathrm{E}/\mathrm{E} \simeq 0.033/\sqrt{\mathrm{E}}$. Shashlyk is a proven technique which has been used effectively in BNL experiment E865 and is presently the main element in the PHENIX calorimeter at RHIC.

Suppression of most backgrounds is provided by a hermetic high efficiency charged particle and photon detector system surrounding the decay volume. The system includes scintillators inside the vacuum chamber, decay volume photon veto detectors and detectors downstream of the main decay volume. The barrel veto detectors are constructed as Pb/scintillator sandwiches providing about 18 X_0 for photon conversion and detection. The detection efficiency for photons has been extensively studied with a similar system in BNL experiment E787. The downstream section of the veto system is needed to reject events where photons or charged particles leave the decay volume through the beam hole. It consists of a sweeping magnet with a horizontal field, scintillators to detect charged particles deflected out of the beam, and photon veto modules. A special group of counters - collectively, the "catcher"

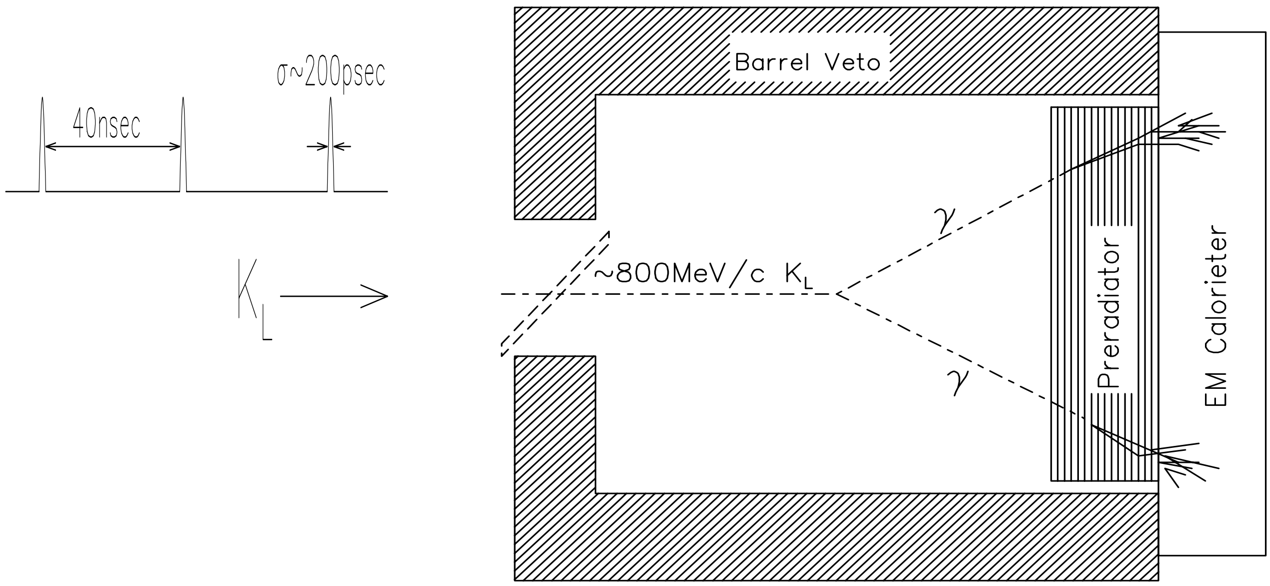

Figure 3: Elements of the KOPIO concept : a pulsed primary beam produces low energy kaons whose time-of-flight reveals their momentum when the π^0 from $K_L^0 \to \pi^0 \nu \bar{\nu}$ decay is reconstructed.

- vetoes particles that leave the decay volume but remain in the beam phase space. This system takes advantage of the low energy nature of our environment to provide the requisite veto efficiency while being blind to the vast majority of neutrons and K^0s in the beam. The catcher uses Cerenkov radiators read out with phototubes.

The KOPIO system described above will clearly identify the $K_L^0 \to \pi^0 \nu \bar{\nu}$ decay signal and effectively reject all backgrounds using a combination of kinematic measurements and photon vetos. Fig. 5 illustrates KOPIO's extensive arsenal of weapons including the measured quantities and constraints available. Reference values for the resolutions in the measured quantities are given in Table 1.

To illustrate how KOPIO will function to reject backgrounds, we consider bogus events originating with $K_{\pi 2}^0$ decays. The two types of $K_{\pi 2}^0$ background are the "even pairing" cases when the two observed photons come from one π^0 and the odd pairing cases when each photon originates from a different π^0. The odd pairing events will generally not reconstruct to the π^0 mass and are also suppressed by kinematic constraints as will be discussed below. Fig. 6 shows the π^0 energy distribution to be detected in the K_L center of mass frame ($E_{\pi^0}^*$) for the $K_L \to \pi^0 \nu \bar{\nu}$ and $K_L \to \pi^0 \pi^0$ ($K_{\pi 2}^0$) decays and fig. 7 gives the 2-gamma mass spectrum $M_{\gamma\gamma}$ for the signal ($M_{\gamma\gamma} = M_\pi$) and for the odd-pairing gammas.

By tagging the K_L momentum as well as determining the energy and direction of γs, one can fully reconstruct the kinematics in 2-body decays. In the case where one π^0 is missing from a $K_{\pi 2}^0$ decay ("even pairing"), a kinematic cut on the monochromatic center of mass energy $E_{\pi^0}^*$ is effective, as shown in fig. 6. In the case where one photon from each π^0 is missed ("odd pairing"), a π^0 mass requirement ($m_{\gamma\gamma}$) is effective as shown in fig. 7. Additional photon energy cuts on $E_{\pi^0}^*$ vs. $|E_{\gamma 1}^* - E_{\gamma 2}^*|$, where $E_{\gamma 1}^*$ and $E_{\gamma 2}^*$ are the energies of γs in the K_L center of mass system, are especially effective in further suppressing the $K_{\pi 2}^0$ background. This is illustrated in fig. 8 which shows distributions of $E_{\pi^0}^*$ vs. $|E_{\gamma 1}^* - E_{\gamma 2}^*|$ (using the

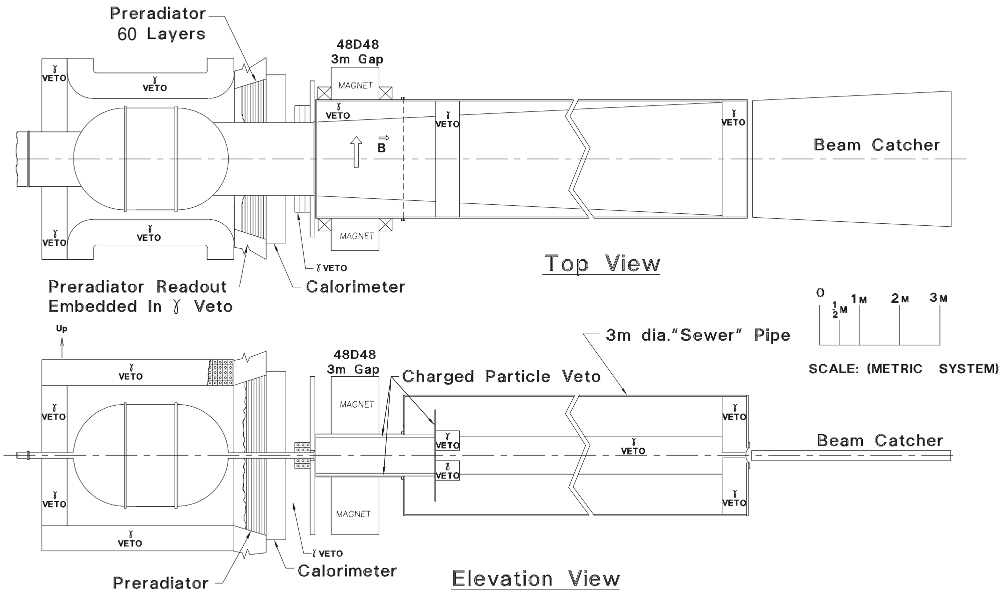

Figure 4: Plan and elevation views of KOPIO detector.

energy resolution indicated in Table 1 and after the π^0 mass requirement was imposed) for the $K_L \to \pi^0\pi^0$ (left plot) and for the $K_L^0 \to \pi^0\nu\bar{\nu}$ signal (right plot). The band in the left hand figure at $E^*_{\pi^0}$ =249MeV corresponds to the even pairing background, which is suppressed by a $E^*_{\pi^0}$ cut at 225MeV/c as discussed above. The remaining band corresponds to the odd pairing background, which is confined to a region constrained by the π^0 mass. The solid lines show the signal regions in both plots for nominal cuts[2]. Further background suppression can be had at the cost of modest acceptance loss providing a certain margin of safety. When reasonable photon veto efficiency values based on E787 measurements are also assumed, the added capability of full kinematic reconstruction leads to the $K^0_{\pi 2}$ background being suppressed to a level well below the anticipated signal. A more complete discussion of the potential backgrounds is given below.

Evaluation of the KOPIO system leads to the expectation that a signal of about 60 $K_L^0 \to \pi^0\nu\bar{\nu}$ events will be collected if the SM prediction holds. In the following sections, we provide details on the KOPIO beam, detection apparatus, sensitivity and backgrounds along with cost and schedule estimates.

[2]The signal region in Fig. 8 appears low in $E^*_{\pi^0}$. This is because the photon veto, which is not applied to the events shown in this figure, is especially effective at eliminating those odd-pairing events which appear in the signal box.

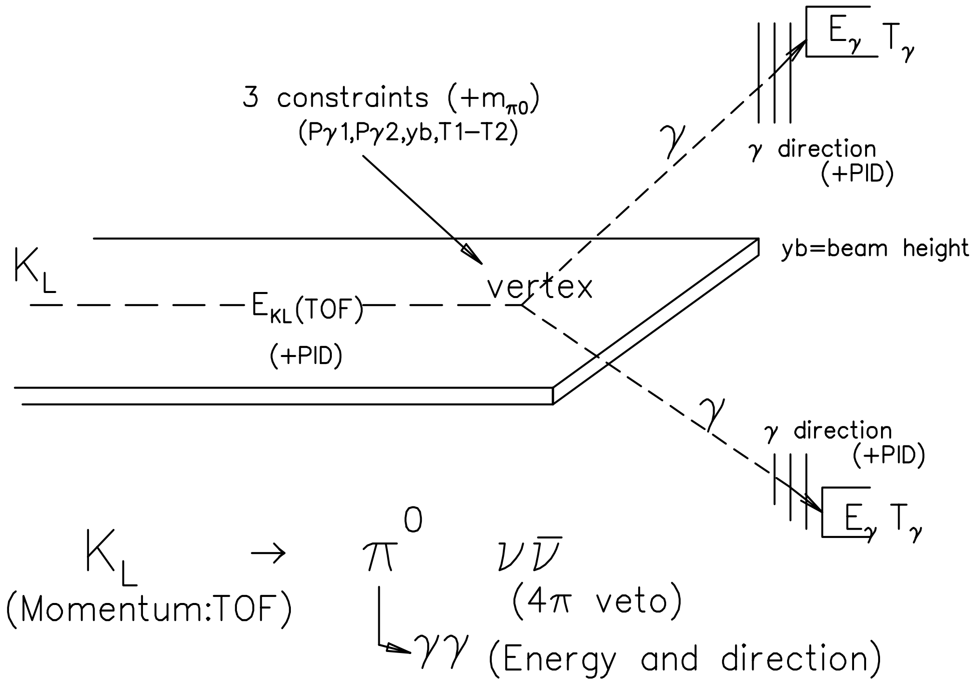

Figure 5: An illustration of quantities measured and constraints available in the KOPIO experiment. Measurements include the K_L energy, and the gamma energies, directions and times. Particle identification (PID) is also available. Constraints include the π^0 mass (M_π^0), the beam vertical extent (y_b) and relative timing of the photons.

Table 1: Parameters and nominal resolutions (σ's) for photon energy (E), angles (θ_{xz},θ_{yz}), conversion positions (x, y), and timing (t) anticipated for KOPIO. In simulations, each measured quantity is smeared by adding a quantity $G\sigma$ where G is a random value chosen from a normal distribution with zero mean and unit variance, and σ is given in the table.

Quantity	Nominal value	σ used in smearing
E	C_E (0.033 GeV$^{1/2}$)	$C_E/\sqrt{E}$
θ_{xz}	$\sigma_{\theta xz}$ (8.2mrad$\cdot$GeV$^{0.7}$)	$\sigma_{\theta xz} \cdot E^{-0.7}$(96%)
		$3.6 \cdot \sigma_{\theta xz} \cdot E^{-0.7}$(4%)
θ_{yz}	$\sigma_{\theta yz}$ (8.2mrad$\cdot$GeV$^{0.7}$)	$\sigma_{\theta yz} \cdot E^{-0.7}$(96%)
		$3.6 \cdot \sigma_{\theta yz} \cdot E^{-0.7}$(4%)
x	C_x (0.45 cm-GeV$^{1/2}$)	$C_x/\sqrt{E}$
y	C_y (0.45 cm-GeV$^{1/2}$)	$C_y/\sqrt{E}$
t	σ_t (0.2 ns)	σ_t

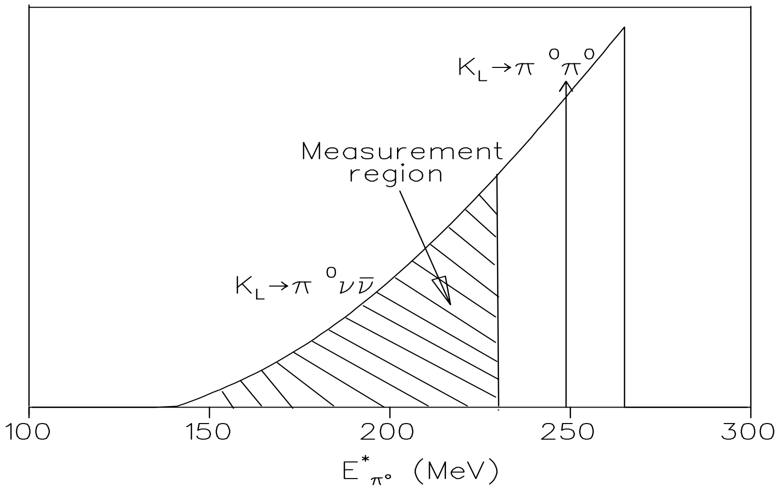

Figure 6: Energy spectrum of π^0 in the K_L center of mass frame (left).

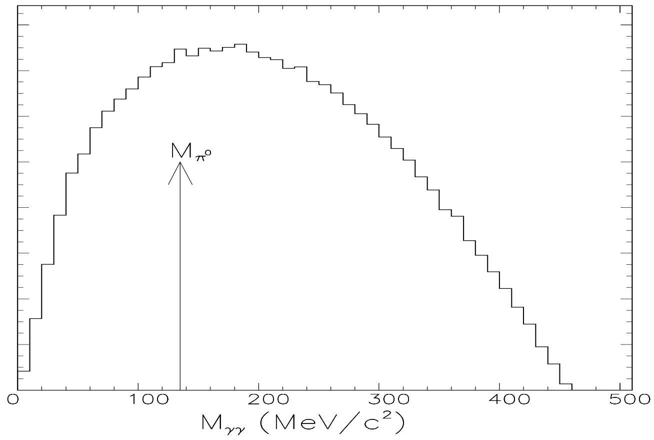

Figure 7: The 2-gamma mass spectrum ($M_{\gamma\gamma}$) for "odd-pairing" gammas in $K_{\pi 2}$ decays.

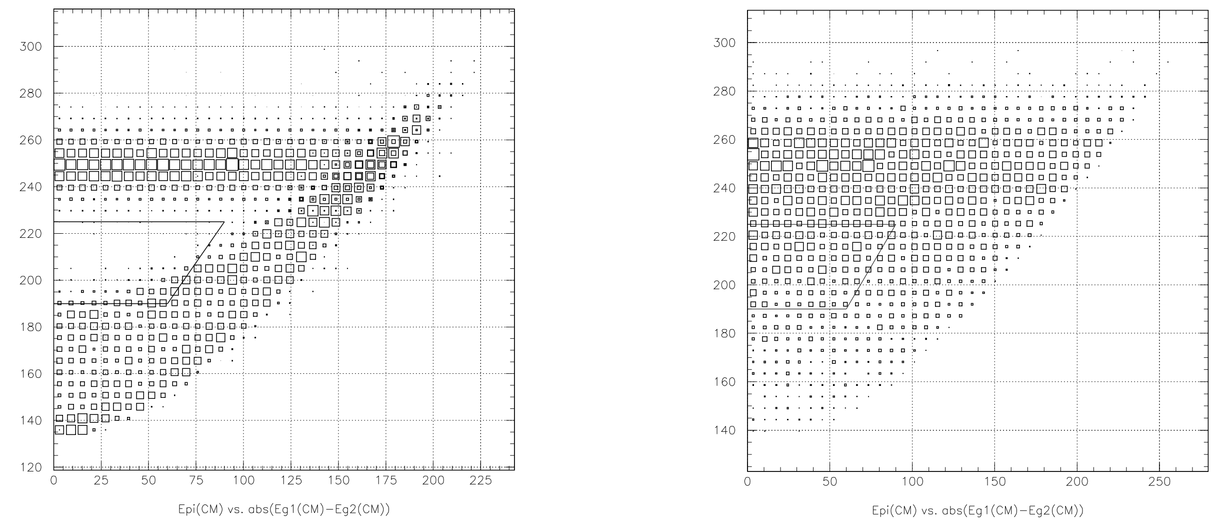

Figure 8: Distributions of $E^*_{\pi^0}$ vs. $|E^*_{\gamma 1} - E^*_{\gamma 2}|$ after π^0 mass requirement for the $K_L \to \pi^0\pi^0$ (left) and for the signal (right). The solid line encloses the signal region.

1.4 AGS

1.4.1 Primary beam luminosity

In recent years the AGS has achieved new records of intensity for synchrotrons. The present SEB peak extraction current has reached $> 7 \times 10^{13}$ protons/pulse. Further improvements are expected to bring this intensity to 10^{14}[31]. For estimates here we will assume this entire intensity will be available for K_L production. Coupled with a high current micro-bunched beam, good duty factor and extended availability during the RHIC era,[3] the AGS is the ideal accelerator site for rare neutral kaon decay experiments employing time-of-flight.

1.4.2 Bunched beam

Short ($\sim$ 200ps) bunches of protons on the kaon production target are desired so that the time-of-flight measurements can result in a few % momentum resolution in the experimental configuration described above. The straightforward expedient of keeping the beam bunched in RF buckets and compressing them would require excessive voltage to make the bunches this short. The method[32, 33] chosen here involves the following three steps: 1) With constant field in the main guide magnets, power an RF cavity that creates a string of empty RF longitudinal buckets around the AGS at a radius outside a de-bunched, coasting beam; 2) Set the radius of the extraction transverse resonance at the radius of these empty buckets; and 3) Force the protons in the coasting beam between these buckets by slowly reducing the main guide field. As extraction occurs where the beam is being forced between the separatrix lines of the empty buckets at the point at which they are closest, the extracted beam has the desired structure.

This concept has been tested at the AGS, exploiting a VHF acceleration cavity that is normally used to dilute the beam in longitudinal space. It operates at about 93 MHz with $\sim$ 30 KV across the gap. For bunched extraction it is powered after the beam is accelerated to full energy and the main field is fixed. This creates 251 empty buckets, every 3.35 m around the AGS, with an energy width of 20 MeV. The guide field is then reduced at a rate of about 0.4%/sec. The resultant stable phase angle is 0.5^o and the gap between buckets is 15^o or 0.5 ns. The frequency of the cavity is also ramped down, since the momentum of the extracted protons is falling with guide field (this frequency change is $\sim$ 1 part in 10^5). The motion through this gap is highly non-linear; tracking of particles in simulations[33] indicate the RMS width of a bunch forced between buckets with this configuration should be $\sim$ 160 ps.

During the 1995-7 SEB runs, initial tests of this concept were carried out using a number of different beam and detector configurations. Secondary particles were timed against the RF acceleration voltage, and the frequency was adjusted to minimize bunch width. Fig 9 shows the distribution of particle times from the most recent test. A Gaussian fit extracts an RMS width of $\sim$ 280 ps.

Widths are still somewhat larger than expected, but the present results are extremely encouraging. Further progress is expected as the instrumentation and feedback circuitry is improved. For use in the proposed experiment, a new cavity with a lower frequency will

---

[3]RHIC is projected to operate for 30 to 40 weeks per year and requires injection from the AGS for $\sim$ 2 hours/day. Thus, approximately 22 hours/day are available for AGS proton operation.

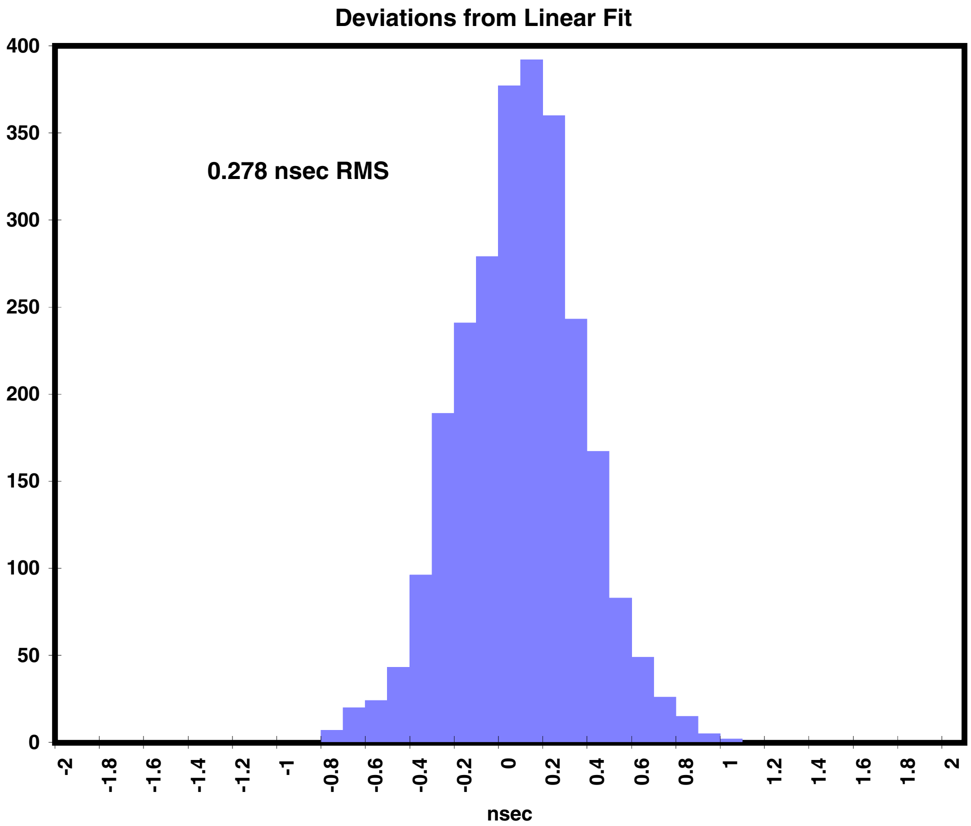

Figure 9: Time in E864 beam Čerenkov with respect to RF timing.

be built. Since the minimum RMS bunch width goes as $\sim V^{-\frac{1}{2}}$, we propose to commission a 100 KV, 20 MHz cavity. This is well within the reach of current technology and can be expected to reach a level of < 150 ps which would be more than adequate for our purposes.

1.5 Beam

KOPIO requires a copious source of K_L^0 of momentum 700 MeV/c. Ideally the spectrum should be peaked around this value with outlying tails as small as possible. A reasonable approximation to such a spectrum can be obtained from a 24 GeV/c primary proton beam if the neutral channel is taken off at a large angle ($\sim 40^o - 45^o$). Such a beam also has the advantage of a very low rate of surviving hyperons (potentially a serious source of background). However because there are a lot of neutrons in this kind of beam, care has be taken in the design of collimation and vacuum systems.

1.5.1 Particle production

K_L production

There is relatively little data on particle production in the region of interest, and the programs and parameterizations that address it tend to disagree significantly among themselves. Fortunately, there does exist a relatively recent, high-quality measurement of $K^\pm$ production by 14.6 GeV/c protons at angles from 5^o to 58^o[34]. These measurements were taken with thin nuclear targets (Be, Al, Cu, and Au). Since KOPIO envisions running at 24 GeV/c and using a 10.6 cm Pt target, these results require correction for the increased primary energy (+30%), and for the $1.2\lambda_I$ target. The latter correction arises from three effects: the extinction of the beam, absorption of K^+ in the target, and secondary K production. As will be discussed below, these effects tend to cancel, and the residual is about the same size as that of the primary energy correction, but of opposite sign. We assume that the K_L^0 cross section can be satisfactorily approximated by the average of the K^+ and K^- cross sections, and that production off Au and off Pt do not differ significantly.

The extrapolation in primary energy is done in four steps[35]. (1) Invariant $K^\pm$ cross sections from pp collisions are fit to the phenomenological form[36, 37]:

$$E_{K^\pm}\frac{d\sigma(pp \to K^\pm X)}{d\mathbf{p}_{\mathbf{K}_\pm}} = B(s)(1-x_R)^{n(s)}e^{b-\sqrt{b^2+c^2(s)p_T^2}} \tag{5}$$

(2) Assuming that in the interaction of protons with light nuclei, kaon production is dominated by single inelastic interactions of the primary proton with the nucleons, the pp cross sections are multiplied by a phenomenologically determined function of $\mu(p_K) \equiv \sigma_{Kp}^{inel}(p_K)Z + \sigma_{Kn}^{inel}(p_K)N$ and $\mu(p_0) \equiv \sigma_{pp}^{inel}(p_0)Z + \sigma_{pn}^{inel}(p_0)N$ to obtain the cross sections off Be. (3) The results of (2) are multiplied by a factor $(A_{Pt}/A_{Be})^{\alpha(x_F)}$ to get predicted cross sections off Pt. (4) The predictions are rescaled by comparison with data taken in the forward direction at 23.1 GeV/c[38].

The predictions are then compared with the Au data of Abbott *et al.* for $K^\pm$ production. Fig. 10 shows the data for K^+ production for $\theta = 40^o$ and 45^o and the corresponding predictions from the above procedure. Fig 11 show similar plots for K^- production.

We are now in a position to confidently extrapolate to 24 GeV/c. For $\theta \sim 40^o$, for example, this correction turns out to be about 30% on average (it is a function of p_K). The extrapolated K^+ and K^- cross sections are averaged, giving the results of Fig. 12.

To obtain yields, these cross sections must be integrated over the beam aperture and corrected for finite target effects. Beam attenuation in the target results in an effective

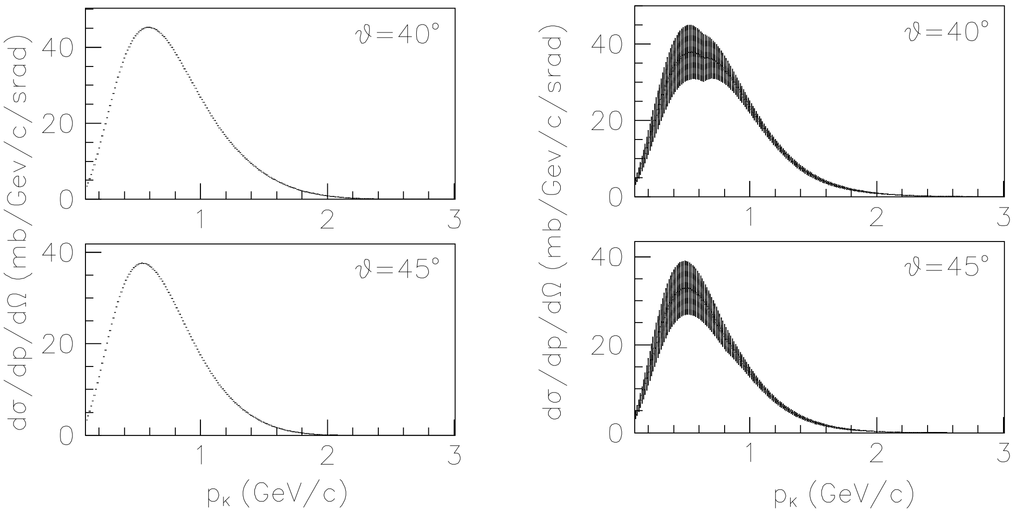

Figure 10: The right hand graphs are double differential inclusive cross sections for K^+ production by 14.6 GeV/c protons on Au at $\theta = 40^o$ and 45^o. The error bars show statistical uncertainties only. The left hand graphs are predictions from the procedure described in the text.

target thickness of $(1 - e^{-10.6/8.8})8.8\,\mathrm{cm} = 6.2\,\mathrm{cm}$. This represents an effective reduction factor of 0.58 with respect to thin target results. The effect of K^+ and secondary production in the long target was calculated via GEANT. Although we don't trust this program to yield reliable absolute yields, it should give a reasonable estimate of the thick target effects. GEANT runs on 0.5 cm and 10.6 cm targets were made[39]. The resultant correction factors varied significantly with production angle, but were very weak functions of p_K. For $\theta = 40^o$, this factor equals 1.32. For $\theta = 45^o$, it is = 1.36. Thus the product of all corrections is very close to 1 in the region of interest.

After applying all corrections, the yield and production spectrum of K_L^0 are obtained. For 10^{14} protons incident on the target, a total of 6.6×10^8 K_L^0 are produced into a 500 μsr solid angle centered at 40^o. After a reduction of 35% due to the photon spoiler discussed below and the loss due to decays in flight, 2.6×10^8 K_L^0 arrive at the detector 10m downstream of the production target with the momentum spectrum shown in Fig. 13.

Neutron production

Simulations and data on neutron production at large angles are also problematical. Therefore a new measurement was made [40] in the B1 beam line at the AGS. Fig. 14 shows a sketch of the set-up used in the measurement of the neutral particles: the beam counter arrangement, TOF scintillator wall and BaF_2 detector.

A small fraction of the 24 GeV/c AGS primary proton beam was extracted into the B1 line. A 10 cm long by 4×4 mm^2 cross section platinum production target was placed at the apex of the E802 spectrometer [41]. A beam spot of 3×3 mm^2 was determined by a small plastic counter (finger counter) placed very close to the front of the target. The TOF1 and TOF2 counters located upstream of the target, the finger and steering counters defined the

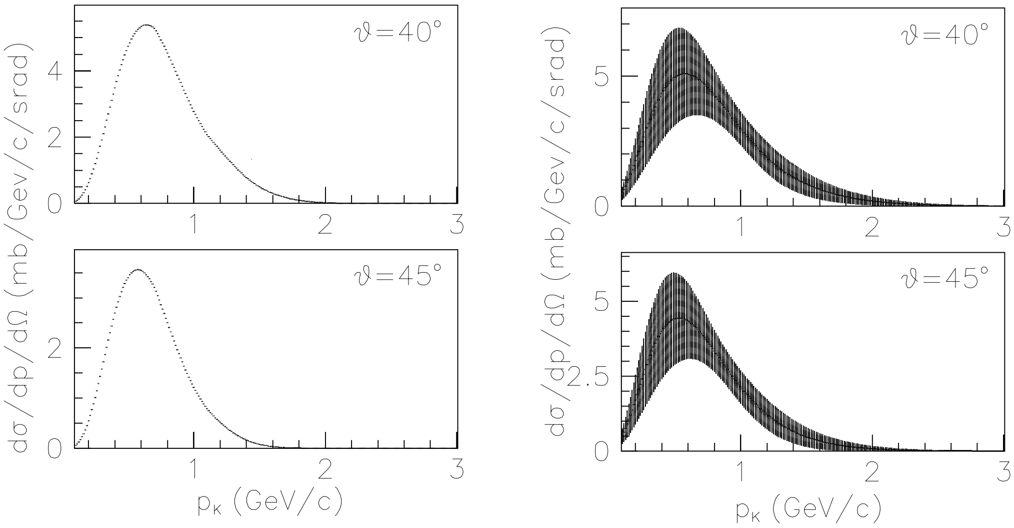

Figure 11: The right hand graphs are double differential inclusive cross sections for K^- production by 14.6 GeV/c protons on Au at $\theta = 40^o$ and 45^o. The error bars show statistical uncertainties only. The left hand graphs are predictions from the procedure described in the text.

geometry of the proton beam.

An array of 36 modules of BaF_2 was used to detect neutrons and photons. The detector was assembled to form a 6x6 array. Each module had a 3.5 cm x 3.5 cm cross section and was 35 cm in length. Each crystal was coupled directly to a fast phototube. The array was placed at a distance of 7.4 m from the target at the rotating spectrometer platform behind the plastic time-of-flight (TOF) wall, as shown in Fig. 14. The BaF_2 detector covered the area of about 440 cm^2, or approximately 6.4×10^{-5} of 4π solid angle.

To reject charged particles which hit the BaF_2 detector, and to form a neutral trigger two veto counters were used: a) a large counter (Int) behind the target (about 0.5 m), b) a veto counter (V_{BaF_2}) in front of the BaF_2 array.

The neutral trigger (NT) required a single beam particle to pass through the beam counters with no particles in the veto counters plus a signal in the BaF_2 detector during the time window of about 200 ns. The neutral trigger was formed as

$$\mathrm{NT} = \mathrm{TOF}_1\times \mathrm{TOF}_2 \times \mathrm{Finger} \times \overline{Int} \times \overline{V_{BaF_2}} \times \mathrm{BaF}_2$$

A time-zero signal used in the off-line analysis is obtained from the two photomultipliers of TOF_2 as

$$\mathrm{T}_{start} = 1/2(\mathrm{TOF}_{21} + \mathrm{TOF}_{22}).$$

The number of protons on the Pt target was calculated as a triple coincidence:

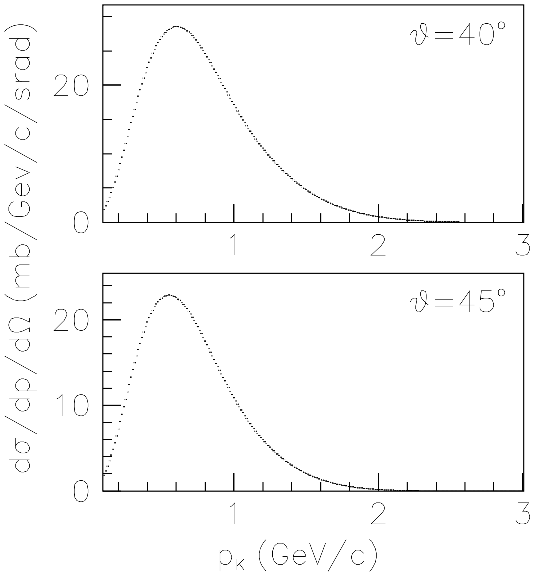

Figure 12: Calculated double differential inclusive cross sections for K_L^0 production at 40^o and 45^o by 24 GeV/c protons on Pt.

TOF1×TOF2×Finger.

The timing in the BaF_2 detector was defined as the TDC time of the crystal which had the maximum energy deposit. The TDC scale (resolution of 50 ps/channel) allowed us to measure a time interval of 200 ns, corresponding to neutron energy of less than 10 MeV. The timing shifts between the photon prompt peaks for different crystals were corrected in an off-line analysis. The timing resolution of BaF_2 varies from 200 to 400 psec (σ) and depended on the type of the PMT used (two types were used). There is also some contribution to the time resolution from the beam counters. After applying a time-amplitude correction in the off-line analysis, a time resolution of 0.55 ns (σ) was achieved for the whole BaF_2 assembly.

Deposited energy was calibrated via tracks identified as minimum ionizing by the TOF wall. Time calibration was based on the position of the prompt photon signal.

Fig. 15 shows a typical energy vs TOF spectrum. The prompt peak position corresponds to the photon time-of-flight from the target to the BaF_2. Neutrons with higher energies (closest to prompt peak) have larger energy deposits in the BaF_2 detector, as seen in Fig. 15. However since the BaF_2 array is only a fraction of an interaction length deep, deposited energy is not a very good estimator of the true neutron energy (although it is fine for photons). Therefore the neutron energy was calculated from time-of-flight information. To get final neutron energy spectra, a flat background was subtracted from the TOF spectra, determined from the hits that precede the prompt peak. Spectra so derived for the $\theta = 38.5^o$ and 46.5^o settings are shown in Fig. 16.

To obtain the true neutron flux, the absolute efficiency of the BaF_2 detector for detection of fast neutrons is needed. Such an efficiency was measured in Refs. [42, 43]. For $E_n \geq$ 100 MeV Ref. [43] gives a neutron efficiency $\epsilon_n \sim$ of 0.25 - 0.3 for 25cm thick crystals. For neutron energy below 40 MeV the efficiency is less than 0.2 and falls to about zero for

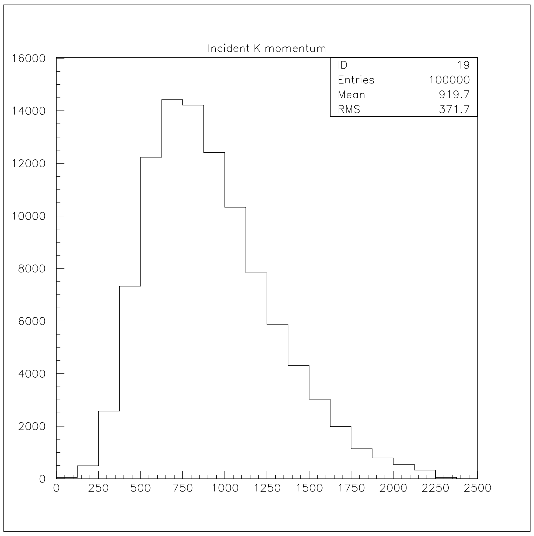

Figure 13: K_L^0 spectrum incident on KOPIO decay volume.

neutron energy of ≤ 15 MeV [42]. The uncertainty in the BaF_2 efficiency limits the accuracy of the measurement of neutron flux, especially at low energies, but it is good enough for our purposes. Since our crystals are 35cm deep, we must correct the above efficiencies upward, by a factor $(1-e^{-35/L_{int}})/(1-e^{-25/L_{int}})$. The Particle Data Book[44] gives 29.6 cm for L_{int}, which implies a correction factor of 1.22.

The photon yields are more straightforward to extract. The photons are selected by timing and the calibrated energy is used directly. The extracted neutron and photon yields measured at 38.5^o and 46.5^o are given in Tables 2 and 3. The results on neutrons agree reasonably well in total yield with the predictions of GEANT/GCALOR, but the observed spectra are somewhat harder than those of the simulation.

Table 2: Neutron and photon yield at 38.5°. The total number of protons on target is 20.6×10^6. Corrections for DAQ dead time (16 %) and BaF_2 efficiency have been made.

Threshold, MeV	10	50	100	300	830
n/p	2.03×10^{-3}	1.69×10^{-3}	1.46×10^{-3}	0.89×10^{-3}	0.35×10^{-3}
n/γ	2.18	3.43	4.08	4.05	3.88

Table 4 recasts the above results in a normalized form. One can use this table to estimate the neutron and photon (pre-spoiler) fluxes in KOPIO. In fact the solid angle coverage of the BaF_2 is only about 60% larger than that of the KOPIO beam. For a proton beam intensity of 10^{14} protons/pulse on target, at 38.5^o, the neutron flux above 10 MeV is 1.26×10^{11}/pulse. For 46.5^o, the corresponding number is 8.3×10^{10}. For neutron energy above 830 MeV, the flux decreases by a factor $20-30$ at 46.5^o and by a factor $5-6$ at 38.5^o. For photons, the flux above 10 MeV is 5.75×10^{10}/pulse at 38.5^o and 2×10^{10}/pulse at 46.5^o. As we discuss

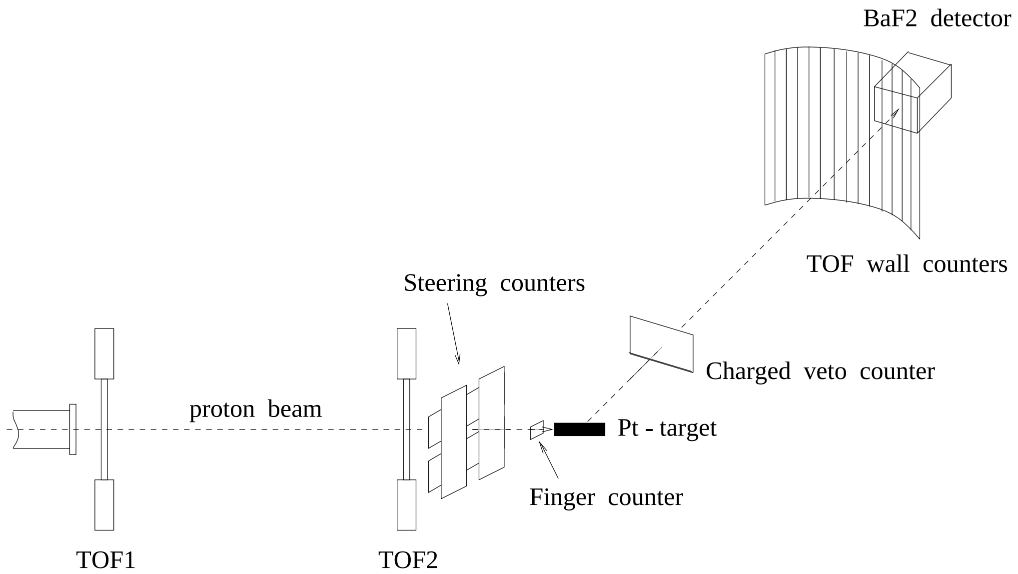

Figure 14: The configuration of beam counters, TOF wall and BaF_2 array. The charged veto counter is referred to as "Int" in the text. V_{BaF2} is not shown.

Table 3: Neutron and photon yield at 46.5°. The total number of protons (p) on a target is 60.5×10^6. Corrections for DAQ dead time (16 %) and BaF_2 efficiency have been made.

Threshold, MeV	10	50	100	300	830
n/p	1.35×10^{-3}	1.02×10^{-3}	7.96×10^{-4}	3.09×10^{-4}	0.52×10^{-4}
n/γ	4.19	4.88	4.98	3.98	3.06

below, this can be greatly reduced by an appropriate photon spoiler system. The neutron flux will also be reduced, although only by a factor ≤ 2, by such a spoiler.

1.5.2 Beam design simulation

Beamline design for KOPIO has several objectives. Charged particles emanating from the production target must be swept out, the photon component of the beam must be highly suppressed and beam neutron halo must be kept well below 10^{-3}. A number of Monte Carlo studies using GEANT3/GCALOR have been performed to optimize a design to meet these objectives.

The geometry of the beam line (the target, proton beam direction and the collimator are shown in Fig. 17. For the purposes of this study the target was taken to be 2mm square in cross-section and 10 cm long. A series of precision collimators (Fig. 17) are used to define the asymmetric neutral beam of solid angle 5.2 mr (V) x 96 mr (H) = 500 μsr. (Early studies were done with collimation directed at producing a 4 mr vertical by 125 mr horizontal beam cross-section.) The horizontal and vertical apexes of the collimator coincided. Studies with

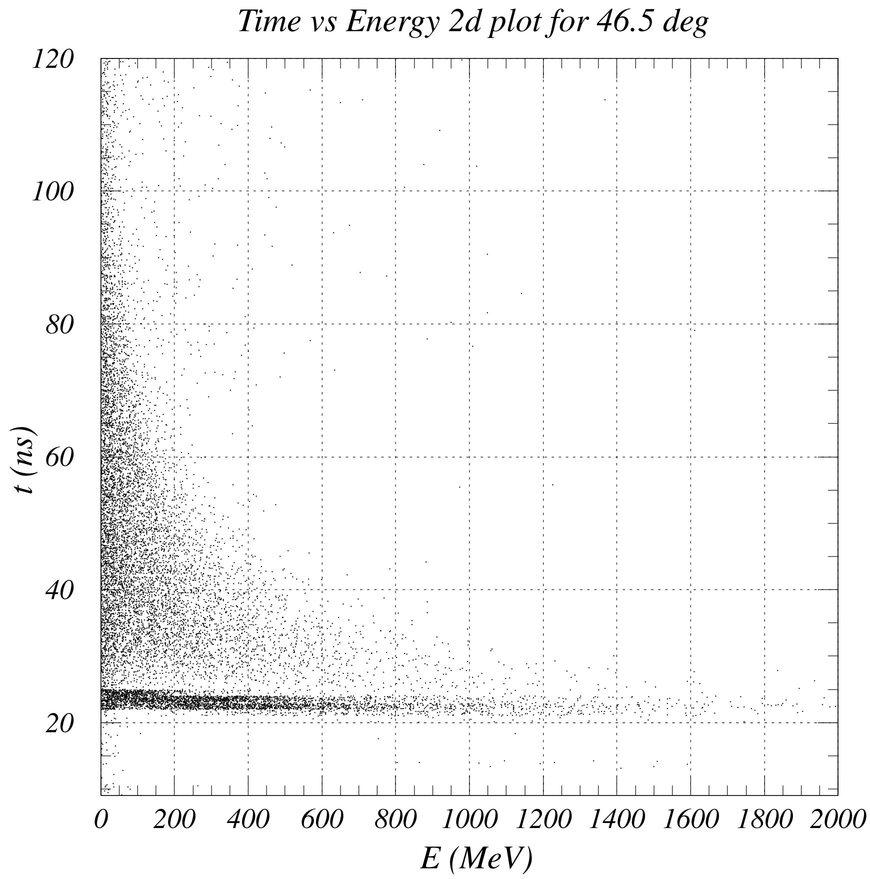

Figure 15: Time vs energy for $\theta = 46.5^o$ setting.

both tungsten and lead as collimator material were done. Herein we report on results with an all-lead collimator. This leaves scope for further improvement through the use of tungsten at critical points. The beamline was simulated by GEANT3/GCALOR. To save computer time the simulation of the neutron production was separated from that of its propagation. Two types of calculations were made. (1) Primary proton interactions were generated by GEANT3/GCALOR and the resulting neutron and proton spectra determined. Neutrons and protons were selected from these distributions and followed into the beamline. (2) Neutrons were generated according to our measured spectra and followed into the beamline. In both cases the subsequent history of the particles was followed by GEANT.

To reduce the high flux of beam photons a lead filter ("spoiler") was installed in the collimator. The filter is a stack of 50 (70) Pb foils 1 mm thick and 2 (or 3) cm apart. It completely covers the beam hole in the collimator. The first foil is located at 1 m from the target, and the total length of the filter varies from 1 m to 2.1 m. To remove positrons and electrons from the beam aperture a horizontal magnetic field was applied. The field is

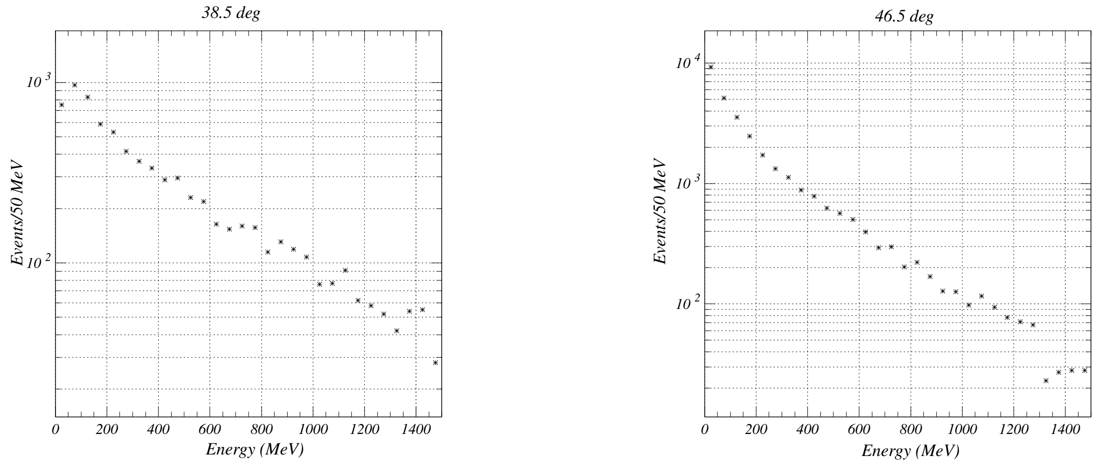

Figure 16: Extracted neutron energy spectrum at 38.5^o (left) and 46.5^o (right). The bin size is 50 MeV.

Table 4: Normalized neutron and photon yield.

Angle	Particle	Threshold, MeV	Flux ($p^{-1}\mu sr^{-1}$)
38.5^o	neutron	10	2.52×10^{-6}
	neutron	100	1.78×10^{-6}
	photon	10	1.15×10^{-6}
46.5^o	neutron	10	1.66×10^{-6}
	neutron	100	1.04×10^{-6}
	photon	10	0.40×10^{-6}

envisioned as beginning at the upstream edge of the first collimator and extending downstream for 2m. (Point 1 to Point 2 on Fig. 17). The dependence of photon intensity in the beam catcher on magnetic field is shown in Fig. 18 for lead thickness of 5 cm and 7 cm. A reduction of the photon flux by a factor of 150-200 is possible for 7 cm of lead with B = 1.5T. One gains very slowly with B beyond this point. Moreover the photon spectra becomes much softer after the filter, as seen in Fig. 19. The ratios of neutral kaon decays with and without the filter are 0.70 for 5 cm of lead and 0.62 for 7 cm. The corresponding factors for beam neutrons are 0.72 and 0.65. Unlike the photon case, neither the neutron nor the kaon spectra are much affected by the presence of the filter.

Neutron halo studies were made by both methods described above. Nucleons were started in the target within a solid angle of 30 mrad (vertical) x 280 mrad (horizontal) that is much wider than collimator-defined acceptance and allowed to hit the the collimator front face. We ran 10^7 neutrons from the target to the collimator in each run. A low energy cutoff parameter of 10 MeV was used, i.e. a neutron was stopped at the point where its energy was reduced to $\leq$10 MeV. The resulting distributions at various points along the beam were used to optimize the collimator design. This is a continuing process, but results thus far are

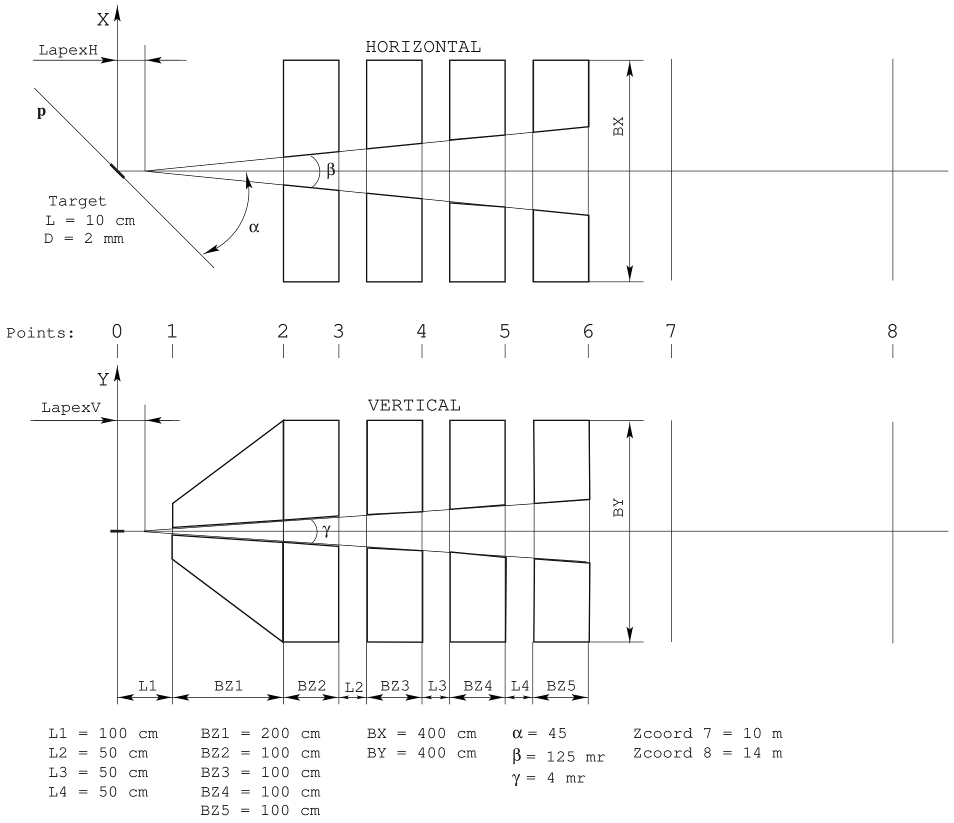

Figure 17: Schematic view of the neutral beam line. The baseline calculations are for LapexH = LapexV = 0.

very encouraging. Fig. 20 shows the x and y projections of the neutron beam at a point 14m downstream of the production target in the type (1) calculation. The fraction of neutrons in the halo, defined as the region more than 1 cm vertically and 3 cm horizontally out of the beam profile, is 4.8×10^{-4}.

Fig. 21 gives the corresponding results for the type (2) calculation. Here the fraction of halo neutrons is 5.0×10^{-4}, very similar to the type (1) calculation. However it must be corrected for the contribution of protons. The correction factor can be determined in type (1) calculations where the fractional proton contribution is observed to be only a few percent. Assuming that this ratio is only a weak function of the nucleon momentum, the total halo in the type (2) calculation is only slightly higher than in the type (1) calculation. The beam halo fraction at 40^o is about a factor two higher than that at 45^o.

Beam optimization continues. The addition of an extra 0.5m of Pb shielding reduces the halo fraction at 40^o to 3.9×10^{-4}, which is already very promising. To meet our trigger rate goals, another factor ~ 2 will be needed. Calculations with a 4 mr x 105 mr beam aperture yield a factor 2.5 smaller halo at the cost of roughly 20% in beam flux. Moving the target 20cm upstream of the apex of the collimators reduces the halo by a factor 2 at the cost of

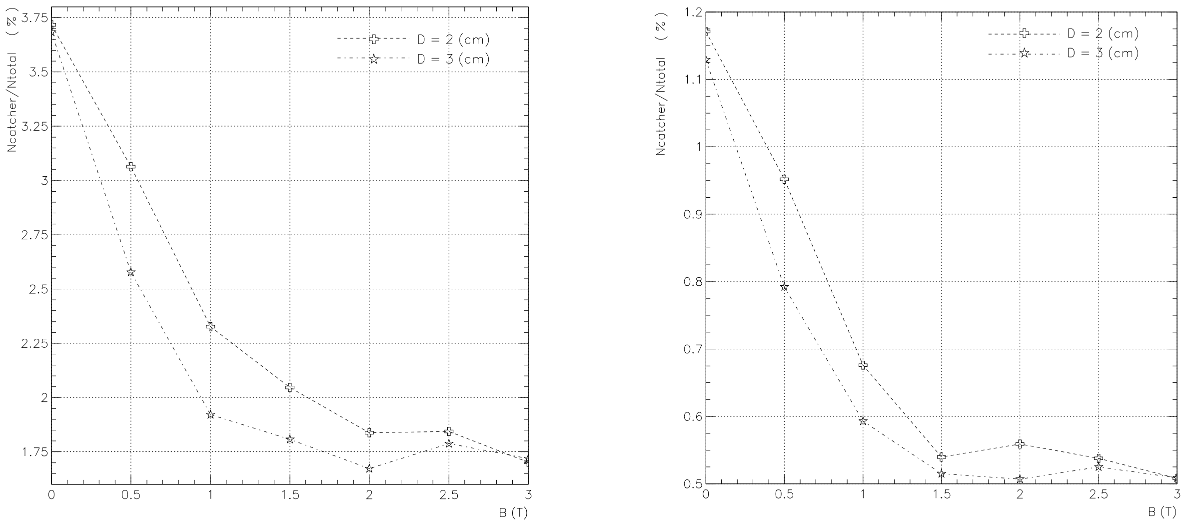

Figure 18: Fraction of photons penetrating filter, versus sweeping magnetic field. Cases of 2 and 3 cm foil separation are shown. Left graph is for the case of a total Pb thickness of 5cm. Right graph is for 7 cm.

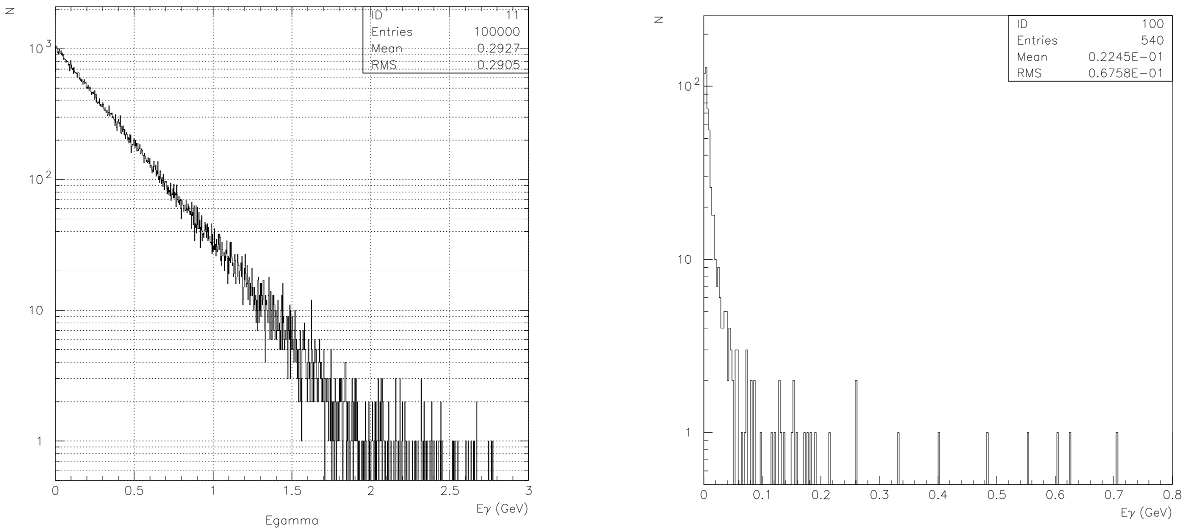

Figure 19: Photon spectra in the collimator-defined aperture before (left) and after (right) a 7 cm Pb filter with B = 1.7T.

13% of beam intensity. Substitution of tungsten for lead in critical regions yields a 15-20% benefit. Based on these studies, we expect to be able to achieve 10^{-4} integral halo at 40^o.

As a test of our methods, the AGS-791/871 beamline [45] was also simulated, and the halo profiles obtained matched available data [46].

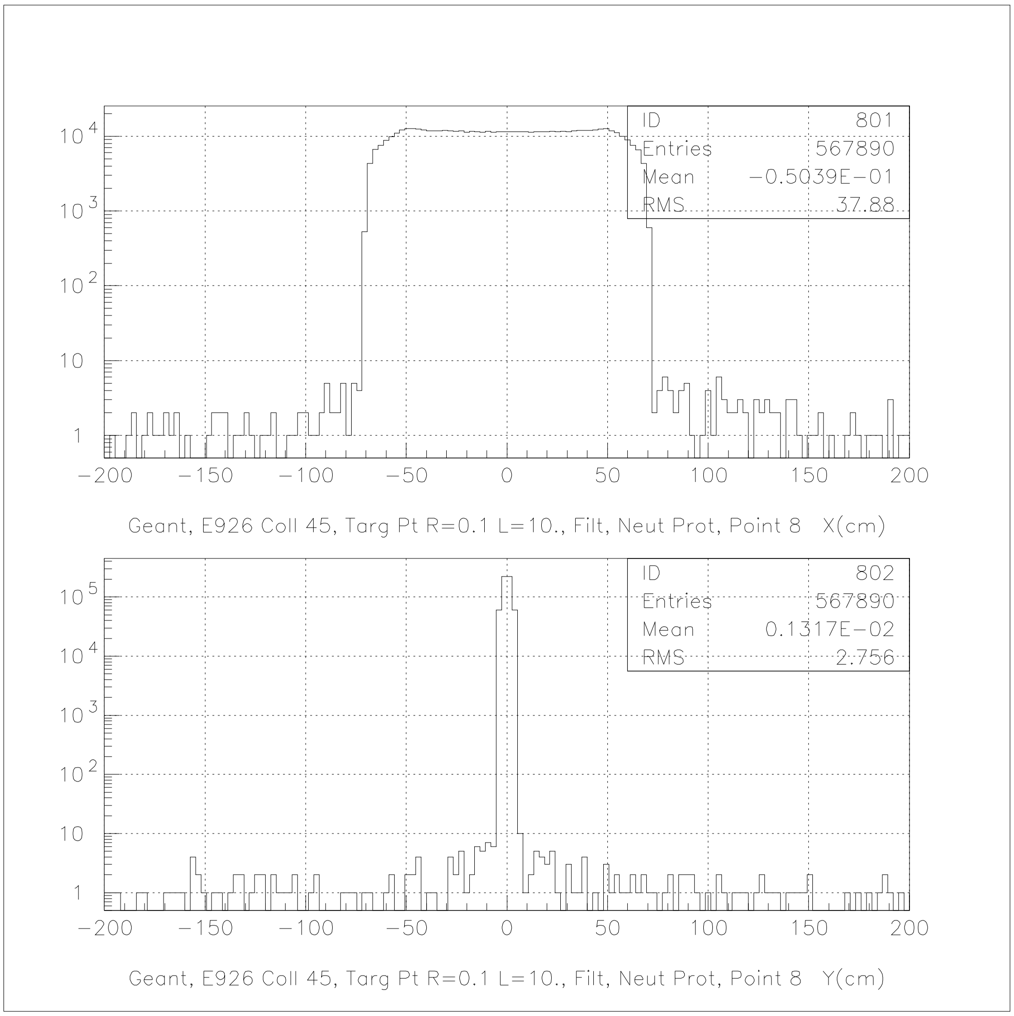

Figure 20: The x (top) and y (bottom) projections of the neutron distribution 14m downstream of the production target for $\theta = 46.5^o$. Gamma filter = 7cm, B= 1.5T. Calculation begins with neutron and proton distributions from GEANT3/GCALOR.

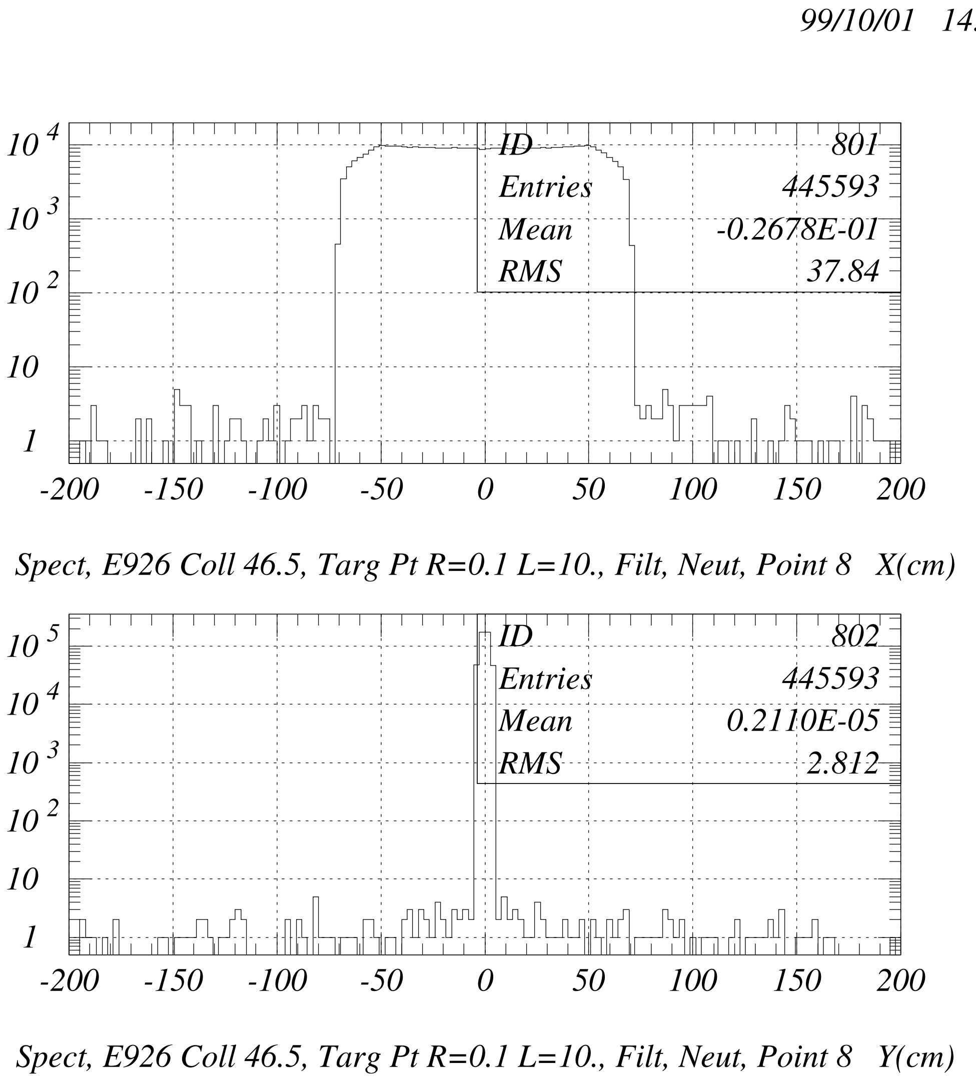

Figure 21: The x (top) and y (bottom) projections of the neutron distribution 14m downstream of the production target for $\theta = 46.5^o$. Gamma filter = 7cm, B= 1.5T. Calculation begins with measured neutron distributions.

1.6 Vacuum and Mechanical considerations.

Figure 22 shows the basic vacuum elements of the apparatus in the experimental area. The beam is in vacuum all the way from the target to the left of the drawing to the exit of the downstream pipe in front of the "catcher" to the right.

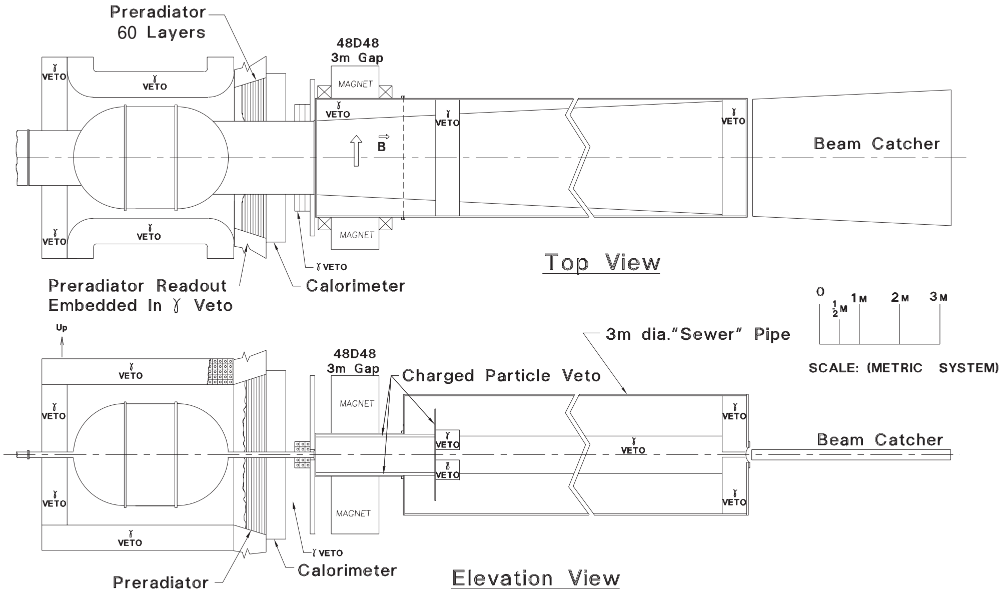

Figure 22: Plan and elevation views of the experimental apparatus. The beam enters from the left in a vacuum system that begins at the target.

1.6.1 Vacuum in the decay region.

The decay volume and the entire beam path within the view of the detector must be at high vacuum ($\sim 10^{-7}$ torr) in order to suppress background from neutron and K^0 interactions with the residual gas. The walls of the vacuum containment must also be of minimal material ($\leq$ 5% X_0) in order to reduce photon conversions and photon production from charged particles, for example in K_{e3} decays. Coupled to the fact that the beam has a high aspect ratio ($\sim$ 1 m horizontally by $\sim$ 5 cm vertically), these constraints provide a challenge to designing the vacuum containment in the decay region.

The vacuum vessel is shown in fig. 23. An engineering report on its design, including a finite element stress analysis, is presented in a KOPIO technote [47]. Possible vendors have been found to manufacture the vessel as described below.

The material from which the vessel is formed is a Graphite/epoxy laminate (Mitsubishi K137/954-3 or Amoco P75/954-3) which is about 1.3 cm thick, or about 5% X_0. The central region consists of two hemispherical shells 2.5 m in diameter joined by Graphite/epoxy composite material flanges to a central cylinder. The flanges also serve as tie points for carbon fiber wires which support the vessel from above and provide stability from below (not shown in fig. 23).

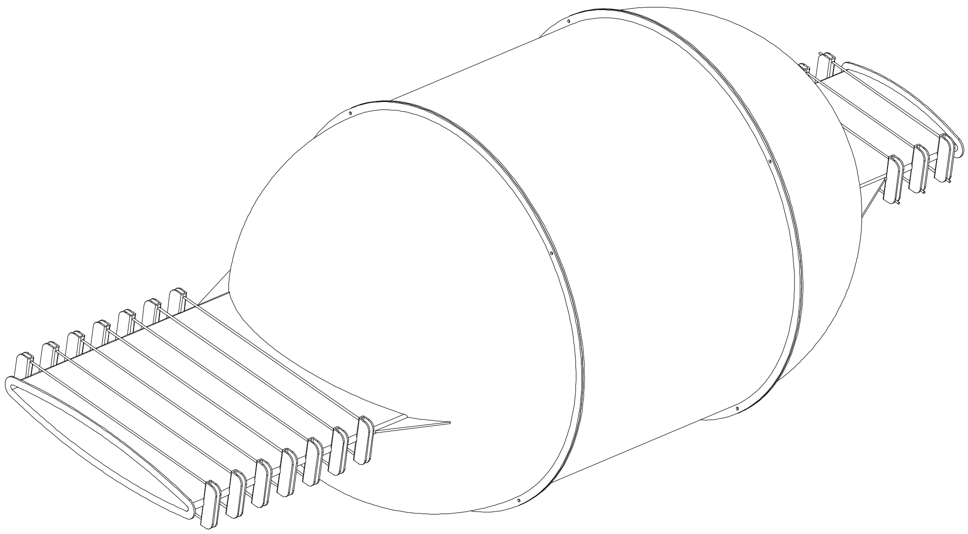

Figure 23: Drawing of the decay region vacuum vessel.

The beam pipes on either end of the hemispheres are connected to vacuum pipes upstream and downstream of the decay volume. These, in turn, are anchored to the floor. Thus, the large stresses on the vessel where the beam pipes join the hemispheres are taken up by the floor.

In order to provide sufficiently high vacuum, the inside of the vessel must be lined with metal. This can be accomplished by placing aluminum foil on the mandrels used for forming the vessel components before the graphite/epoxy material is applied, and curing the system in vacuum.

Directly upstream of the upstream γ vetos in fig. 22 is the pumping station for the decay volume vacuum. It is separated from the beam (dirty) vacuum upstream by a thin window. It consists of a box containing the necessary pumps plus an optical feed-through through which the fibers for the charged particle veto (housed inside the vacuum vessel) pass.

Because of the large horizontal to vertical aspect of the beam, the beam pipes deserve special consideration. They should be as close to the beam shape as possible to minimize the beam hole in the detectors, but must also be made of thin material (both in size and radiation lengths) to minimize absorption of photons or interactions of neutrons. The concept employed is to construct them as opposing arches with external supports (made of carbon fiber "wires" and carbon fiber material) to resist collapse from atmospheric pressure. This concept is also shown in fig. 23. The downstream end of the beam pipe is 160 cm at its widest extent and 20 cm high in the horizontal center. One of the advantages of using carbon fiber wire supports is that the preradiator panels can be shaped to fit closely to the beam pipe, thus maximizing the acceptance of the detector.

1.6.2 Vacuum and mechanical downstream of the decay region.

The region downstream of the decay volume (see Fig. 4), and just beyond the end of the calorimeter, the decay volume vacuum vessel ends with a thin window. Its flange is connected to a vacuum box that fills the downstream sweeping magnet. That vacuum box is in turn connected to a 3 m diameter, 13 m long cylindrical pipe which terminates in a 3m diameter end plate with an Al vacuum window that is roughly 280 cm wide by 15 cm high. The box and pipe have appropriate feed throughs for the various veto counters that are housed therein, as well as holes for pumping.

The sweeping magnet is a standard Brookhaven 48D48 with a horizontal 1 kG field and a 200cm gap. Between it and the calorimeter is a 10 cm thick magnetic shield with a 160 cm wide by 15 cm high slit through which the beam passes.

Beyond the vacuum region is the beam catcher which is described elsewhere.

1.7 Preradiator

The requirements of the preradiator (PR) include a photon angular resolution of approximately 25 mr, a photon conversion efficiency of about 0.7 (2.0 X_0), a good measurement of the deposited energy and as short as possible linear extent so as to limit shower size at the calorimeter. The principle we will employ is to measure the positions and angles of the first e^+e^- pair following photon conversion in a series of thin converter/detector modules. Each PR module consists of an inactive converter material, a dual coordinate drift chamber and a scintillator. The chambers provide the position measurements and the scintillation counters are used for triggering, timing, and energy loss measurement. To keep multiple Coulomb scattering (MCS) at the 25 mr level the PR modules each contain $\leq$0.034 X_0, are separated by about 1 cm and have position resolution of between 150 and 200 μm. In addition, the energy deposited in the preradiator will be measured with sufficient precision to allow the full energy measurement (including the PR and the calorimeter) to be better than $3.3\%/\sqrt{E}$

1.7.1 Design concept

We are considering two designs for the preradiator sub-elements. One scheme is based on a "honeycomb strip chamber" [48] with integrated scintillators illustrated in fig. 24. The system is based on proportional tubes made from corrugated, metalized kapton and metalized scintillators. The second system under study, shown in fig. 25, consists of flat square cell drift chambers with an extruded Al comb backplane and independent extruded scintillator elements similar to those to be used in the barrel veto detector. In both cases, the primary chamber readout will be done with the induced charge signals from 3 - 5 mm wide cathode strips (CS) strips running perpendicular to the anode wires at a 6 mm pitch. Measurement of the combined induced charge distribution on the CS will allow the best resolution to be obtained on the position of the e^+e^- pairs. The timing of the anode wire pulses will also be read out yielding the position of the initial track ionization perpendicular to the wire direction. The wire signals will be multiplexed using every other wire joined in groups of three to a single electronics channel. The preradiator modules will be oriented with alternating vertical and horizontal wires (horizontal and vertical CS).

In the honeycomb arrangement, when the three pieces shown in fig. 24 are joined two close packed rows of hexagonal tubes are formed. The cell size of each tube is 7 mm between parallel faces. The central foil has strips on both sides which are electrically connected. An attractive feature of this chamber arrangement is the nearly cylindrical geometry in which the strips cover half the circumference of the tubes yielding a larger induced pulse. Where the scintillators make contact with the foil they are not metalized; otherwise they are metalized and connected to ground. As an integral component of the tubes, the scintillators will be constructed precisely from injection molded plastic panels. The side facing the tubes will be formed to the corrugated shape of the tubes, adding mechanical strength to the tube structure. The opposite side will contain grooves every 10.5 mm into which will be placed wave length shifting (WLS) fibers for reading out the scintillators. The thickness of one module, including metal, foils, and scintillator, will be about 1.5 cm making the preradiator depth 90 cm.

The Al comb chambers may provide a simple compact preradiator with comparable performance. In this case, the cell size will be 5 mm x 5 mm with a maximum drift time of about 70 ns. The 0.5 mm thick Al strongback supports the wires strung through plastic end-pieces and crimp pins. The thickness of the cell divider fins is specified to be 250 μm and the tolerance on the overall flatness of the structures up to 4 m in length is of order 150 μm. For long horizontal wires, small plastic wire support pieces will be installed about every meter. Thin copper coated G-10 with etched cathode strips will be spaced 2.5 mm from the anode wires Extruded Al combs have been produced with the specifications indicated in fig. 25 by the Northern State Metal Corp.[49] The combs are mounted on 0.4 mm Cu plates which serve as the photon converter material. The CS foils are read out at the ends as in the honeycomb arrangement. Extruded scintillator of thickness 3 mm with grooves for WLS fibers every 1 cm has been tested to produce 8.5 p.e. for a single minimum ionizing particle. In total the modules are 0.9 cm thick providing 2 X_0 in 60 modules of 54 cm in depth.

Prototypes are being constructed of both systems mentioned above for evaluation.

In both cases, the majority of the modules are 4.5 m long, with 30 μm sense wires. Panels of size 4.5m x 4.5m will be constructed using 4.5m long 2.25m wide modules, with accommodation made for the beam slit. The fibers will be grouped into 16 cm sections within a panel. The orientation of the fibers will be, alternating along the beam direction (z): horizontal (yielding a y measurement), vertical (yielding an x measurement), and at 45° (termed v). The fibers will extend through one quadrant and be viewed at the appropriate outside edge. For triggering purposes, and to reduce the influence of phototube noise, four planes of sections with the same view, *i.e.*, x, y, or v, will be ganged together on a single phototube. The entire preradiator will consist of 60 panels with a total of approximately 50,000 wires (with their readout multiplexed by 3), 50,000 strips with analog readout, and 840 phototubes.

1.7.2 Readout

The anodes and cathodes from each preradiator panel will be read out and digitized individually at the chamber; only digitized information will be taken from the chamber area. Thus, the readout boards on the chambers will each contain the appropriate preamplifiers, discriminators (for time measurements), track and hold circuits (for analog measurements), multiplexing, and digitization circuitry. Because wire chambers are employed it will take several micropulses to accumulate the data from an event. A local trigger formed from regions of interest for the event defined by the scintillator readout arrangement described above will provide the appropriate gates for the chamber information which is to be passed on to the digitizers. Thus the expensive component of the system, *i.e.* the digitizers, will be heavily multiplexed.

1.7.3 Performance

We show in Fig. 26 the angular resolution of photons as determined by GEANT simulation of the preradiator with 3.4% X_0 per layer and assuming 150 μm position resolution for both the CS measurements of e^+e^- pairs and drift times of initially detected ionization. The resolutions (sigma) obtained are dominated by MCS and vary from 15 mr at $E_\gamma = 450$ MeV to 33 mr at $E_\gamma = 150$ MeV. Using position resolutions up to 350 μm worsened the angular

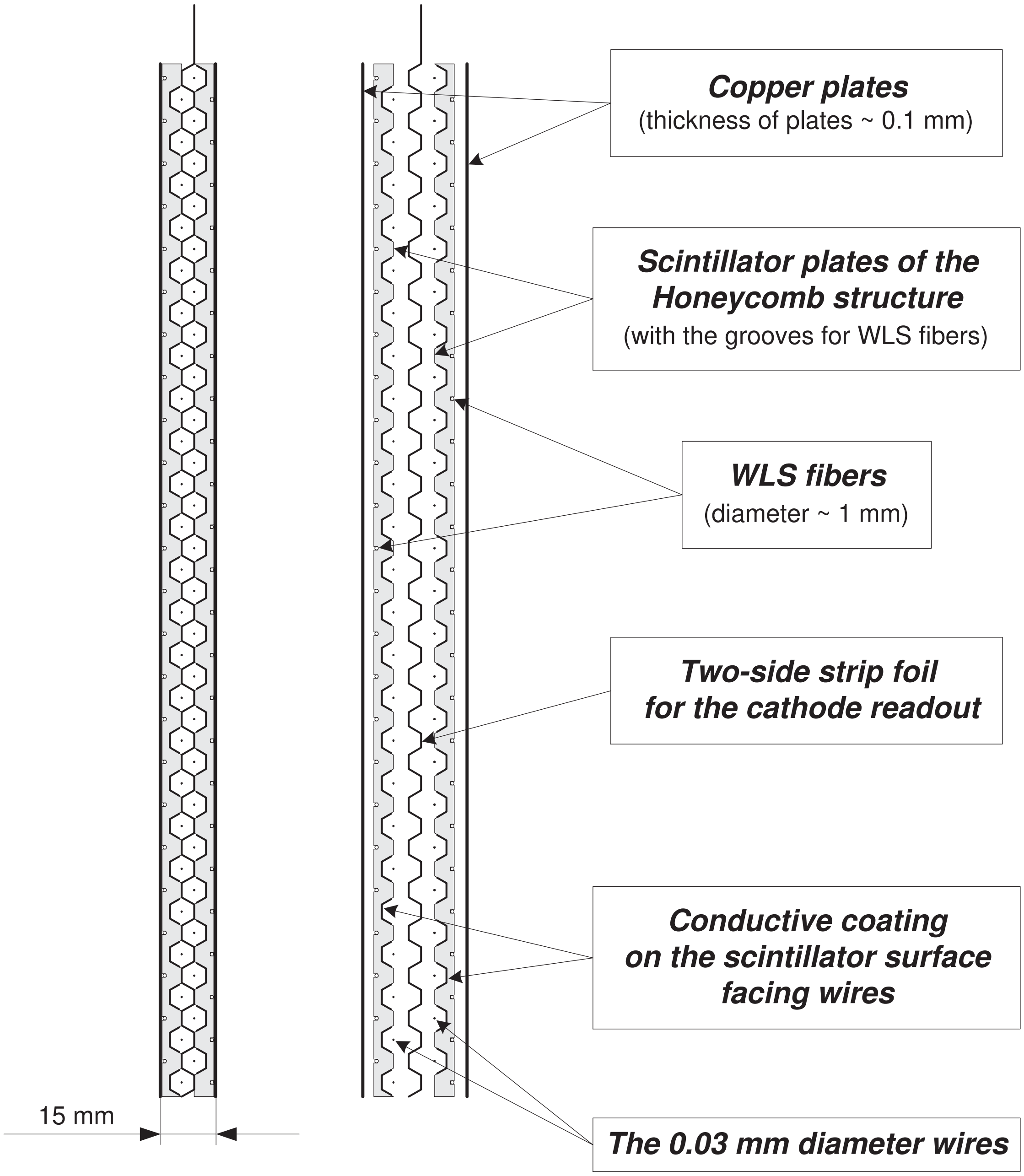

Figure 24: End view of the hexcell preradiator.

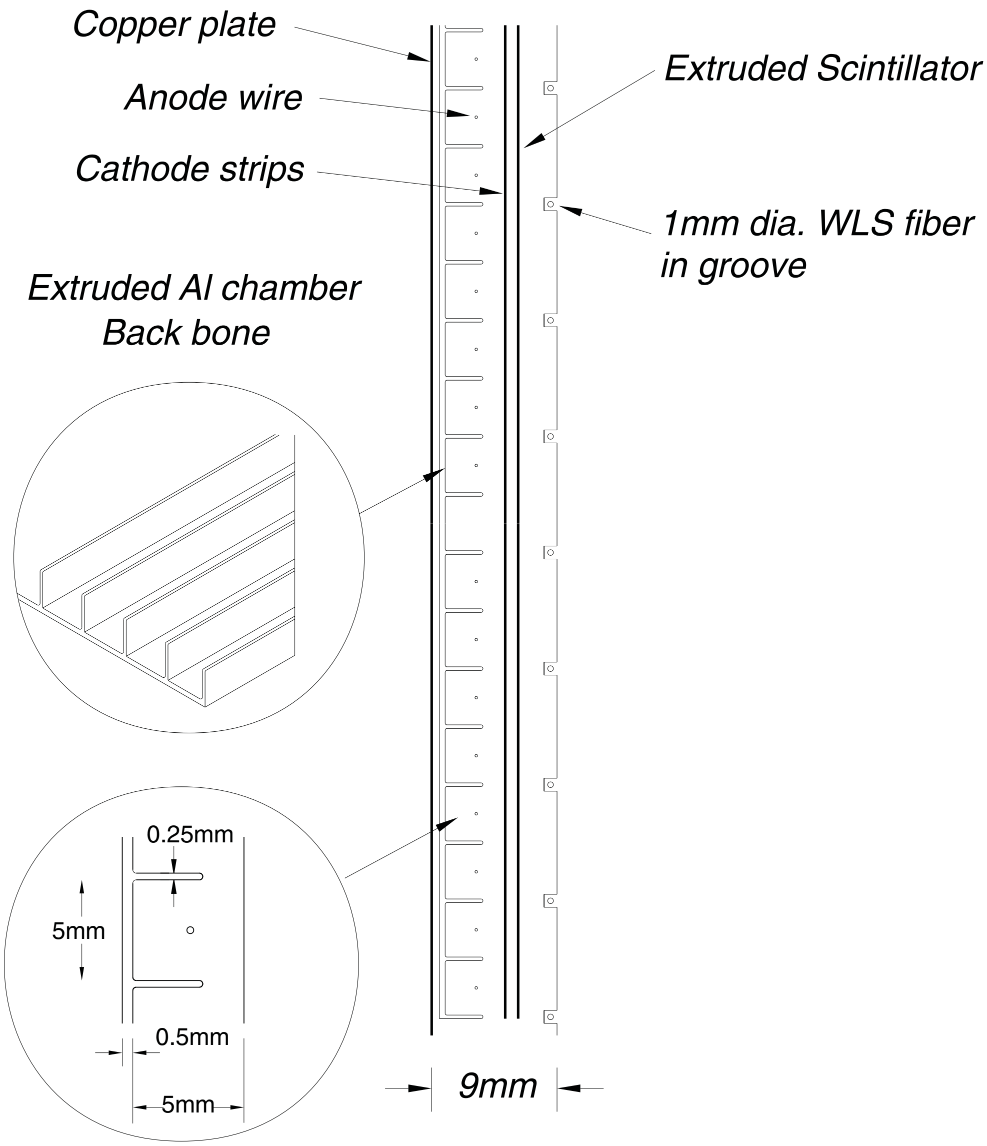

Figure 25: End view of the Al-backbone preradiator.

resolutions by about 10 %. The case shown uses anode drift time information from the first chamber struck by the e^+e^- pair and averaged position measurements from the CS of the second and fourth chambers hit. Subsequent evaluations of signal and backgrounds described in this report use preradiator resolutions generated in this manner.

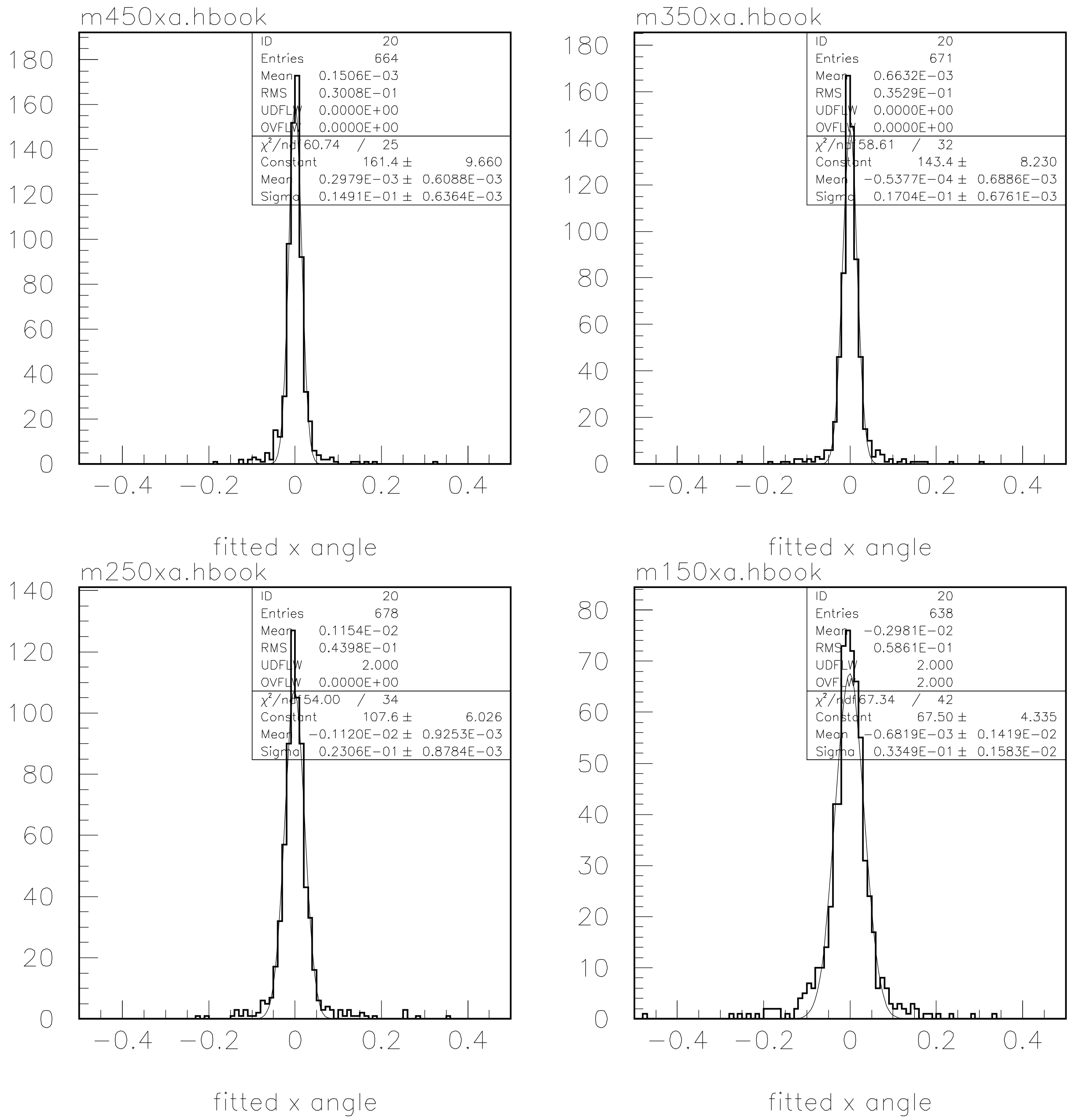

Figure 26: Preradiator angular resolution for various photon energies. GEANT results are shown for $E_\gamma = 450$ (top left), 350 (top right), 250 (bottom left) and 150 MeV (bottom right).

1.8 Calorimeter

In the KOPIO experimental configuration the endcap calorimeter occupies an area of 5.2x5.2 m^2 behind the preradiator. The optimization study described above and other considerations lead to the following requirements for the calorimeter:

1. Time resolution approximately 60 ps/ $\sqrt{E(GeV)}$,
2. Energy resolution 3-3.5%/$\sqrt{E(GeV)}$,
3. Granularity 10 cm.

To meet the specified requirements in an economical way we have chosen a Shashlyk based calorimeter. Such a calorimeter is composed of Shashlyk modules which are lead-scintillator sandwiches read out by means of wave length shifting (WLS) fibers passing through holes in the scintillator and lead. While we propose a module with significantly improved performance over previous incarnations, the technique is well proven, *e.g.*, E865 at Brookhaven [50], and has been adopted or is being considered by other experiments, *e.g.*, the PHENIX RHIC detector [51], the HERA-B detector at DESY [52], and the LHCb detector at CERN [53].

We have significant experience with the E865 calorimeter which is composed of 600 such modules and ran reliably in a higher rate environment than that expected in the KOPIO experiment. It is from that experience, and improvements which have been prototyped and simulated, that we draw our confidence that the design goals can be reached.

The E865 Shashlyk module has an energy resolution of 8%/$\sqrt{E}$. A new prototype module has been constructed, studied in a test beam, and measured to have a resolution of 4%/$\sqrt{E}$. Using this experimental study as a reference point for tuning Monte Carlo simulations, mechanisms for further improvements to achieve the desired performance have been determined and are described below. Details of measurements and calculations can be found in KOPIO technical note [54].

1.8.1 Prototype module

The design of a prototype module is shown in Fig. 27. Ten such modules were produced at TECHNOPLAST (Vladimir,Russia). The module is a sandwich of alternating perforated stamped lead and injection molded polystyrene-based scintillator plates. The crossectional size of module is 110×110 mm^2; the thickness of plates are 0.35 mm for lead and 1.5 mm for scintillator. Each plate has 144 equidistant holes in a 12×12 matrix, with the spacing between the holes being 9.5 mm. The diameter of the holes is 1.5 mm in the lead plates, while the holes in the scintillator have a conical shape with diameter ranging from 1.4 to 1.5 mm. 72 WLS fibers are inserted into these holes. Each fiber is looped at the front of the module, so that both ends of a fiber are viewed by the PMT. Such a loop (radius $\sim$ 3 cm) may be considered as a mirror with reflection coefficient of about 90%. The fiber ends are collected in one bunch, glued, cut and polished, and connected to a 1" diameter PMT.

To increase light collection 60 μm perforated white reflecting paper is interleaved between lead and scintillator plates, and edges of scintillator plates are aluminized. The complete

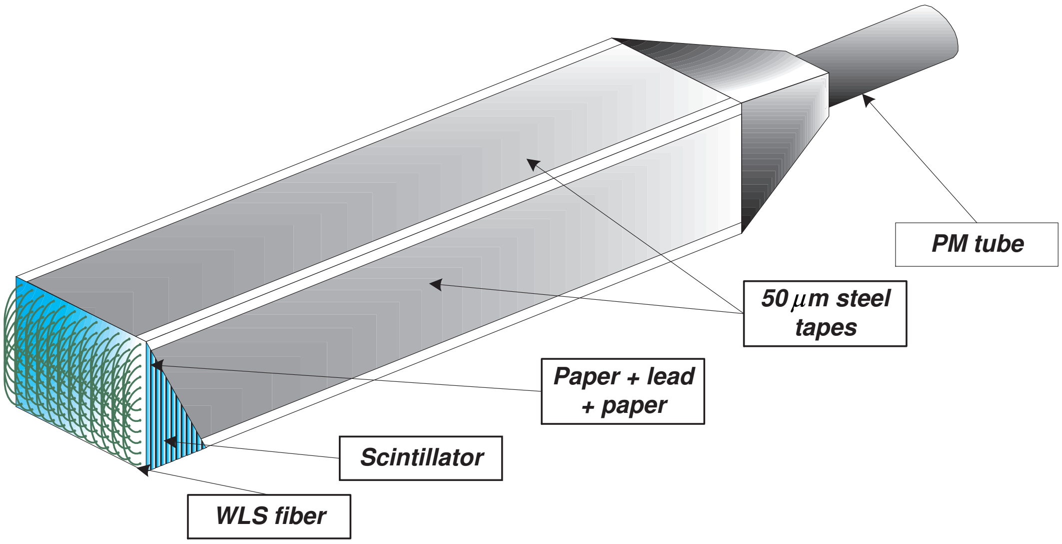

Figure 27: Shashlyk module design

stack of all plates is held in compression by the four 50 μm stainless steel side strips that are pretensioned and welded to both front and back special endcaps.

Parameters of module are summarized in Table 5. The KOPIO calorimeter will contain 2209 such modules.

1.8.2 Experimental study of the prototype module

The characteristics of the modules were studied on B2 test beam at the AGS with 0.5 - 2 GeV/c electrons and pions during the Spring and Fall of 1998. The prototype calorimeter consisted of 3×3 modules. The tests examined the response to tagged electrons of different energies and the uniformity of response as a function of incident position of the beam. Three different photomuliplier tubes (FEU85, FEU115, and EMI - 9903B) and three different WLS fibers (KURARY:Y11(200)M-DC, BICRON: BCF-99-29A-SC and BCF-92-SC) were examined.

The results of resolution measurements (σ_E/E) for various configurations, as well as fits to these data (where σ_E/E is parameterised as $\sqrt{\mathrm{p_1}^2 + \mathrm{p_2}^2/\mathrm{E}}$) are shown in fig. 28. Also shown is a GEANT calculation of resolution in the limit of sampling and geometry alone. One sees from these results that Shashlyk with the Kuraray fiber and EMI tube yield a resolution of $3.8\%/\sqrt{E}$.

GEANT simulations are in good agreement with the data of fig. 28 when sampling, leakage, holes, light attenuation, photostatistics, and noise are included in the calculation. The measurements were not sensitive to uniformity of light collection.

Energy resolution depending on the level of details of Monte-Carlo simulation is shown on Table 6.

Table 5: Properties of Shashlyk module.

Item	***Dimension***
Lateral segmentation	110 mm x 110 mm
Absorber layers	240
Scintillator thickness	Analog NE110, 1.5 mm
Absorber thickness	Pb, 0.35 mm
Reflective material thickness	TYVEK paper, 0.06 mm x 2
Effective X_0	31.5 mm
Effective R_M	54.9 mm
Number of WLS fibers per module	72
Fiber spacing	9.5 mm
Holes diameter in Scintillator/Lead	1.4 mm/1.5 mm
Diameter fiber	1.0 mm (1.2mm)
Fiber bundle diameter	14 mm (17 mm)
Effective density	2.75 g/cm^3
Active depth	473 mm (15.9 X_0)
Total depth (without PMT)	610 mm

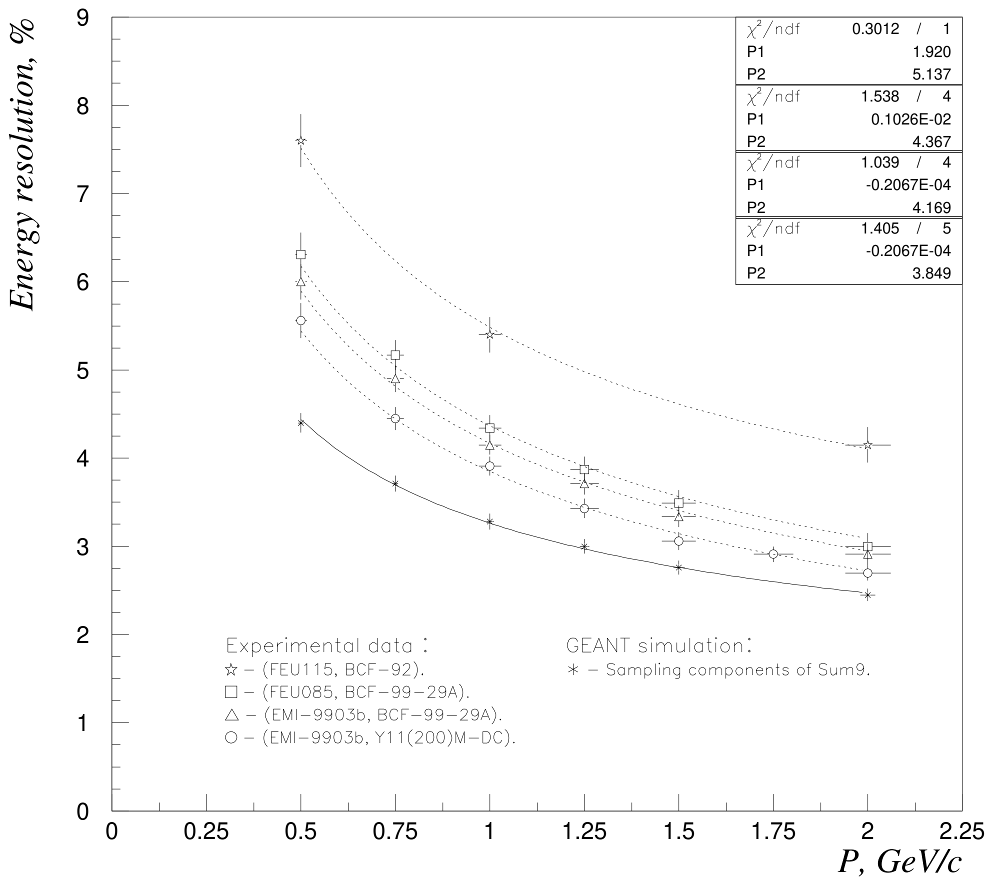

Figure 28: The energy resolution of the nonet of modules versus momentum of the electron beam. The measurements were made for four types of light collection systems (see text). The results of the fit for the different configurations are given in the figure. A GEANT calculation in the limit of sampling and geometry alone is also shown.

Table 6: Energy resolution of uniformly exposed prototype module depending on the level of detail of Monte-Carlo simulation

	$\sigma_E/\sqrt{E}$ (%)
Sampling only	2.69
+ 240 layers	2.84
+ Holes and steel strips	3.04
+ Attenuation in fiber	3.01
+ Photostatistics	3.65
+ 3 × 3 modules	**3.84**
+ Nonuniformity of light collection	4.27

1.8.3 Improving the energy resolution

Sampling constitutes the main contribution to the energy resolution. However, it is less than the combined contribution of other factors, 3.3% (added in quadrature). Among these contributions the most significant are photostatistics, 2.1%, and uniformity of light collection, 1.8%.

The possibilities of improving the sampling contribution are limited. Decreasing the thickness of lead plates or increasing of thickness of scintillator plates increases the effective radiation length of the module, and as a result resolution deteriorates due to longitudinal fluctuations of electromagnetic shower and due to an increased transverse leakage (increased Molière radius). Simultaneously decreasing the thickness of lead and scintillator plates will lower photostatistics. Decreasing lead and/or scintillator plates may also cause technical problems for module production.

Within these limitations we consider 3 possible improved samplings shown in Table 7:

To improve the uniformity of light collection we propose using a chemical modification of a scintillator surface (CMSS) [55] on the edges of the scintillator plates, which produces thin (50-100 μm) white foam layer with a diffuse reflection efficiency of about 93%. This coating also increases total light output (photostatistics). Monte-Carlo distributions of light output as a function of the distance from the center of modules with and without this coating are shown on Fig. 29

In addition to increasing scintillator plate thickness and fiber diameter, light output may be also increased by establishing optical contact between fiber and scintillator. This may be accomplished by gluing fibers within scintillator holes. Direct measurements on a single plate confirmed this concept. Results of calculations for the 3 versions of modules with the above described improvements is presented in Table 7.

One can see that improvements in mechanical and optical construction of modules can yield an energy resolution of about $3.2\%/\sqrt{E}$. There is almost no difference between the expected resolution for versions 1 and 3. Larger longitudinal leakage fluctuations in the case of version 3 can be compensated by a better sampling term. Increasing of the number of modules to capture a larger fraction of visible energy is limited by a greater noise contribution. If fibers are not glued, resolution will be increased by $0.1\%/\sqrt{E}$.

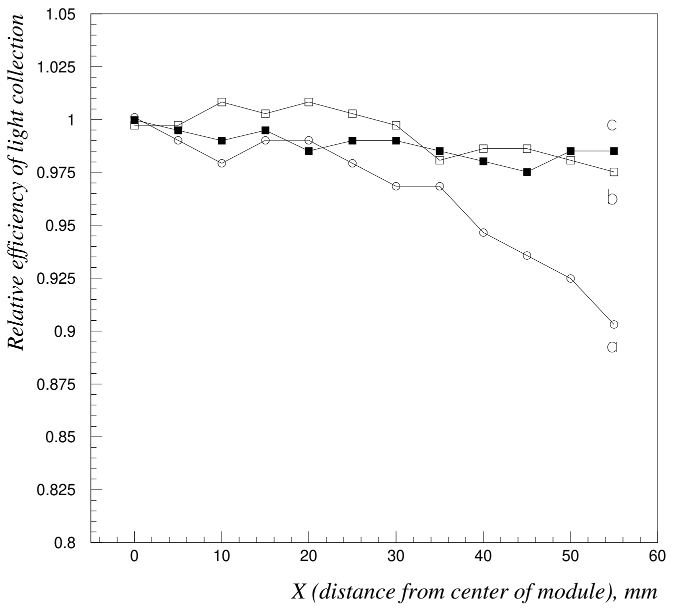

Figure 29: Monte-Carlo dependence of light output on distance from center of module for (a) existing prototype of module, (b) suggested module totally covered by CMSS, and (c)module with CMSS only on edges. Data normalized to 1 at center of plate.

Table 7: Energy resolution ($\sigma_E/\sqrt{E}$) in a module, uniformly exposed by 250 MeV photons, depending on the level of detail of the Monte-Carlo simulation. Statistical accuracy of the calculations is 2%

Module version	1	2	3
Number of layers	400	300	300
Lead thickness (mm)	0.25	0.35	0.25
Scint. thickness (mm)	1.5	2.0	2.0
Fiber diameter (mm)	1.2	1.2	1.2
Sampling only	2.14	2.50	1.91
+ Finite number of layers	2.12	2.54	2.13
+ Holes and steel strips	2.34	2.68	2.31
+ Attenuation in fiber	2.53	2.88	2.57
+ Photostatistics	2.82	3.09	2.75
+ Nonuniformity of light collection	2.87	3.15	2.84
+ 3×3 modules	3.17	3.42	3.23
− gluing of fiber	3.28	3.53	3.16

1.8.4 Time resolution

Detailed time resolution studies of Shashlyk modules were performed by the PHENIX collaboration [51]. The results of those studies show that, for 1 GeV electrons, the time resolution for their modules was 100 psec and the light yield was 1200 photoelectrons. The experimental light yield for the prototype module described above was 3100 photoelectrons at 1 GeV, and the anticipated improvement on this is a factor of 2.2. Since time resolution is inversely proportional to the square root of the light yield, we can anticipate a resolution of ~ 50 ps/$\sqrt{\mathrm{E(GeV)}}$ for the improved modules. We note that the average photon energy for the experiment is about 250 MeV/c, so our time measurements will have a time resolution on the order of 100 ps.

1.8.5 Summary

Modules for a Shashlyk calorimeter with energy resolution about $4\%/\sqrt{E}$ have been constructed and experimentally tested. Monte-Carlo simulation based on this experimental data indicates that this resolution can be improved to about $3.3\%/\sqrt{E}$ with a time resolution better than 60 ps/$\sqrt{E}$. These realizable parameters well meet the design goals of the KOPIO experiment.

1.9 Veto detectors

Suppression of most backgrounds is provided by a hermetic high efficiency photon and charged particle detector system. This system divides itself into two sections: the region around the decay volume and the region downstream of the decay volume including the beam catcher. The preradiator/calorimeter also acts as a veto system, thus the decay region is thoroughly enclosed. Figure 4 shows the layout of the various components of the veto system.

1.9.1 Decay region veto detectors

Around the decay region the basic element of the photon veto system is a Pb scintillator sandwich consisting of 23 7 mm thick, 15 cm wide scintillator plates interspersed with 1 mm of Pb, see fig.30. The length of each element depends on its specific location in the apparatus, with the longest element being 4 m. The scintillators are extruded, with 1 mm grooves placed 10 mm apart running their full length, see fig. 31. Readout is accomplished with wave length shifting (WLS) fibers placed in the grooves and viewed from each end of the element. In most locations four elements are stacked perpendicularly to the photon direction of flight, providing about 18 X_0 of thickness of conversion and detection thickness.

The WLS fiber used is BCF99-29 which has a decay time of about 3.3 ns and an attenuation length of more than 4 m. The fibers are viewed with FEU-115M phototubes at either end. The FEU-115M, produced in Russia, has a photocathode sensitivity extended into the green region, as appropriate for detecting WLS fiber light. Details of construction, testing, and performance of such modules can be found in a KOPIO technical note [57].

From the tests, a single plate of scintillator as described above has a light yield of 17 photoelectrons for minimum ionizing particles. The summed output of phototubes reading out both ends of the fibers shows less than a 10% variation over the length of the scintillator. The light yield corresponds to 12 photoelectrons per MeV of energy loss in the scintillator. This results in about 1300 photoelectrons for minimum ionizing particles passing through the total thickness of a stack, which can be compared with 750 photoelectrons for the photon veto counters in E787. Comparison with E787's results is important since it is the performance of that veto system which is well documented [58], and with which we make our veto efficiency estimates.

The method of stacking the veto modules around the decay volume is depicted in figure 4. The nature of the modules allows their ends to be curved, thus facilitating the construction of the hermetic enclosure. Straight modules span the roof, floor, and upstream parts of the enclosure, while curved modules make up the sides. The modules spanning the 3.5m width of the top of the enclosure are supported by an external truss structure via thin ($\sim 100\mu$m) straps extending down from the external support beams, see fig. 32. For the side walls the modules will be mounted in shelves which support their weight.

Because backward going photons have low energies, the scintillator to lead ratio and the number of WLS fibers per plate will both be increased for the upstream modules.

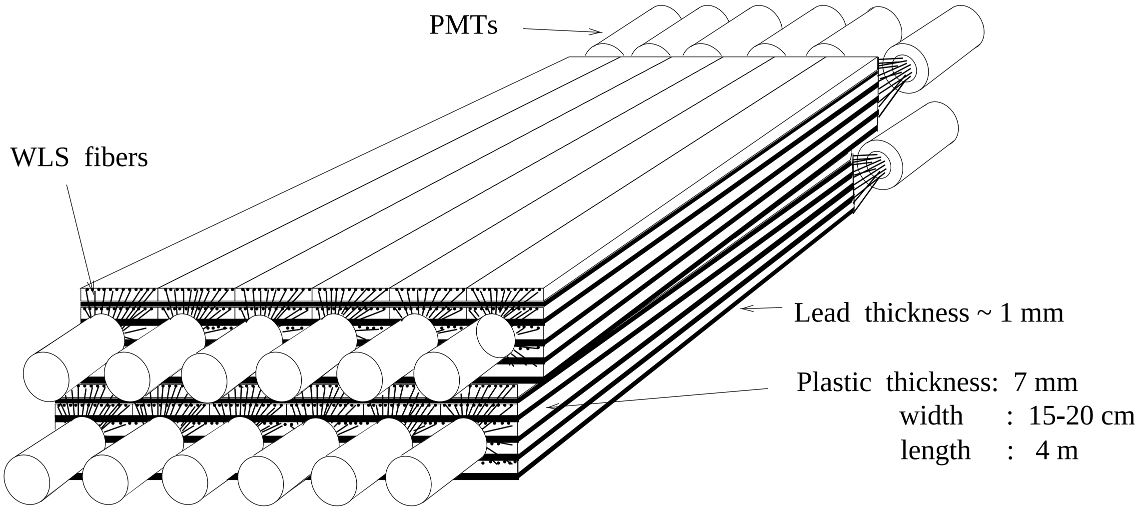

Figure 30: Isometric schematic view of twelve veto elements.

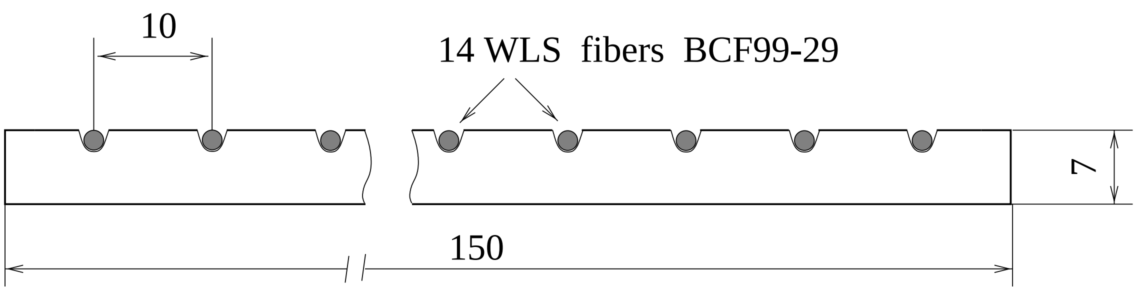

Figure 31: End view of a scintillator plate.

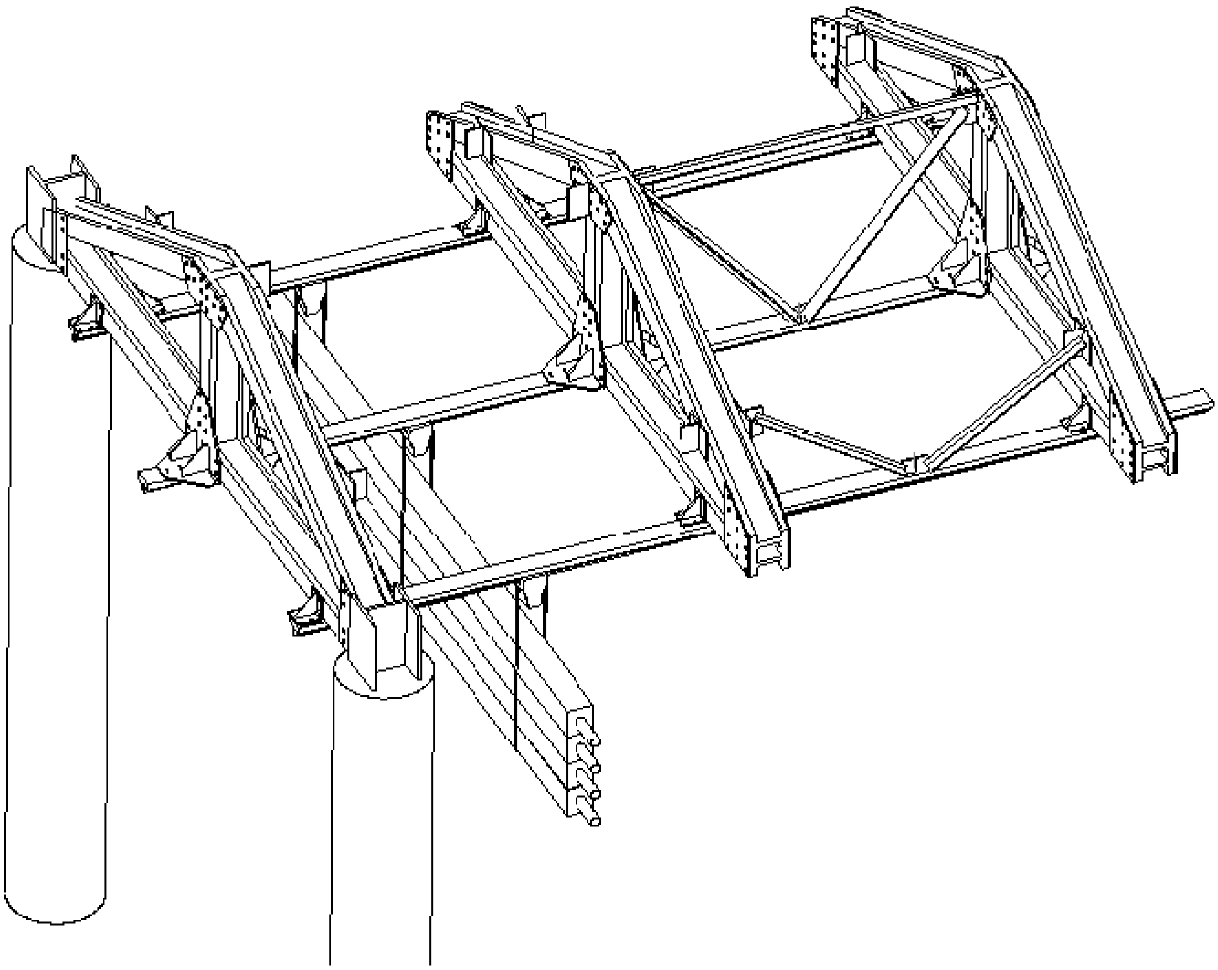

Figure 32: Support structure for the roof veto counters.

1.9.2 Charged particle and downstream veto detectors

Vetoing charged particles is important for suppressing background modes such as $\pi^+\pi^-\pi^0$ and K_{e3}, and for reducing the trigger rate. The most dangerous mode is the former, and after kinematic suppression must be suppressed by a factor of 10^9 to yield a $\pi^+\pi^-\pi^0/\pi^0\nu\bar{\nu}$ ratio of less than 0.1.

To achieve the required high veto efficiency we will have two levels of detection for charged particles. In the decay region, scintillator inside the the vacuum vessel forms the first line of defense. The vessel will be lined with 7 mm of scintillator which will be read out with embedded WLS fibers running longitudinally. For readout, the fibers will run upstream along the walls of the upstream beam pipe of the vacuum vessel, and exit the vacuum through the pumping station box upstream of the detector. The second detection of charged particles in the decay region will be with the photon veto system where the first plate in each element is a scintillator plate. This method has the added advantage of also detecting photons which might result from charge exchange of π^-s coming from K^0 decays.

In the downstream beam hole direction beyond the calorimeter, charged particles will be swept out of the neutral beam with the bending magnet, seen in fig. 4, and into veto scintillators. By and large these counters will also be backed by photon veto counters.

Photon vetoing downstream of the calorimeter will be accomplished with counters whose construction is essentially as described above. Because of the large angles of photon trajectories in the horizontal plane, the downstream beam pipe will be lined in its median plane with similar detectors.

1.9.3 Beam catcher

The requirement of high veto efficiency is true for all directions of flight of the extra photons, including the region occupied by the beam. This presents a challenge since the beam region contains as many as 10^{11} neutrons per 100 TP machine pulse, as well as 1.7×10^8 K_L^0 per pulse. Fortunately, however, only a few times 10^{-3} of the undesirable events send their photon into the beam region 15 m downstream from the decay region, and most of those photons have energies above 100 MeV. Thus, the detector that must operate in the beam region, termed the catcher, need only have a detection efficiency of about 99% to achieve the required background suppression.

Catcher Designs

Pb-Lucite Sandwich Catcher

At present we are considering two catcher designs. One is the detector based on Pb-Lucite sandwiches viewed on edge by means of total internally reflected Cerenkov light. It is blind to low energy protons and charged pions due to Cerenkov threshold or total reflection threshold, and thus is expected to be blind to neutrons.

Based on this design, a prototype counter has been constructed and tested in three kinds of beams, 100–400 MeV photons, 200–400 MeV neutrons, and 200–1200 MeV protons. A module is composed of 8 layers of 2mm-thick lead sheets and 9 layers of 10mm-thick Lucite sheets stacked alternately, viewed by two 5-inch photomultipliers from both (up and down) ends of Lucite sheets. Four identical modules are placed in series along the beam direction, and the total thickness is equivalent to 12 X_0.

In a photon beam at INS (KEK-Tanashi), its inefficiency has been measured with various photon energies and threshold values, as shown in Fig. 33 We have found that the distribution

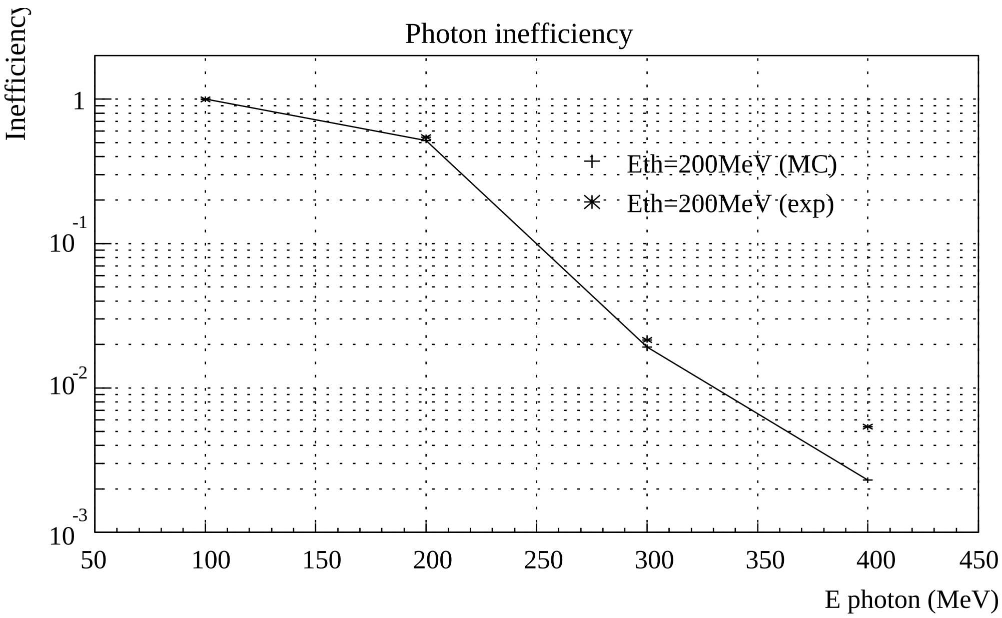

Figure 33: Photon inefficiencies as a function of incident energy with energy threshold of 200 MeV.

is well reproduced by MC simulation so far as 0.5% level.

As for the neutron efficiency, we have performed two measurements. In a low energy region around π^0 production threshold, we have measured the neutron efficiency directly using the neutron TOF beam line at RCNP (Osaka). In a high energy region where a neutron might come within the event time window, i.e. above 1500 MeV/c ($E_{n,kin}$=830 MeV), we have measured the efficiency for protons (instead of neutrons) and compared it with a MC simulation to verify the validity of the nuclear interaction part in the simulation. Even though detailed analysis of these measurements is still proceeding, the simulation says that if we set the energy threshold at 200 MeV, we can obtain 98% photon efficiency above 300 MeV, while the neutron efficiency can be kept as low as 1% level at 1500 MeV/c, as shown in Fig. 34

Studies are continuing to improve the low energy detection efficiency and to reduce the neutron efficiency by other cuts. This design and the results of the tests are presented in a KOPIO technical note [56].

Aerogel Distributed Catcher

The other design [59] takes advantage of the low energy of the beam to produce inefficiency in neutron and beam kaon detection without sacrificing photon detection efficiency. This is possible since the photons we wish to veto are coming directly down the beam line, while the particles to which we wish to be blind arise from low energy π^0 decays and knock-

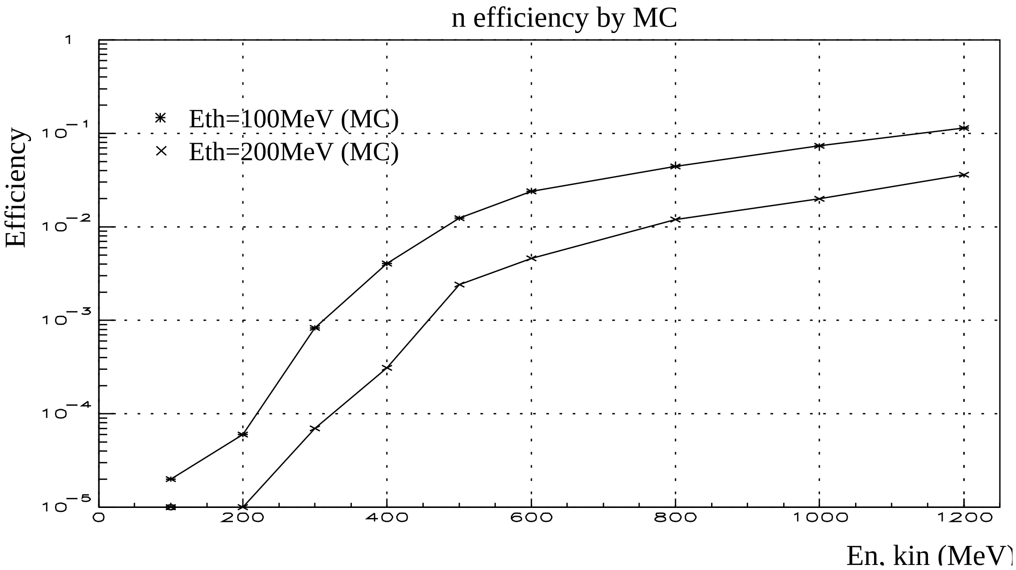

Figure 34: Simulated neutron efficiencies as a function of incident energy, with thresholds of 100 MeV and 200 MeV.

on proton recoils which are produced over a wide range of angles with respect to the beam. The basic concept is to convert the photons, detect the resulting electron/positrons through Cerenkov radiation, and veto those which are traveling in the beam direction.

The catcher consists of 600 modules of the design shown in fig. 35. The modules are arrayed in 25 rows (transverse to the beam) of 24 modules, with the rows separated by 25 cm. The radiators are 5 cm thick aerogel with index of refraction about 1.03. Such a radiator raises the threshold velocity of charged particles high enough so that knock-on protons produced by beam neutrons make no light. That aerogel can be reliably used in this application has been demonstrated by the HERMES collaboration [60]. The HERMES group notes that new production techniques now yield very transparent hydrophobic aerogel with indices of refraction in the range 1.01 to 1.1. We choose 1.03 since the HERMES group performed their beam tests with this material and were able to obtain more than 20 photoelectrons from a 5 cm thick radiator.

Each module segment contains 1/3 X_0 of material. Along the beam there are 25 segments for a total of 8.3 X_0 over a distance of 6.3 m. The modules in a row are staggered laterally by half a module width from those in the following and preceding rows. Vetoing will occur if there is coincidence between the module in which the photon converts and either of the modules directly in back of it in the next row.

The unscattered Cerenkov light emerging from the downstream end of each aerogel slab will be focussed and reflected by a section of spherical mirror with its axis tilted vertically at 45° to the horizontal. Such light can be focussed onto a 5 cm PMT mounted vertically over, and pointed at the mirror. That a sufficient amount of such unscattered light can be captured has been demonstrated in the HERMES R&D program.

We have performed a GEANT Monte Carlo calculation which simulates three types

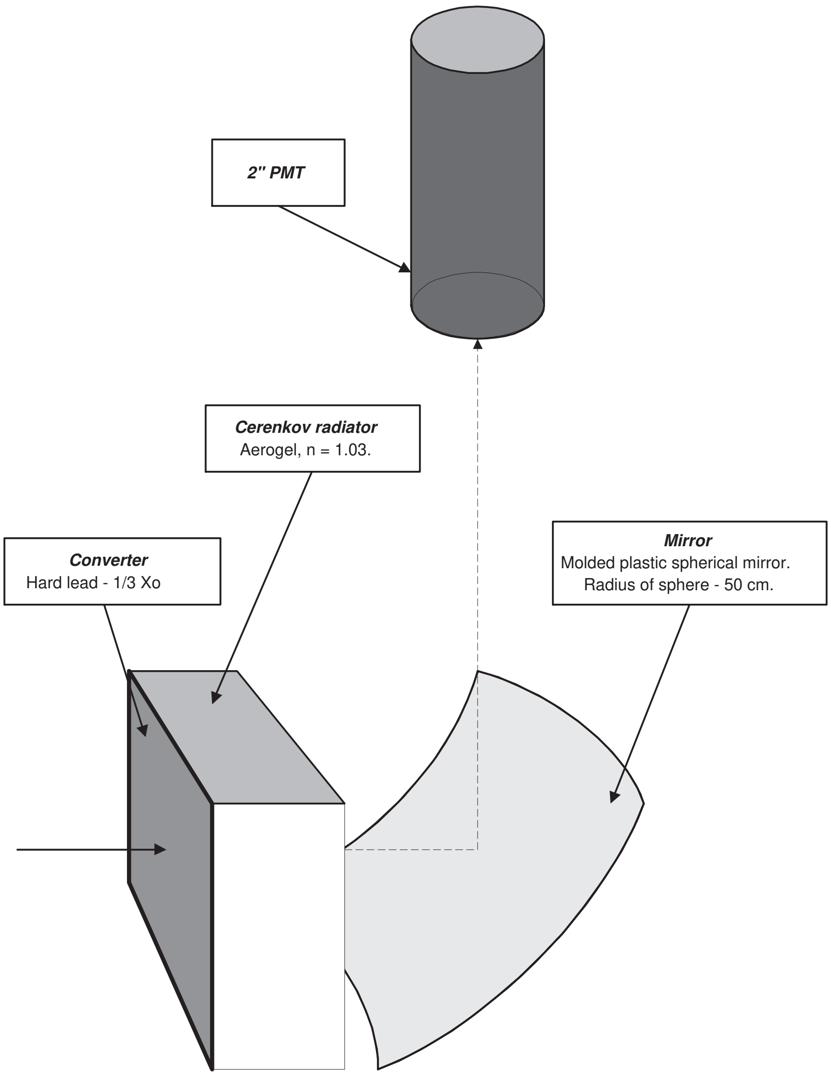

Figure 35: A catcher module.

Table 8: Efficiency of the catcher for various incident particles.

Mode	Momentum (MeV/c)	Efficiency (%)
Decay photons	100.	89.
	200.	95.
	500.	98.5
Beam neutrons	1500.	0.34
	3000.	4.
Beam K_L^0	750.	3.4

of events: photons coming from the beam region of the decay volume; neutrons in the beam; and K_L^0s in the beam. The momenta of the kaons were chosen from a Gaussian distribution centered on 750 MeV/c with a standard deviation of 250 MeV/c. Table 8 shows the efficiencies for detecting these types of particles, where the efficiency is for detection of light in two longitudinally contiguous segments.

From our Monte Carlo calculations $K_L^0 \to \pi^0\pi^0$ events with a photon in the catcher will result in about a 20% addition to the background, and an accidental veto probability due to neutrons of about 10%.

One must also consider the blindness probability, *i.e.* the probability of having any member of a set of counters destined to veto an event being blinded by another hit within, say, 10 ns of the event. Due to the high granularity of the catcher this is reduced to less than a percent for hadronic interactions. Another source of blindness, however, is the prompt photons associated with the beam. These show up at the catcher 4-7 ns before those we wish to veto, thus they will not cause accidental vetos. But they will illuminate the catcher and possibly cause blindness. We calculate the probability of this occurring to be less than 8×10^{-3}. Improving the pulse pair resolution of the detectors to better than 4 ns can significantly reduce this probability, and we are undertaking an R&D program to this end. We expect to instrument each catcher phototube with a transient digitizer operating at 0.5-1.0 GHz.

1.10 Trigger

The basic idea of the trigger is quite simple: two and only two photons appearing in the forward detector and no other particles appearing anywhere else in the veto system.

1.10.1 Trigger scheme

There will be about 4.2×10^7 kaon decays per 3-s machine pulse in the detector volume, corresponding to a decay rate of $\sim$ 14 MHz. With a micro pulse frequency of 25 MHz, the probabilities of zero, one and two or more K_L^0 decays within a micro pulse are about 60%, 30% and 10%, respectively. Because the decay volume is 4 m long, the time between photon conversions in the forward detector and particles interacting in the veto counters ranges from zero to 12 ns. Since the RMS spread in kaon decay times within a micro pulse is comparable, about 15 ns, we cannot reliably veto one K_L^0 decay and accept another within the same micro pulse. We thus choose at the outset to trigger only on those micro pulses with single decay in which exactly two photons are present in the forward detector, and no veto counters fire. Although this costs about 40% of the possible K decays, it greatly simplifies the trigger scheme and allows a reasonable trigger rate.

The Level-0 trigger requires the presence of activity in the pre-radiator, no energy deposited in the barrel region (with a threshold of 5–10 MeV), no charged particles observed, and minimum and maximum numbers of hits in the pre-radiator scintillators and calorimeter. Another fast effective logic scheme will require cuts on the average hit positions in the x and y projections (a very crude form of transverse momentum balance). Two-dimensional cluster counting in the $x-y$, $x-z$ and $y-z$ planes will also be applied at this level.

In order to recognize two and only two conversions in the forward detector system we group the scintillators in the preradiator to form three dimensional "cells". Each plane of the preradiator will be divided into quadrants, and the fibers of each quadrant grouped into 16 cm units. The orientations of the fibers in contiguous planes along the beam (z) direction are horizontal (x), vertical (y), and at 45° (v). This pattern is repeated along the length of the preradiator. Because each scintillator yields a relatively small number of photoelectrons (about 7) and to reduce the influence of phototube noise in the photon energy measurement, we group four planes of fiber units together, *i.e.*, four x's, four y's and four v's. One cell has a volume roughly 18 cm in z and 16 cm in x and y. (The redundant v plane is present to remove (off-line) the combinatorics in $x-y$ that would occur with two conversions in the same quadrant at the same depth. This information is not used at Level-0.) The numbers of clusters of cells in the $x-y$, $x-z$ and $y-z$ planes, after projecting hits onto each plane, are obtained using fast logic based on gate array chips or memory lookup units. There are five cell-planes in the z direction and the calorimeter is treated as the sixth column element in the $x-z$ or $y-z$ matrix. As presently conceived this approach is about 97% efficient at recognizing π^0s from $\pi^0\nu\bar{\nu}$ events. Roughly 5% of $\pi^0\pi^0$ events fail to be rejected due to overlapping photons.

Most veto counters will be viewed from both ends and mean-timed. They will be appropriately delayed to compensate for hit positions along the beam, *i.e.*, upstream, in the barrel, or at points along the downstream regions. With the time of veto counter hits so adjusted, the number within a given micro pulse can be determined. This process will be "pipelined", so it imposes no dead time.

Once this level of trigger (L0) is satisfied, the time and analog information from all counters and from the appropriate channels of the preradiator will be digitized and read out. The delay of the trigger is constrained to be on the order of 150-200 ns since that is the evolution time for the analog information from the strips in the preradiator chambers.

1.10.2 L0 Trigger rates

To determine the rates of the Level-0 trigger output, Monte Carlo simulations were done. Events were generated for various decay modes, and the Level-0 trigger logic was applied. A photon veto threshold for the barrel region was set at 5 MeV (visible energy). The charged particle detection inefficiency was conservatively assumed to be 1 %. Table 9 summarizes the number of Level-0 triggers per machine cycle for the various modes for which significant numbers of triggers are expected.

Table 9: Number of L0 triggers per machine cycle for various decay modes.

Mode	B.R.	Triggers
$\pi^{\pm}(\mu+e)^{\mp}\nu$	0.66	200
$\pi^0\pi^0\pi^0$	0.21	600
$\pi^+\pi^-\pi^0$	0.13	20
$\pi^0\pi^0$	10^{-3}	100
$\gamma\gamma$	6×10^{-4}	900
Accidentals		2000
Total		3820

1.10.3 Higher level trigger rates

Although the present Level-0 estimate reduces the data flow to a manageable level, we are considering several schemes of higher level triggers based on the fast digitized information available on energy and time to further reduce the data volume before events are fully read out. These include requirements of unbalanced sums of observed energies and transverse momenta, and cuts based on refined timing information and tracking. As an example consider $K_L \to \gamma\gamma$ events. Given that the full rest mass energy of the K_L^0 goes into the photon energies in $K_L \to \gamma\gamma$ decays while only a fraction goes into those of $K_L \to \pi^0\nu\bar{\nu}$ decays, the total laboratory energy of the photons in the former is usually greater than that in the latter. That this is true can be seen in fig. 36. Forming a correctly compensated analog sum of the total energy seen in the forward detector allows one to cut high energy (2γ) events while having a small impact on the desired $\pi^0\nu\bar{\nu}$ events. The MC simulation indicates an additional suppression factor of 5. Similar suppression factors are obtained for other "energy conserving" decay modes such as $K_L^0 \to \pi^0\pi^0\pi^0$. This logic scheme can be further improved by combining it with the time-of-flight information, which compensates for the variation in the incident K_L energy.

Another example is the reduction of accidental events by employing tighter timing, and hit patterns and energies of struck cells available from digitized information.

The Level-1 scheme with a decision time of $\sim 10\mu$s is based on a combination of highly multiplexed fast ADC's for triggering, memory lookup units for providing energy calibration, and arithmetic units for energy summing or energy-weighted hit-position determination. The read-out process will be aborted (with the additional deadtime of $\sim 1\mu$s) if it fails the logic. The DAQ system reads out the data from the detectors, most notably the preradiator chambers, at a rate of 10^3 events per ~ 3 second machine spill. This will require one level of buffering in order to keep the dead time below a few percent. As described in the DAQ section, such a system will be straightforward to implement using present technology.

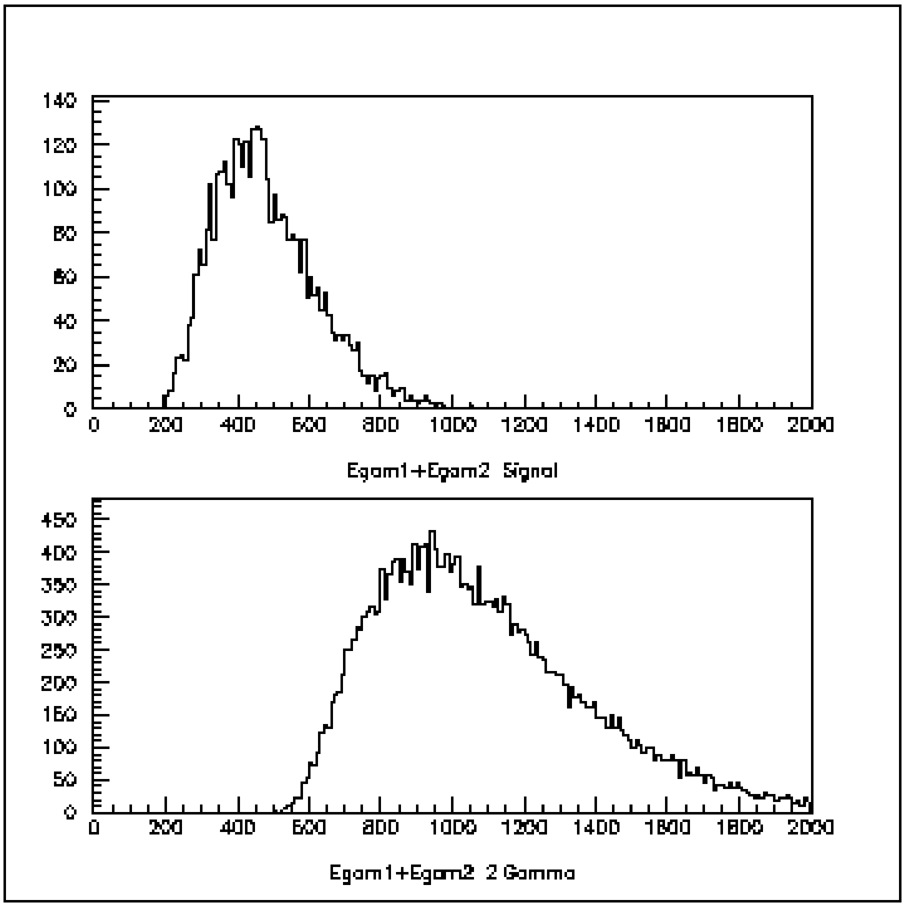

Figure 36: Total 2 photon laboratory energy of $\pi^0\nu\bar{\nu}$ signal events (top), and of 2γ events (bottom).

1.11 Data Acquisition

After the hardware trigger Level 1, the data acquisition system receives the following information:

- analog signals from phototubes (4000 ch) are fed into either switched capacitor arrays SCA, transient digitizers, or ADC/TDCs readout into buffer modules located in a VME-P crate. ADCs in other formats will be read via a custom interface into similar buffer modules. It is assumed that the density of modules achieved will be 256 channels per crate for a total of sixteen crates; and,
- digitized data from chambers that gets stored into large memories located in a VME-P crate. Each VME-P crate has enough storage to keep events from one given spill. In the inter-spill, the data is moved over Fast or Gigabit Ethernet through a network switch. A 16 processor farm receives the data for Level 3 processing and data reduction. Commodity CPU's without monitors will be used to keep costs down. A large CPU host collects the events from the farm and data is written to disks and logged to tape in the background

Table 10: A summary of data rates.

Modes	# of γ/ev	Data /ev / K Bytes	Trig./spill After L2	Data/spill K Bytes
$\pi^{\pm}(\mu+e)^{\mp}\nu$	2	2.7	200	540
$\pi^0\pi^0\pi^0$	6	7.1	120	852
$\pi^+\pi^-\pi^0$	4	2.7	20	54
$\pi^0\pi^0$	4	4.9	20	98
$\gamma\gamma$	2	2.7	180	486
Accidentals		2.7	1000	2700
All				4730

Data rates have been estimated assuming the following: each γ will generate 8 phototube pulses and 35 layers of chamber hits in the preradiator and 9 phototube pulses in the calorimeters. Each phototube pulse is sampled (8 bit samples) at 500 MHz for 50 ns for an average of 32 Bytes/pulse[4] and each layer of chamber hits is digitized in 16 Bytes. This adds up to a total of 1.1 KB/γ. Extra overhead from header data and randoms in the veto counters is estimated at 0.5 KB/ev

Although the signature of the trigger will be the presence of two gammas, some of the backgrounds really contain more gammas. These events will trigger when pairs of gammas are located in the same area. Data produced by such a pair will have more data than a clean gamma and thus we have calculated the rates based on the number of gammas in

[4]Data rates are estimated assuming all pmt pulses are transient digitized at 500 MHz.

each trigger. Assuming trigger rates as described in the previous section and the results of preliminary Monte Carlo calculations, we estimate data rates shown in Table 10.

The estimated total data rate of < 5 MB/spill can be handled easily by two DLT7000's. Monitoring and calibration triggers are accounted for by raising this rate to 7 MB/spill. Such a data acquisition system collects data at a rate less than that presently handled in the E787 experiment.

1.12 Simulations

We simulated the performance of the KOPIO detector in order to estimate the acceptance for $K_L^0 \to \pi^0 \nu\bar{\nu}$ and the suppression of backgrounds. Since the KOPIO neutral beam is planar as indicated in Fig. 5 (see Overview Section), the decay vertex is obtained from the preradiator measurement of each photon conversion position and direction extrapolated to the beam plane. The position and direction of the other photon, the time difference between the two photons (i.e. the path length difference between the photons and the vertex), and the π^0 mass provides up to four additional constraints. These extra constraints are effective in removing non-Gaussian tails, particularly in the preradiator angular measurements. The K_L energy is measured by time-of-flight and its direction is obtained by connecting the production target position and the decay vertex.

Figure 26 [in Sec 1.7] shows the simulated preradiator angular resolution distributions obtained for several photon energies. The angular resolution function is parameterized by two Gaussians, one of which represents the core and the other accounts for the tail due to large angle scattering of the electron or positron. Table 1 lists the resolution parameters used in the simulations including effects of the energy dependence of the angular resolution. Typically 200k Monte Carlo events were generated for each mode used to study the acceptance and background rejection. Up to 100M events were generated to examine the rarest cases such as photons missing in the beam holes.

The analysis of the Monte Carlo data was performed in 2 steps. First a 3C constrained least square kinematic fit was performed without using the π^0 mass constraint. This fit provided the two-photon invariant mass $m_{\gamma\gamma}$. Fig 37(a) shows the $\gamma\gamma$ mass distribution for signal events with m_π^0 resolution (RMS) approximately 10 MeV. In the second step, a full

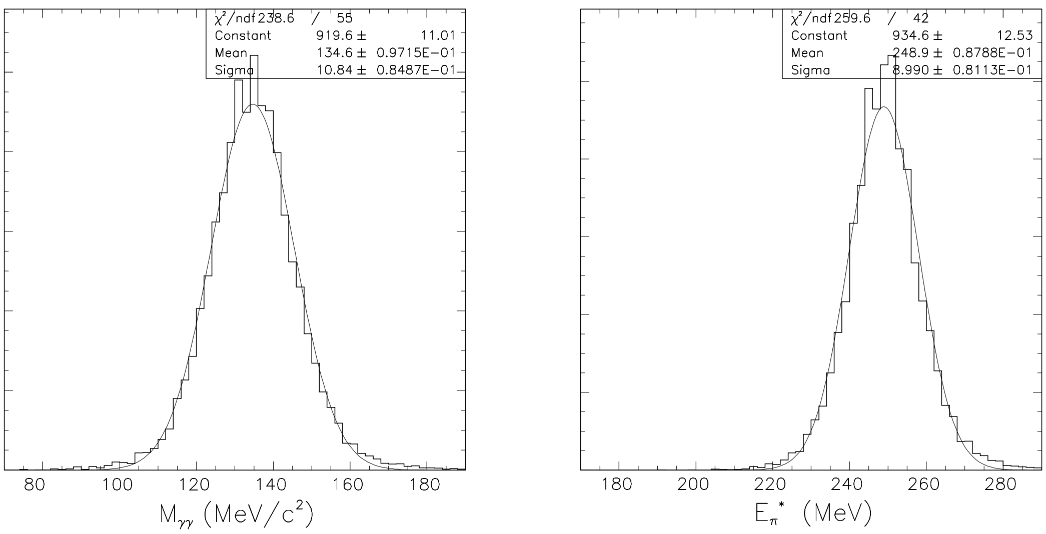

Figure 37: Reconstructed $\gamma\gamma$ mass and E_π^* from the detector simulation for the $K_{\pi 2}^0$even paring events.

4C constrained fit was performed including the π^0 mass constraint to achieve the best vertex and energy resolutions. Fig 37(b) shows the reconstructed E^*_π distribution for the $K^0_{\pi 2}$ even paring events, and Fig 38 shows the reconstructed K_L decay vertex resolution distributions with $\sigma_x = 7$ cm, $\sigma_y = 1.3$ cm, and $\sigma_z = 14.6$ cm.

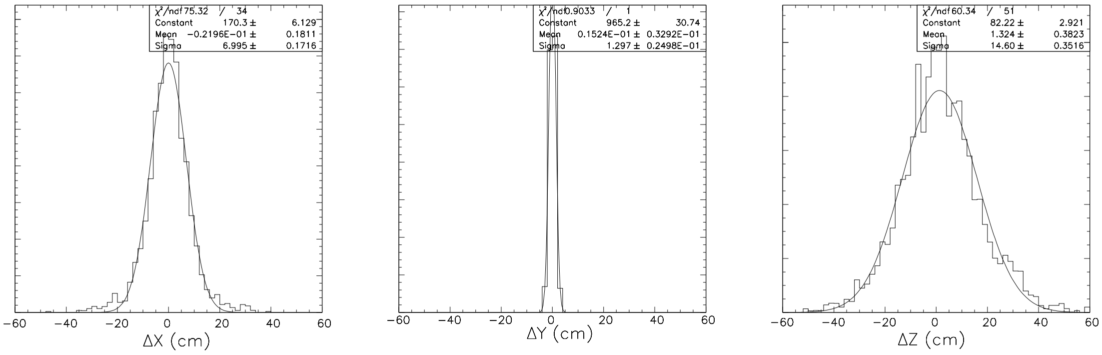

Figure 38: Reconstructed K_L decay vertex resolutions.

1.13 Background Rejection

1.13.1 Photon veto

High detection efficiencies for additional photons and charged particles are the primary defenses against backgrounds in the $K_L^0 \to \pi^0 \nu\bar{\nu}$ measurement. However, there are barriers to achieving unlimited efficiency such as photo-nuclear interactions in which the photon energy is transferred entirely to neutrons to which we are mostly blind. In the following we deal with the limits of photon detection efficiency, the KOPIO kinematic method of suppressing the most dangerous background with extra photons due to $K_{\pi 2}^0$, and the problems of photons escaping detection in beam holes and within the showers of other photons.

Charged particle detection efficiencies are also relevant to the suppression of backgrounds like K_{e3} and $K_L^0 \to \pi^+\pi^-\pi^0$. The detection efficiency for pions and electrons will be discussed in the context of the background estimates for these modes presented in the next section.

Photon Detection Efficiency

E787 has achieved a π^0 detection inefficiency of $< 10^{-6}$ for 200 MeV/c π^0 decays which yield photons between 20 and 225 MeV. The detector employs lead/scintillator calorimetry similar to that proposed for KOPIO. The central E787 photon detector consisted of about 1 radiation length (X_0) of plastic scintillator (range stack) followed by multiple layers of 1 mm thick lead and 5 mm thick scintillator (barrel veto) for a total of about 15 X_0. The greatest inefficiency, 1%, occurs for photon energies ≤ 20 MeV due to sampling fluctuations. The inefficiency for higher energy photons was 10^{-4} and appeared to be limited by sampling fluctuations, shower escape and photo-nuclear reactions which may be contributing at comparable levels.

Progress on the limits of photon detection has been made in a beam test at INS (Japan)[61] where the efficiency for detection of photon-induced events with photo-nuclear interactions (i.e. those in which soft neutrons were also detected) was made in the energy range from 185 MeV to 1 GeV. Single photon inefficiencies as low as 10^{-6} for 1 GeV photons could be inferred from these measurements under the assumption that no events occur in which high energy neutrons carry off all the missing energy. If this assumption were valid, the efficiencies quoted below for higher energy photons would be considerably improved with the consequences of much reduced backgrounds and higher acceptance for KOPIO. However, in order to determine the true photon veto inefficiency at higher energies than covered by E787, construction of a full 4π spectrometer like that needed for a $K \to \pi\nu\bar{\nu}$ experiment will be required. Thus, due to the uncertainties in the validity of the inefficiencies inferred in Ref. [61], we will use only the levels already demonstrated by E787 in our estimates below. Uncertainties in the level of photon detection efficiency achievable are actually largest for the region $E_\gamma \leq 20$ MeV which is preferentially populated by higher energy π^0 decays due to Lorenz boosting. For these photons, the detection efficiency is minimal at best and additional measures must be taken.

Suppression of photons in $K_{\pi 2}^0$ decays

In order to fully suppress $K_{\pi 2}^0$ backgrounds, a π^0 detection inefficiency of 10^{-8} is required. This is a realistic goal in KOPIO where both "missing" photons from $K_{\pi 2}^0$ decay can be required to be in the higher energy range of the E787 measurements because we have kinematic handles available to suppress those configurations with low energy missing photons.

Some improvements in the photon detection inefficiency for lower energy photons may also be possible (until the photo-nuclear limit is reached) by using a finer sampling calorimeter, especially at the front of the barrel veto. The photon detection efficiency for higher energy photons may also be improved by a small factor by implementing more radiation lengths to block remaining shower escape. In the KOPIO experiment, we will increase the average thickness to 18 X_0. Figure 39 shows the photon detection inefficiency assumed in KOPIO background estimates.

Due to the requirement of a single K_L decay per micro-bunch in the KOPIO decay volume, accidental losses associated with photon vetoing are expected to be small.[5]

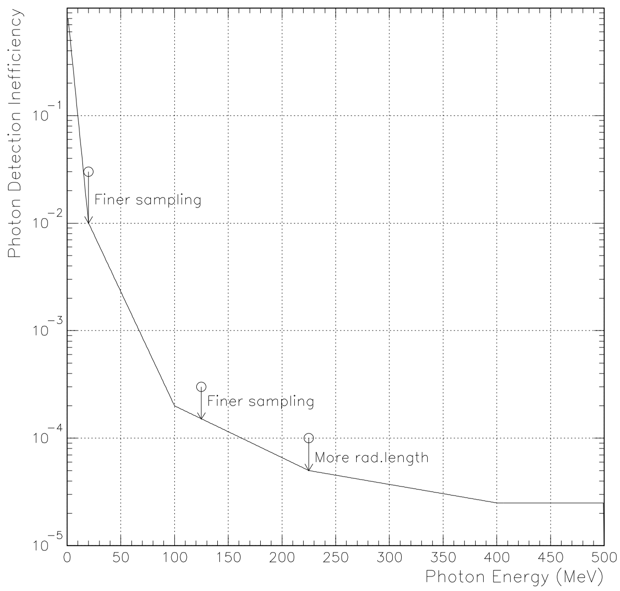

Figure 39: Photon detection inefficiency used in this proposal(solid line). The open circles are the E787 results.

Photon loss in beam holes and within overlapping showers.

100 million events were generated to study the effect of the beam holes. Backgrounds due to photons escaping towards the upstream beam hole were found to be negligible. However, the photons exiting towards the downstream beam hole were found to cause significant backgrounds if not dealt with. The primary defense against this effect is the system of downstream photon detectors, in particular, the catcher described above. Figure 40 shows the energy distribution of $K^0_{\pi 2}$ photons hitting the catcher. The $K^0_{\pi 2}$ background is dominated by the odd paring case with energies above 300 MeV. Having a detector which is 99% efficient for photon energies above 300 MeV is sufficient to bring events exiting through the beam

[5]The single decay per micro-bunch provides a quieter environment than found in E787 where the photon veto accidental losses were in the neighborhood of 20%.

hole under control. At a 300 MeV threshold, we expect accidental losses due to the catcher to be < 10%.

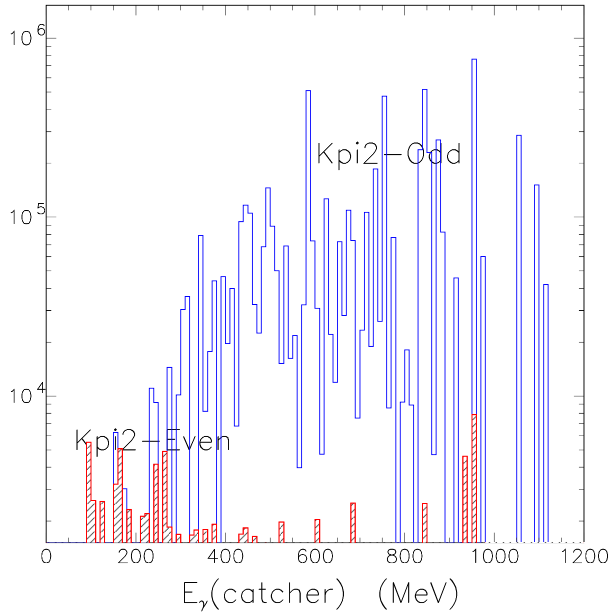

Figure 40: Energy distribution of photons in the beam hole for $K^0_{\pi 2}$ even (hatched) and $K^0_{\pi 2}$odd type events. Absolute normalization of vertical scale is arbitrary.

Although the detection of decay photons traveling out the beam hole seems feasible with the present catcher design, the KOPIO experiment could even proceed without such a detector. As indicated above, we use kinematics to reconstruct the direction and energy of missing $K^0_{\pi 2}$ photons in order to eliminate potential background events. Figure 41 shows the reconstructed position of the $K^0_{\pi 2}$ photons exiting the beam hole obtained from the two photons detected in the preradiator (dots) for the odd pairing case. The $K^0_L \to \pi^0 \nu \bar{\nu}$ signal event distribution, when a $K^0_{\pi 2}$ hypothesis is assumed, is also shown (boxes). At a cost of 20% (33%) of the acceptance, an additional factor of 25 (50) rejection could be provided to suppress these events. The backgrounds associated with lost photons in the beam hole are then below the nominal $K^0_{\pi 2}$ background due to the detection inefficiencies discussed above[6].

Photons can also hide in the showers of other detected photons but we expect that the consequent inefficiency will be smaller than the effects described above. These overlapping photons occur a few per cent of the time in $K^0_{\pi 2}$ events for distances between the two photons at the calorimeter less than 50 cm (about 6 Moliere radii). For separation distances ≤ 20 cm, the probability is < 1% for $K^0_{\pi 2}$ decays. When the distance between two photons is between 20 and 50 cm, we identify the overlapping photons by comparing the shower center of gravity in the calorimeter (position resolution $\sigma \sim 3$ cm) to the expected position from the preradiator. With an estimated inefficiency of 10^{-3} for the center of gravity method

[6]However, the signal to noise ratio (S/N) would be worsened by about 25% if the catcher information were not used.

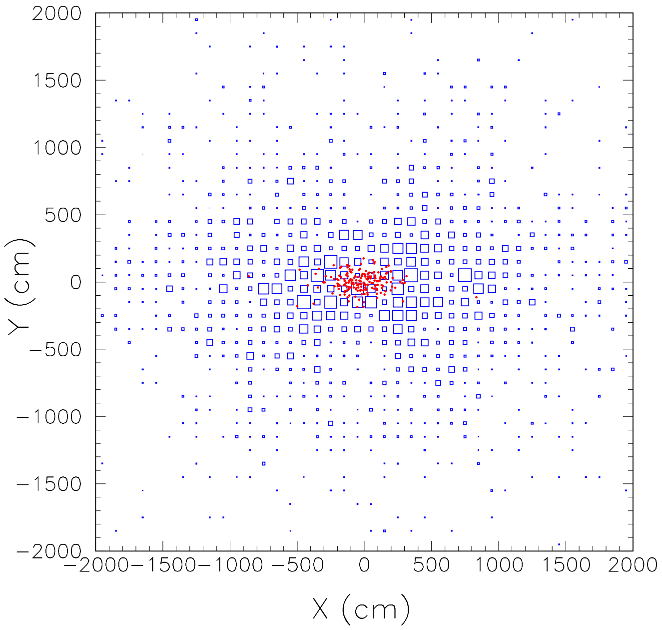

Figure 41: The reconstructed x-y distribution at the catcher position for $K_{\pi 2}$ photons which exit through the beam hole (dots), and for signal events (boxes) interpreted as $K_{\pi 2}$ decays.

and including the probability of the conversion of the extra photon in the preradiator, the inefficiency due to overlapping photons is 10^{-5}. When the separation is less than 20 cm and the overlapping photons merge, the invariant mass of the photons becomes much larger than the π^0 mass and the missing energy and mass are small. The inefficiency of this invariant mass cut is limited by the photonuclear reaction probability (a few times 10^{-3}) of the overlapped photon. Again, taking into account the photon non-conversion probability, the photon detection inefficiency due to overlap in the region of separation < 20 cm is also estimated to be 10^{-5}. We have also found that the loss of acceptance due to cuts aimed at eliminating overlapping photons is only a few percent.

1.13.2 Background Estimates

Methodology

The energy and direction measurements of photons by the KOPIO preradiator/calorimeter arrangement along with momentum tagging of the K_L by time-of-flight provide powerful kinematic constraints for suppressing backgrounds. Among the most effective constraints are the mass of the two photons ($m_{\gamma\gamma}$), and the center of mass energy of the π^0 ($E^*_{\pi^0}$). Vertex restrictions from photon tracking help in rejecting accidentals and particles produced near the surface of the detector by the beam halo. The tight vertical collimation of the beam reduces the beam halo and provides an extra vertex constraint. In the horizontal direction, we apply tighter cuts on the photon reconstruction algorithms to suppress backgrounds. In addition, we construct constraints to avoid backgrounds coming from earlier timing micro-bunches and require that there was only one K^0_L decay in the micro-bunch of interest for

$K_L^0 \to \pi^0\nu\bar{\nu}$ candidates. The 4π coverage of the photon veto ($\overline{\gamma}$) and charged particle veto ($\overline{charge}$) are effective in suppressing other K_L decays. The entire decay volume is evacuated to suppress production of particles in the decay region. Since the KOPIO technique provides complete information on each decay mode, we expect to be able to use data to accurately measure the levels of backgrounds.

In addition to $K_{\pi 2}^0$ decays, potential sources of background include neutron production of π^0's in the fiducial region vacuum, other K_L decays like $K_{\pi 3}$, K_{e3} and $K_L \to \gamma\gamma$ and $\Lambda \to n\pi^0$ decays. Suppression of most backgrounds is accomplished by the high efficiency hermetic photon detector along with kinematic constraints. In the following, we discuss the nominal background levels anticipated for each of the potential sources for the entire proposed exposure of 10^{14} protons on target.

$\underline{K_L \to \pi^0\pi^0}$

The dominant background $K_{\pi 2}^0$ has a branching ratio of 9×10^{-4}. In the $K_{\pi 2}^0$ background studies, each Monte Carlo event was weighted with an energy dependent veto efficiency and a photon direction reconstruction efficiency in order to study the rejection and acceptance. The kinematic information was primarily used to suppress $K_{\pi 2}^0$ background through the use of a cut on the pion c.m. energy $E_{\pi^0}^*$ for the even paring background events, and a cut on the reconstructed pion mass $m_{\gamma\gamma}$ for odd paring background events. The full kinematic information was found to allow a range of $K_{\pi 2}^0$ rejections and treatment of rare pathologies such as bucket-to-bucket wrap-around events and events in which photons escape through the beam hole. These constraints were also found to effective in the simulations for suppressing other decay modes such as $K_{\pi 3}$ and K_{e3} decay modes discussed below.

Dealing with low energy $K_{\pi 2}^0$ photons (where the inefficiency is greatest) is particularly important. The energy of the missing photons in $K_{\pi 2}^0$ events can be obtained by subtracting the measured energies of the two observed photons from the K_L energy. Requiring significant total missing energy (i.e. $(E(K_L) - E_{\gamma 1} - E_{\gamma 2})$ as is generally the case for $K_L^0 \to \pi^0\nu\bar{\nu}$ events suppresses most potential background events that contain lower energy missing photons. However, in unusual cases when one of the missing photons has very high energy and one has very low energy an additional cut on missing mass (i.e. $\sqrt{(E(K_L) - E_{\gamma 1} - E_{\gamma 2})^2 - (\mathbf{P}(K_L) - \mathbf{P}_{\gamma 1} - \mathbf{P}_{\gamma 2})^2)}$ is effective. Because the missing mass in $K_{\pi 2}^0$ events is proportional to $\sqrt{E_{miss1} * E_{miss2}}$, where E_{miss} is the energy of a missing photon, the missing mass also becomes small for the case of asymmetric energy sharing. Figure 42 shows the missing mass vs. missing energy distribution of photons for $K_{\pi 2}^0$ and $K_L^0 \to \pi^0\nu\bar{\nu}$ events. After removing the low missing mass and low missing energy region, we can suppress the low energy photons to achieve 10^{-8} overall detection inefficiency for the two missing photons in $K_{\pi 2}^0$ events.

The effect of eliminating events with small missing mass can be seen more directly by comparing $E_{\pi^0}^*$ distributions before and after the photon veto cut for the $K_{\pi 2}^0$ odd background events where one photon from each π^0 is missed (Figure 43). The peak above $E_{\pi^0}^*$=230 MeV after the photon veto cut corresponds to the small missing mass region [7]. This is one of the main reasons why the phase space below the $K_{\pi 2}^0$ peak, $E_{\pi^0}^* <$ 249 MeV, is used for the

[7] There is a one-to-one correspondence between $E_{\pi^0}^*$ and missing mass: $E_{\pi^0}^* = \frac{m_K^2 + m_{\pi^0}^2 - m_{miss}^2}{2m_K}$. For small missing mass, $E_{\pi^0}^*$ is large.

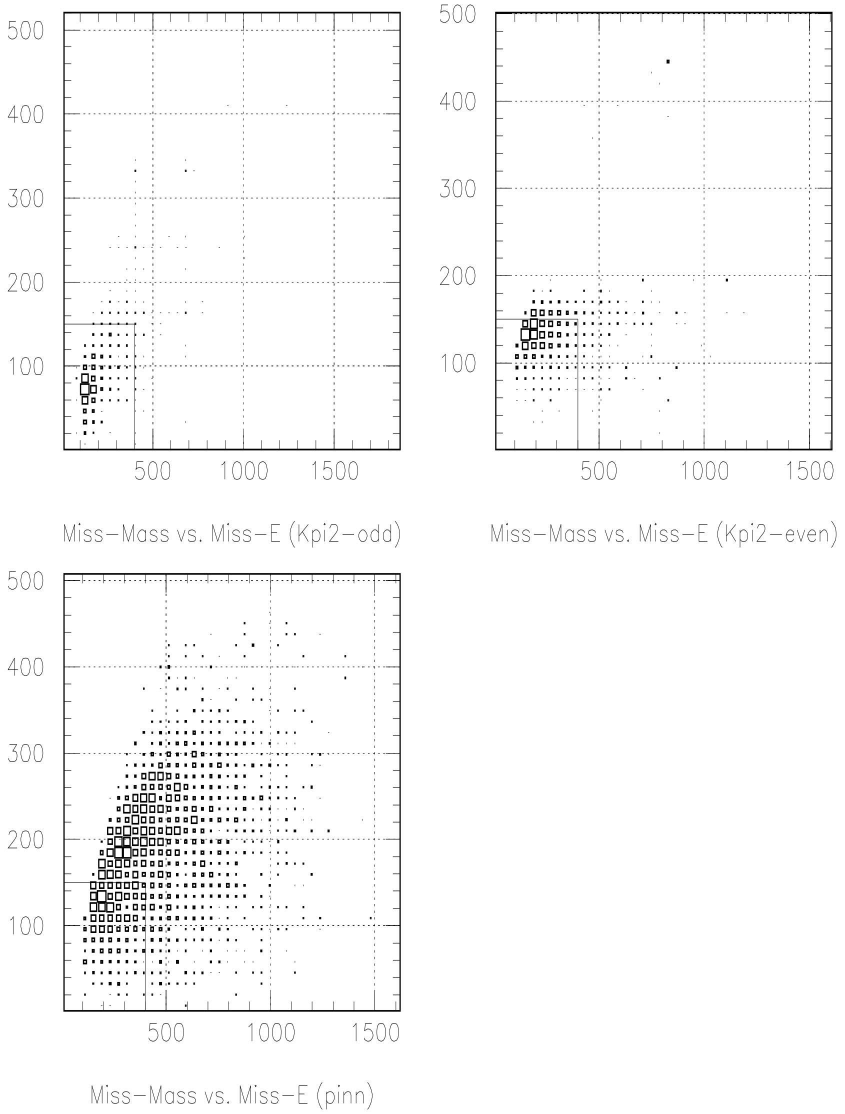

Figure 42: Missing mass vs. missing energy distribution of photons for $K^0_{\pi 2}$ odd, $K^0_{\pi 2}$ even and $K^0_L \to \pi^0 \nu \bar{\nu}$ events.

KOPIO measurement.

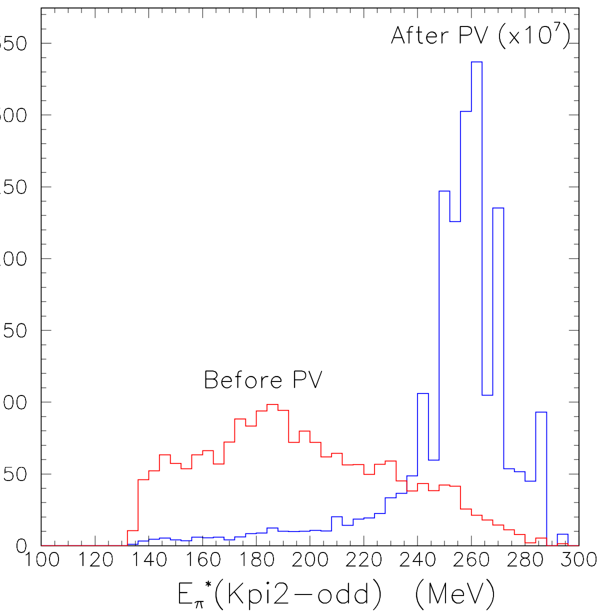

Figure 43: π^0 energy distribution in the K_L center of mass system ($E^*_{\pi^0}$) for $K^0_{\pi 2}$ odd events before and after photon veto cuts.

The $K^0_{\pi 2}$ even background arising from the previous timing micro-bunch ("wrap-around" events) can cause a serious problem because the E^*_π cut as well as the missing energy cut to suppress low energy missing photons may fail. Figure 44 shows E^*_π assuming that the particle is coming from the previous bunch versus the longitudinal π^0 momentum of the signal (box) and the wrap-around $K^0_{\pi 2}$ background. This background is suppressed by cutting on these quantities as indicated in the figure.

Table 11 gives the estimated acceptance factors for the $K^0_{\pi 2}$ backgrounds, including all combinations of 2 missing photons out of the 4 photons when both observed photons convert in the preradiator. Multiplying the total $K^0_{\pi 2}$ acceptance by the branching ratio and the number of K^0_L decays, we expect 13 events from this source split evenly the between the odd and even pairing types. When we include those cases where one photon converts in the preradiator and one in the calorimeter, and account for accidental losses (see below) the total $K^0_{\pi 2}$ background expected is 15 events.

$\underline{K_L \rightarrow \pi^+\pi^-\pi^0}$

Since the $K_{\pi 3}$ decay contains a π^0 in the lower momentum range of $K^0_L \rightarrow \pi^0\nu\bar{\nu}$, this mode is suppressed by a combination of charged particle vetos and additional c.m. energy cuts (E^*_π). Charged pions can disappear by detector inefficiency (e.g. insufficient light output from the charged veto scintillators) or via nuclear interactions.

Using 1 cm thick plastic scintillation counters and a threshold of 1MeV, Inagaki et al.[62] found inefficiencies for 1 GeV/c particles to be 3.2×10^{-4} for e^+, 6×10^{-4} for π^-, $< 1.6\times10^{-5}$ for π^+ and $< 1.3 \times 10^{-4}$ for e^-. In KOPIO, when the π^- reacts via charge exchange

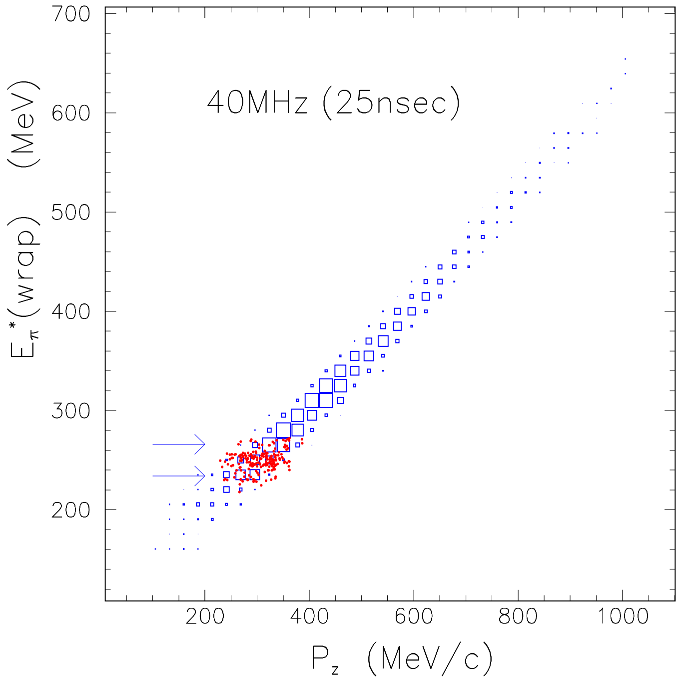

Figure 44: E^*_π assuming that the particle is coming from the previous bunch versus longitudinal π^0 momentum for the signal (boxes) and background events from wrap-around $K^0_{\pi 2}$ (even) decays (dots). The arrows indicate the cut values use to suppress the background.

$\pi^- p \to \pi^0 n$ or $\pi^- p \to \gamma n$ before being detected by the charged particle veto system, photon energy will be present elsewhere to reduce the overall inefficiency. However, the influence of the 3-3 resonance causes the interaction cross sections for pions to be large at KOPIO energies. Ultimately, pion reactions producing only neutrons will represent an irreducible level of efficiency. In order to make estimates for such processes, we have employed cross section measurements[63] on reactions of the type $\pi^+ + C \to p + p$ in the energy region appropriate for KOPIO and, assuming isospin symmetry, obtain values for $\pi^- + C \to n + n$ reactions (including those with larger numbers of neutrons). Then, taking into account the measurements of Inagaki et al. mentioned above, we estimated the overall charged pion inefficiencies for the $K_{\pi 3}$ background to be $\leq 10^{-4}$ for π^- and $\leq 10^{-5}$ for π^+ resulting in a suppression factor of $\leq 10^{-9}$.

The unusual case where a π^+ gets a very small energy and stops in a veto counter without depositing much energy is potentially problematic because the charged veto rejection for π^+ is not available. However, these events are concentrated in a particular phase space region in $E^*_{\pi^0}$ vs. missing energy as shown in Fig. 45 and can easily be rejected with little acceptance loss.

Figure 46 shows a plot of $E^*_{\pi^0}$ vs. $|E^*_{\gamma 1} - E^*_{\gamma 2}|$ for the $K_{\pi 3}$ background. A cut in $E^*_{\pi^0} <$ 190 MeV is very effective, and is compatible with the odd paring cuts. Putting all the cuts together gives an estimated 6 events (including 4 with two photons converted in the preradiator and 2 with one) from $K_{\pi 3}$.

Table 11: Acceptance factors for the $K^0_{\pi 2}$ even and odd pairing backgrounds (two photons converting in the preradiator).

Requirement	Even Pairing	Odd Pairing
No. γ Combinations	2	4
Z fiducial region and P_K	0.57	0.59
Solid angle	0.34	0.29
Preradiator Conversion Probability	0.50	0.50
$m_{\gamma\gamma} = m_\pi$	0.73	0.09
Wrap-$K_{\pi 3}$ low energy	0.68	0.78
E^*_π	0.016	0.27
Photon veto	8.3×10^{-8}	2.9×10^{-8}
Missing Energy	0.57	0.84
E^*_π vs. $\lvert E^*_{\gamma 1} - E^*_{\gamma 2}\rvert$	0.82	0.53
Acceptance	5.8×10^{-11}	8.1×10^{-11}
Total $K^0_{\pi 2}$ Acceptance	1.4×10^{-10}	

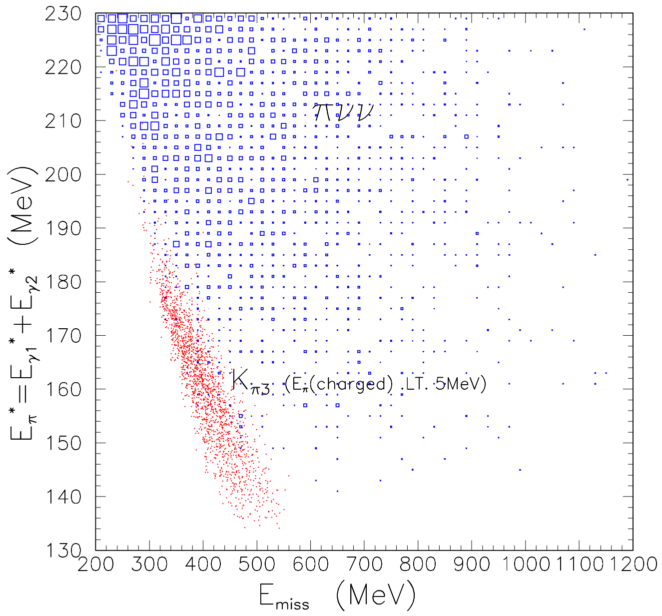

Figure 45: $E^*_{\pi^0}$ versus missing energy for the $K_{\pi 3}$ background when π^+ kinetic energy is less than 5MeV.

$K_L \to \pi^- e^+ \nu$ (K_{e3})

The K_{e3} background can arise when the π^- and e^+ react via charge exchange before they are detected and two photon clusters (each with one or two photons) remain. In making background estimates for KOPIO, we will use the inefficiencies for electrons and positrons

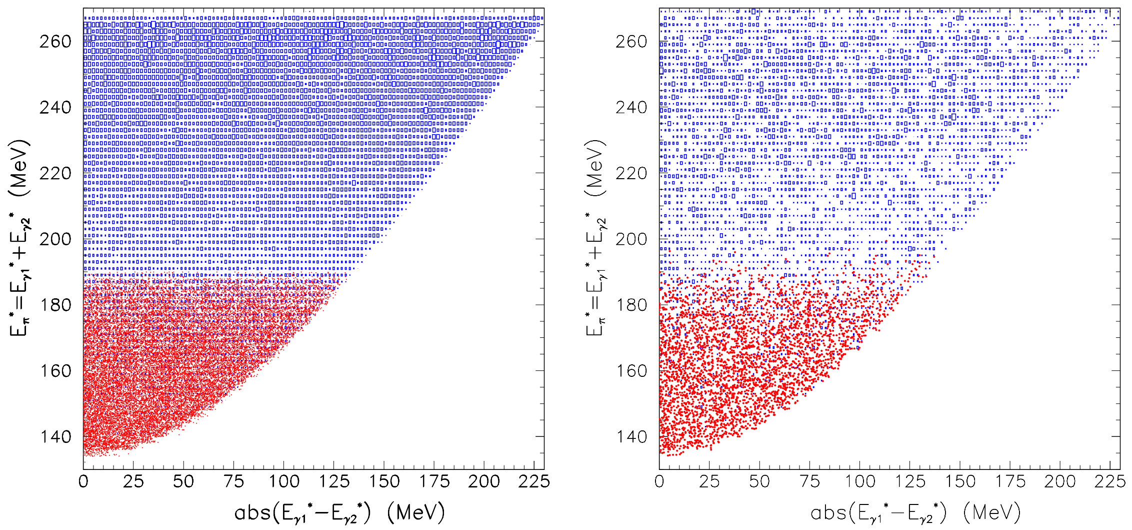

Figure 46: $E^*_{\pi^0}$ versus $|E^*_{\gamma1} - E^*_{\gamma2}|$ plot for $K_{\pi3}$ background (red dots) and signal (blue squares). Left plot shows the case of perfect resolution and right that of expected resolution.

measured by Inagaki et al. along with estimates of the pion charge exchange cross sections.

Fortunately, there are two extra kinematic handles on the K_{e3} background: the two photon mass ($m_{\gamma\gamma}$), which tends to be much larger than m_{π^0} and the c. m. energy of the two photons ($E^*_{\pi^0}$) which tends to be at the end point of the phase space. Due to the use of a low energy beam, the photons from $\pi^- p \to n\pi^0$ can be identified as two photon clusters, which provides the extra rejection power needed to suppress this mode.

Figure 47(a) shows the π^0 momentum distribution produced by the $\pi^- p \to n\pi^0$ reaction for the K_{e3} background. Here, we conservatively assume that only those events below 250 MeV/c can be rejected by the photon clustering cut. Figure 47(b) and (c) show $m_{\gamma\gamma}$ and $E^*_{\pi^0}$ distributions for the signal and K_{e3} background. Selecting the phase space region below the $K_{\pi2}$ peak in the $E^*_{\pi^0}$ distribution is particularly effective.

Overall, the $K_L \to \pi^- e^+ \nu$ background is expected to be 0.06 events.

$K_L \to \gamma\gamma$

$K_L \to \gamma\gamma$ is very tightly constrained by kinematics. For example, by knowing the direction of one photon, one obtains the energies of both photons and the direction of the other photon. Cutting on the monochromatic photon energies in c.m. system (E^*_γ) using an invariant mass cut on 2 photons($m_{\gamma\gamma}$) and the CM energy of the 2 photons ($E^*_{\pi^0}$), brings this process under control. We expect 0.04 events from this background source.

$\Lambda \to \pi^0 n$

Because of the large angle of the neutral beam used here, the cross section for producing Λs is low and they decay completely before reaching the decay volume. Backgrounds could arise from Λ's produced by halo neutrons and K_L's. Again, the production cross section of Λs by the beam halo is low because the beam is soft and it is hard for Λs to reach the

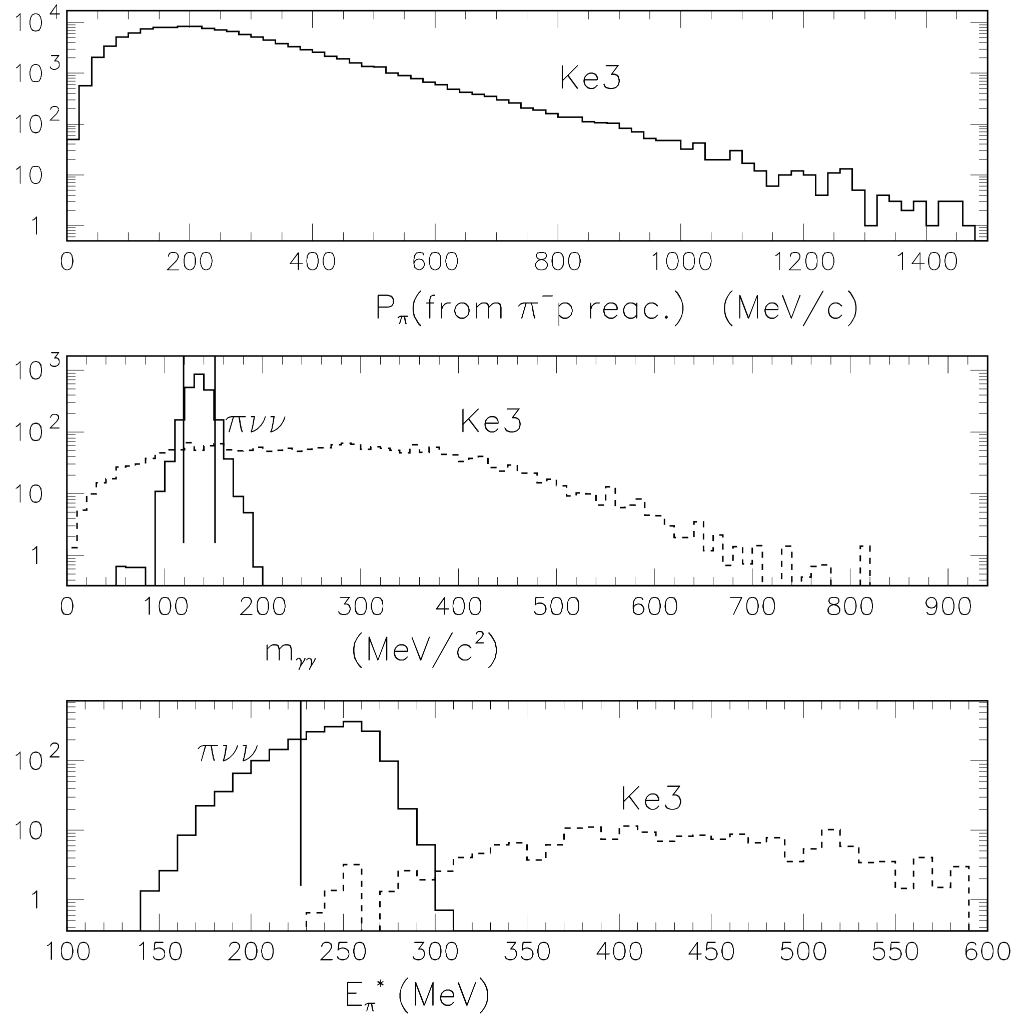

Figure 47: (a) Momentum of π^0, (b) invariant mass of 2 "photon" energy clusters ($m_{\gamma\gamma}$) and the (c) the center of mass energy of the two photons ($E^*_{\pi^0}$) of the K_{e3} background.

fiducial decay volume from the interaction point. Good collimation of the beam as well as a vertex cut to eliminate events produced near the surface of the last collimator suppresses this background to a negligible level of 0.2 events.

$nA \to \pi^0 A$

Neutrons interacting with the residual gas in the decay volume can produce single π^0s without any other easily detectable activity. This background is primarily suppressed by having an excellent vacuum (10^{-7} torr) and by the reduced number of neutrons above the π^0 production threshold (800MeV/c) at the 40 degree production angle. The micro-bunching of the beam provides further suppression of the neutrons as illustrated in Fig. 48 which shows the arrival time of K_L's and neutrons with respect to photons at 10m from the production target. Neutrons with momenta between 1 and 2.4 GeV/c fall into our arrival time of interest (i.e. K_L with momenta between 0.4 and 1.3 GeV/c). Within this time window, the neutron to K_L ratio is improved by a factor of 5. Despite the fact that a low energy beam is used here, the effective n/K_L ratio is as good as or better than in higher energy experiments. This background is further suppressed by the kinematic cuts used for $K^0_{\pi 2}$ because it includes a large unphysical kinematical phase space due to the miss-assignment of an incoming neutron as a K_L. We expect 0.5 events from this background source.

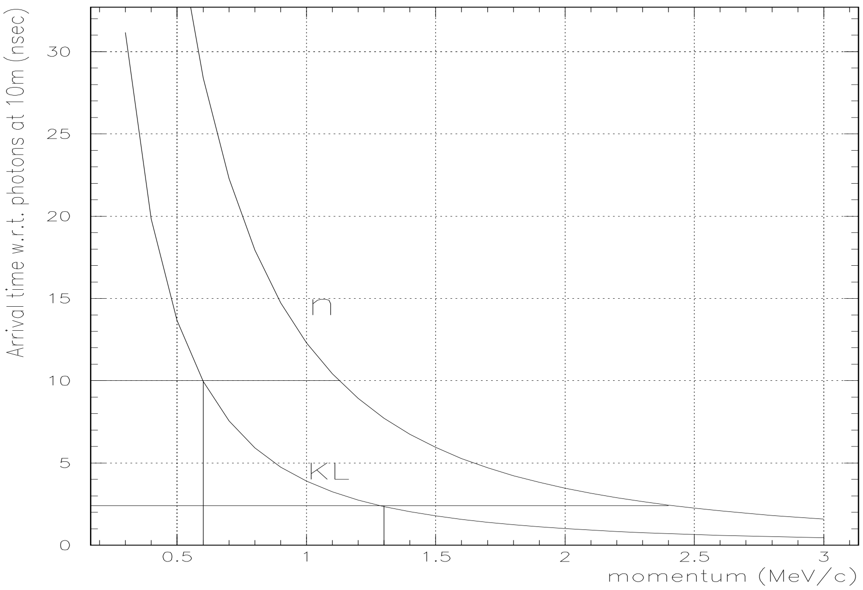

Figure 48: Arrival time of K_L's and neutrons with respect to photons at 10m downstream from the production target.

Accidentals

Accidental backgrounds are caused by beam halo neutrons, photons and K_L's which are scattered from the last collimator and get into the detector. Multiple stages of collimation of the narrow vertical beam should provide good collimation. From our measurements and GEANT calculations of our beam, confirmed by our correct simulation of the E791 beam, we would expect to bring the neutrons, kaons and gammas scattered into the detector down to $\sim$1MHz, 100 KHz, and 10 KHz, respectively. Requiring the converted track in the preradiator further suppresses neutrons and K_Ls because they show different track characteristics from photon conversions in the preradiator. Finally, photon tracking allows us to reject those photons coming from the upstream collimators. Assuming the signal event coincidence timing window of 1 ns, the rate of the accidental background is estimated to be $\sim$ 1 event.

1.14 Sensitivity and Measurement Precision.

Our estimates of sensitivity for $K_L^0 \to \pi^0 \nu\bar{\nu}$ decay are tightly coupled to the cuts required for background suppression, particularly for the $K_{\pi 2}^0$ and $K_{\pi 3}$ backgrounds. Fig. 49 illustrates the KOPIO methodology based on kinematic reconstruction in the K_L c.m. system. On the left is a pure kinematic scatter-plot of c.m. pion energy ($E_{\pi^0}^*$) vs. the difference of gamma energies in the c.m. system ($|E_{\gamma 1}^* - E_{\gamma 2}^*|$), for the $K_{\pi 2}$ background (blue dots) and $K_L^0 \to \pi^0 \nu\bar{\nu}$ (red dots). Regions 1, 2 and 3 are free of background. Now, even when the resolution and acceptance effects are included in the simulations, Regions 1 and 2 remain virtually background free as indicated on the right hand plot in fig. 49.

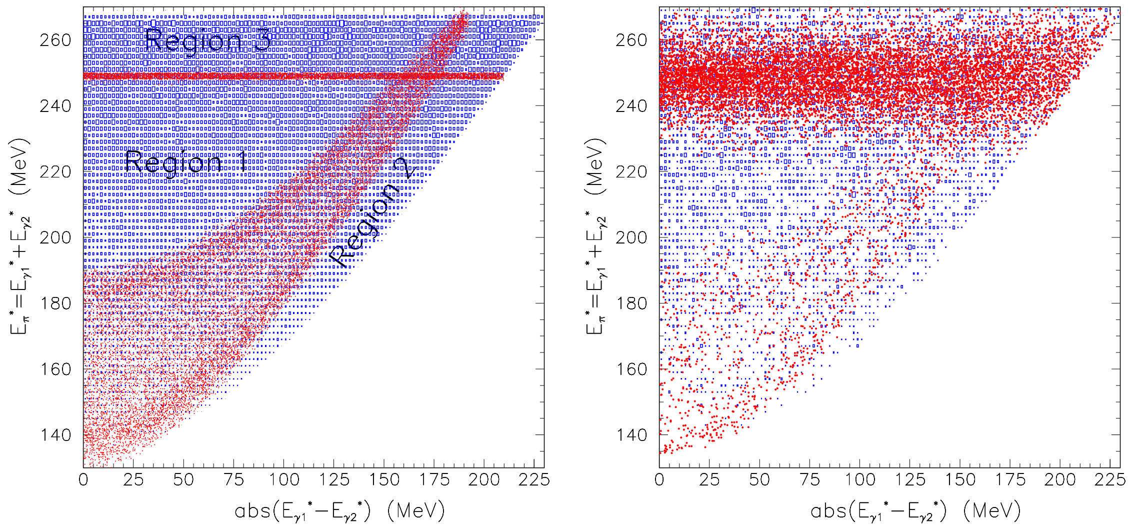

Figure 49: $E_{\pi^0}^*$ vs. $|E_{\gamma 1}^* - E_{\gamma 2}^*|$ for the $K_{\pi 2}$ background (red dots) and signal (blue boxes). The left hand figure shows the pure kinematic effects while the right hand figure includes experimental resolution effects.

Table 12 gives the breakdown leading to the estimated 1.0% acceptance for $K_L^0 \to \pi^0 \nu\bar{\nu}$ with two photons converting in the preradiator. The list includes factors for the 3 m long Z fiducial region and the K_L momentum cut (0.4 GeV/c $< P_K <$ 1.4 GeV/c), the solid angle acceptance, the conversion and reconstruction of two photons in the preradiator, and the accessible $K_L^0 \to \pi^0 \nu\bar{\nu}$ phase space (E_π^*) acceptance. In addition, there are cuts on missing energy and mass and on photon energy sharing. The inefficiency due accidental spoiling of good events is estimated to be $\leq$ 10% for a threshold of a few MeV in the preradiator, calorimeter and barrel veto, 300 MeV in the cacher, and a timing window of 2 ns. Taking the estimated accidental loss (due to accidental hits spoiling otherwise acceptable events) of 10%, the overall detection efficiency becomes 0.0114. Accepting the cases where one photon converts in the preradiator and one in the calorimeter increases the overall acceptance to $\epsilon = 0.015$.

The acceptance can be estimated for a variety of cut selections and levels of S/N. For the

Table 12: Acceptance factors for $K_L^0 \to \pi^0\nu\bar{\nu}$(two photons converting in the preradiator).

Requirement	Acceptance factor
Z fiducial region and P_K	0.58
Solid angle	0.33
Preradiator Conversion Probability	0.50
$m_{\gamma\gamma} = m_\pi$	0.73
Wrap-around/$K_{\pi 3}$ low energy	0.73
E_π^*	0.31
Photon veto	1.000
Missing Energy	0.91
E_π^* vs. $\lvert E_{\gamma 1}^* - E_{\gamma 2}^*\rvert$	0.9
Acceptance	0.0126

nominal $K_L^0 \to \pi^0\nu\bar{\nu}$ and background acceptance estimates given above, we have included events in which at least one of the photons converts in the preradiator. Of all such $K_L^0 \to \pi^0\nu\bar{\nu}$ events, about 50% have both photons converting and 50% have one photon converted in the preradiator and one in the calorimeter. Since there are additional constraints available when the angles of both photons are measured, this category contributes about 75% of the events for a given level of S/N. The signal yield is calculated as follows:

$$\begin{aligned}
N_K &= (4.2 \times 10^7 \ K_L \text{ decays/pulse}) \cdot 0.57(\textit{single decay}) \cdot (6.1 \times 10^6 \text{ pulses}) \\
&= 1.47 \times 10^{14} \ K_L \text{ decays} \\
N_{\pi\nu\bar{\nu}} &= N_K \cdot \epsilon \cdot \mathrm{B} \\
&= (1.47 \times 10^{14}) \cdot (0.015) \cdot (3 \times 10^{-11}) \\
&= 65 \text{ events}
\end{aligned}$$

where B$= 3 \times 10^{-11}$ is the SM central value for the branching ratio. The figure 0.57 is the fraction of unaccompanied K_L^0 decays assuming a 25 MHz microbunching frequency and a 3 second spill. A total AGS cycle time of 5.3 seconds is assumed. We expect to measure 65 $K_L^0 \to \pi^0\nu\bar{\nu}$ events in 9000 hours of beam at 1×10^{14} protons/spill. The single event sensitivity of the experiment would be approximately 6×10^{-13} if not limited by background. A summary of the signal and background estimates is given in Table 13. For the nominal cuts scenario, the signal would exceed the background by about a factor of 2.

Since we expect that the actual background levels will be determined reliably from the data, it will be feasible to select the cuts in order to optimize the precision of the extraction of the $K_L^0 \to \pi^0\nu\bar{\nu}$ branching ratio, and to demonstrate the stability of the result at varying levels of background suppression. For example, by tightening the cut on E_π^* vs. $|E_{\gamma 1}^* - E_{\gamma 2}^*|$ (see Table 13) the number of events could be reduced from 65 to 48 while the S/N ratio would increase from 2 to 3. Table 14 shows several other examples of the numbers of events obtainable with various S/N ratios and also the precisions obtainable on B($K_L^0 \to \pi^0\nu\bar{\nu}$), at the SM central value. If the other relevant CKM parameters were known well, it would then

Table 13: Estimated event levels for signal and backgrounds.

Process	Modes	Main source	Events
$K_L^0 \to \pi^0\nu\bar{\nu}$			65
K_L decays ($\bar{\gamma}$)	$\pi^0\pi^0$,$\pi^0\pi^0\pi^0$,$\pi^0\gamma\gamma$	$\pi^0\pi^0$	24
$K_L \to \pi^+\pi^-\pi^0$			9
$K_L \to \gamma\gamma$			0.04
K_L decays ($\overline{charge}$)	$\pi^\pm e^\mp\nu$,$\pi^\pm\mu^\mp\nu$,$\pi^+\pi^-$	$\pi^- e^+\nu$	0.06
K_L decays ($\bar{\gamma}, \overline{charge}$)	$\pi^\pm l^\mp\nu\gamma$, $\pi^\pm l^\mp\nu\pi^0$,$\pi^+\pi^-\gamma$		0.1
Other particle decays	$\Lambda \to \pi^0 n, K^- \to \pi^-\pi^0, \Sigma^+ \to \pi^0 p$	$\Lambda \to \pi^0 n$	0.03
Interactions	n, K_L, γ	$n \to \pi^0$	0.5
Accidentals	n, K_L, γ	n, K_L, γ	1.5
Total Background			35

be possible to extract η with a precision of approximately 10% from the KOPIO measurement of $K_L^0 \to \pi^0\nu\bar{\nu}$.

Table 14: Signal/Noise, numbers of $K_L^0 \to \pi^0\nu\bar{\nu}$ events and the precision of the B($K_L^0 \to \pi^0\nu\bar{\nu}$) measurement.

S/N	$K_L^0 \to \pi^0\nu\bar{\nu}$ Signal	B($K_L^0 \to \pi^0\nu\bar{\nu}$) Precision
1	94	0.15
2	65	0.15
3	48	0.17
5	32	0.20

References

[1] G. Buchalla and A.J. Buras, *Nucl. Phys.* **B548**, 309 (1999) hep-ph/9901288.

[2] M.K. Gaillard and B.W. Lee, *Phys. Rev.* **D10**, 897 (1974); J. Ellis, M.K. Gaillard and D.V. Nanopoulos, *Nucl. Phys.* **B109**, 213 (1976); L. Littenberg, *Phys. Rev.* **D39**, 3322 (1989).

[3] L. Littenberg and G. Valencia, *Ann. Rev. Nucl. Part. Sci.* **43**, 729 (1993); B. Winstein and L. Wolfenstein, *Rev. Mod. Phys.* **65**, 1113 (1993); J.L. Ritchie and S.G. Wojcicki, *Rev. Mod. Phys.* **65**, 1149 (1993); G. Buchalla, A.J. Buras and M.E. Lautenbacher, *Rev. Mod. Phys.***68**, 1125 (1996).

[4] A.J. Buras and R. Fleischer, in *Heavy Flavours II*, World Scientific, eds. A.J. Buras and M. Linder, 65-238 (1997).

[5] D. Rein and L.M. Sehgal, *Phys. Rev.* **D39**, 3325 (1989); G. Buchalla and G. Isidori, *Phys. Lett.* **B440**, 170 (1998).

[6] G. Buchalla and A.J. Buras, *Nucl. Phys.* **B400**, 225 (1993).

[7] W.J. Marciano and Z. Parsa, *Phys. Rev.* **D53**, R1 (1996).

[8] C. Jarlskog and R. Stora, *Phys. Lett.* **B 208**, 268 (1988).

[9] G. Buchalla and A.J. Buras, *Nucl. Phys.* **B412**, 106 (1994).

[10] S. Adler *et al.*, *Phys. Rev. Lett.* **79**, 2204 (1997).

[11] G. Redlinger, KAON-99 Conference, June 1999.

[12] M. Gronau, *Phys. Lett.* **B300**, 163 (1993).

[13] A.J. Buras, *Phys. Lett.* **B333**, 476 (1994).

[14] C. Dib, D. London and Y. Nir, *Int. J. Mod. Phys.* **A6**, 1253 (1991).

[15] Y. Grossman, Y. Nir, and R. Rattazzi, in *Heavy Flavours II*, eds. A.J. Buras and M. Lindner, World Scientific Publishing Co., Singapore, 755-794 (1997) hep-ph/9701231.

[16] G. Bélanger, C.G. Geng and P. Turcotte, *Phys. Rev.* **D46**, 2950 (1992).

[17] C.E. Carlson, G.D. Dorata and M. Sher, *Phys. Rev.* **D54**, 4393 (1996) hep-ph/9606269.

[18] Y. Nir and M. Worah, *Phys. Lett.* **B423**, 319 (1998).

[19] Z. Xiao, C. Li and K. Chao, *Eur. Phys. J.* **C10**, 51 (1999) hep-ph/9903348.

[20] Y. Kiyo, T. Morozumi, P. Parada, M.N. Rebelo, and M. Tanimoto, *Prog. Theor. Phys.* **101**, 671 (1999) hep-ph/9809333.

[21] Y. Grossman and Y. Nir, *Phys. Lett.* **B398**, 163 (1997).

[22] T. Hattori, T. Hasuike, and S. Wakaizumi, hep-ph/9908447v2 (1999).

[23] A.J. Buras, A. Romanino, and L.Silvestrini, Nucl. Phys. **B520**, 3 (1998).

[24] G. Colangelo and G. Isidori, *JHEP* **09**, 009 (1998) hep-ph/9808487 (1998).

[25] A.J. Buras and L.Silvestrini, *Nucl. Phys.* **B546**, 299 (1999) hep-ph/9811471.

[26] A.J. Buras, G. Colangelo, G. Isidori, A. Romanino and L. Silvestrini, hep-ph/9908371.

[27] A. Alavi-Harati *et al.* [KTeV Collaboration], *Phys. Rev. Lett.* **83**, 22 (1999) hep-ex/9905060.

[28] V. Fanti *et al.*[NA48 Collaboration], CERN-EP/99-114, hep-ex/9909022.

[29] S. Bosch, A.J. Buras, M. Gorbahn, S. Jager, M. Jamin, M.E. Lautenbacher, and L. Silvestrini, TUM-HEP-347-99, Apr 1999, hep-ph/9904408.

[30] A. Alavi-Harati *et al.,* hep-ex/9907014.

[31] T. Roser, private communication.

[32] R. Cappi and C. Steinbach, CERN-PS-OP-81-10, *Particle Accelerator Conference 1981*, 2806.

[33] J. W. Glenn, AGS/AD Technote 426 (1996); J. W. Glenn, *et al.*, **Proc. Particle Accelerator Conference** (in press), BNL-63890, May 1997.

[34] T. Abbott *al.* [E802 Collaboration], *Phys. Rev.* **D45**, 3906 (1992).

[35] P. Kapinos, E926 Technical Note 5, Aug 1997.

[36] S.V. Efremov, M.V. Kazarnovsky, E. Ya. Paryev, *Zeit. Phys.* **A344**, 181 (1992).

[37] S.V. Efremov, E. Ya. Paryev, *Zeit. Phys.* **A348**, 217 (1994).

[38] D. Dekkers *et al.*, *Phys. Rev.* **137**, B952 (1965).

[39] L. Littenberg, E926 Technical Note 11, Aug 1998.

[40] M. Grigoriev, Yu. Kudenko, O. Mineev, E926 Technical Note 7, April 1998.

[41] T. Abbott *al.* [E802 Collaboration], *Nuc. Instr. Meth.* **A290**, 41 (1990).

[42] R.A. Kryger et al., "Efficiency of a BaF_2 scintillator detector for 15-150 MeV neutrons" *Nucl. Instr. Meth.* **A346** 544 (1994).

[43] V. Wagner *et al.*, "Detection of relativistic neutrons by BaF_2 scintillators" *Nucl. Instr. Meth.* **A394** 332 (1997).

[44] C. Caso, *et al.*, *Eur. Phys. Jour.* **C3** 1 (1998).

[45] S.D. Worm, UTA thesis, UTEXAS-RHIP-95-1, UTEXAS-HEP-95-21, KL-243, Aug 1995.

[46] M. Hebert, private communication.

[47] W.T. Emmet, "Design and Manufacturing Considerations for the KOPIO Vacuum Vessel", KOPIO Technote TN012, (1998).

[48] H. van der Graaf, *et al.*, NIM in Phys. Res. A307 (1991), 220-230.

[49] Northern State Metal Corp.

[50] G.S. Atoyan, *et al.*, "Lead-scintillator electromagnetic calorimeter with wave length shifting fiber readout", NIM, **A320**, 144 (1992)

[51] G. David, *et al.*, "Performance of the PHENIX EM Calorimeter", PHENIX Technote 236 (1996).

[52] A. Golutvin, "Electromagnetic calorimeter for HERA-B", HERA-B Tech. Note 94-073 (1994).

[53] Technical Proposal, CERN LHCC 98-4, LHCC/P4, 20Feb. 1998.

[54] G.S. Atoyan, *et. al.*, "Preliminary Research of Shashlyk Calorimeter for E926", E926 Technote (1999).

[55] V.K. Semenov, private communication.

[56] T. Nomura, *et al.*, "Studies of a Prototype Photon Catcher", KOPIO Technote TN013 (1998).

[57] Y. Kudenko and O. Mineev, "Extruded grooved scintillator with WLS fiber readout", KOPIO TN008 (1998).

[58] S. Adler,*et al.*, Phys. Rev. Lett. **79** 2204 (1997).

[59] M. Blecher, L. Littenberg, and M. Zeller, "A Catcher Design for KOPIO", KOPIO TN016 (1999).

[60] E. Cisbani, *et al.*, "Proposal for a Dual Radiator RICH for HERMES", HERMES Technical note (1997).

[61] S. Ajmura et al., KEK preprint 97-243.

[62] T. Inagaki et al., NIM A359 (1995) 478.

[63] R. D. Ransome, et al., Phys. Rev. C 46 (1992) 273.